POLITECNICO
MILANO 1863

SCUOLA DI INGEGNERIA INDUSTRIALE
E DELL'INFORMAZIONE

Integrated nuclear-solid oxide electrolysis systems for electricity and hydrogen production

TESI DI LAUREA MAGISTRALE IN
ENERGY ENGINEERING-INGEGNERIA ENERGETICA

Author: **Adriano Gianchino**

Student ID: 940310
Advisor: Dr. Paolo Colbertaldo
Co-advisor: Ing. Marco Ficili
Academic Year: 2022-23

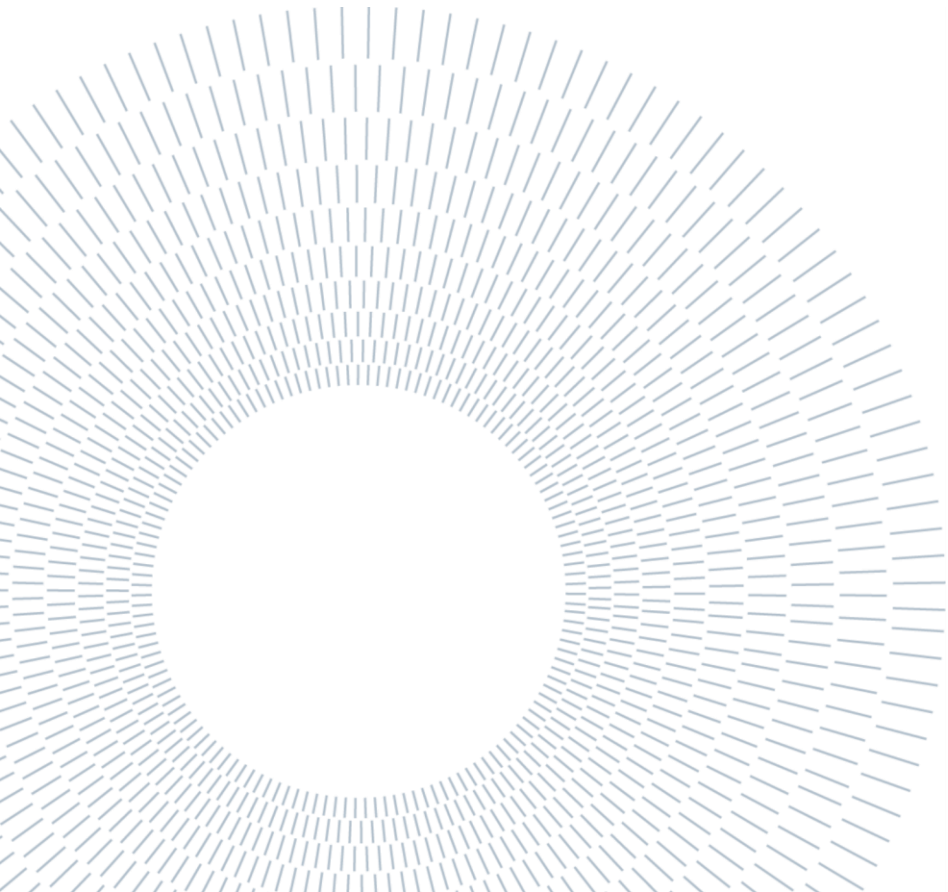

Abstract

To effectively pursue the climate goals set by international treaties like the Paris Agreement, greenhouse gases emissions must be strongly reduced. Low-emitting technologies like nuclear power plants (NPPs) and variable renewable energy sources (VRES) are a viable alternative for sustainable energy production. However, VRES present some issues related to their intermittent nature, and the need for energy storage systems and sustainable technologies to maintain grid stability arise.
Integrated energy systems (IESs) composed of a NPP and a solid oxide electrolysis (SOE) unit allow to produce both electric power and hydrogen (H_2). The steady availability of the NPP helps to support electric grid inertia with low emissions, while H_2 production enables energy storage and/or supply to hard-to-abate sectors. The synergies between these technologies can reduce H_2 production costs, and exploit IES flexibility to increase VRES penetration. Small modular nuclear reactors (SMNRs) enable decentralized production, reduce costs, and increase flexibility.
In this work, a SMNR-SOEC IES has been modelled, sized, and its steady-state operation has been simulated over its whole operational range. Two separate models were implemented for the SMNR and for the SOE system, using THERMOFLEX® and Aspen Plus®, respectively. The SMNR power block model allowed to obtain a curve that describes the electric power output as a function of the steam bled towards the SOE system while keeping the reactor at nominal conditions. The SOE system was sized accordingly, and the operation of the whole IES was simulated. The IES also generates heat at medium temperature as a byproduct. Six configurations for the SOE system were proposed and assessed, with different anode-cathode cross flows and endo/exothermal stack conditions. The exothermic case without outlet streams crossovers offered better thermodynamic performances and a lower layout complexity. The analysis of the energy flows showed that thermal integration could be improved by moving the bleeding point from the NPP at the inlet of the low-pressure turbine. The analysis of regulation options showed that the symmetric control of stack and modules constrains the operation at very low partial load.

Key-words: hydrogen, electrolysis, SOEC, integrated energy systems, nuclear power plant, small modular reactor

Abstract in lingua italiana

Per raggiungere efficacemente gli obiettivi climatici stabiliti dai trattati internazionali, come l'Accordo di Parigi, è necessario ridurre le emissioni di gas serra. Tecnologie a basse emissioni come le centrali nucleari (NPP) e le fonti energetiche rinnovabili variabili (VRES) rappresentano una valida alternativa per la produzione sostenibile di energia. Tuttavia, le VRES presentano alcune problematiche legate alla loro natura intermittente, facendo sorgere la necessità di sistemi di stoccaggio dell'energia e tecnologie sostenibili per mantenere l'inerzia di rete.
I sistemi energetici integrati (IES) composti da una NPP e un'unità di elettrolisi a ossidi solidi (SOE) consentono di produrre sia energia elettrica che idrogeno (H_2). La disponibilità costante della NPP contribuisce alla stabilità della rete elettrica con basse emissioni, mentre l'H_2 consente l'accumulo di energia e/o la fornitura di un vettore energetico ai settori hard-to-abate. Le sinergie tra queste tecnologie possono ridurre i costi di produzione dell'H_2 e sfruttare la flessibilità dell'IES per aumentare la penetrazione delle VRES. I reattori nucleari modulari di piccole dimensioni (SMNR) consentono una produzione decentralizzata, riducono i costi e aumentano la flessibilità.
In questo lavoro è stato modellato e dimensionato un IES SMNR-SOEC, e il suo funzionamento stazionario è stato simulato su tutto l'intervallo operativo. Sono stati implementati due modelli separati per la NPP e per il sistema SOE, utilizzando rispettivamente THERMOFLEX® e Aspen Plus®. Il modello del power block dello SMNR ha permesso di ottenere una curva che descrive la produzione di energia elettrica in funzione della portata di vapore inviata al sistema SOE, mantenendo il reattore alle condizioni nominali. Il sistema SOE è stato dimensionato di conseguenza, ed è stato simulato il funzionamento dell'intero IES, che genera anche calore a media temperatura come sottoprodotto. Sono state proposte e valutate sei configurazioni per il sistema SOE, con diversi incroci dei flussi anodo-catodo e condizioni di stack endo/esotermiche. Il caso esotermico senza incrocio tra i flussi offre prestazioni termodinamiche migliori e un layout meno complesso. L'analisi dei bilanci energetici ha mostrato che l'integrazione termica può essere migliorata spostando il punto di prelievo dalla NPP all'ingresso della turbina a bassa pressione. L'analisi della regolazione operativa ha mostrato che il controllo simmetrico di stack e moduli comporta alcune limitazioni a carichi parziali molto bassi.

Parole chiave: idrogeno, elettrolisi, SOEC, sistemi energetici integrati, centrale nucleare, reattori modulari di piccola taglia

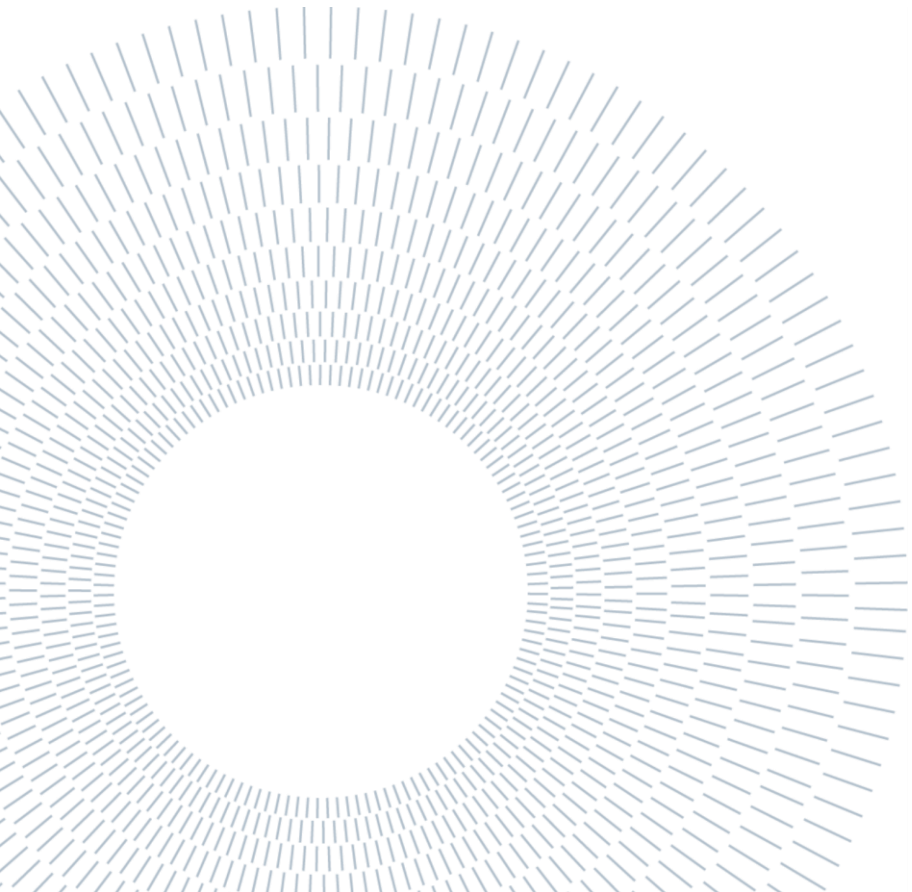

Contents

1. Introduction

1.1 Climate change

According to the United Nations (UN), climate change refers to long-term shifts in temperatures and weather patterns [1]. Through the analysis of natural records dating back from hundreds to millions of years ago (such as core samples of tree rings, corals, ice and sediments, or the temperature of rocks at various depths), palaeoclimatology has proven that such shifts have occurred throughout Earth's history. Due to natural phenomena such as solar cycles and very small variations in Earth's orbit, our planet has gone through eight cycles of ice ages and warmer periods in the last 800,000 years, with the end of the last ice age about 11,700 years ago marking the beginning of the modern climate era and of human civilization [2]. However, the rate at which these changes have occurred ever since the Industrial Revolution (early to mid-1800s) has never been seen before, and human activities have undeniably been the main driver.

The huge technological progress in the last two centuries led to a relatively sudden development of mankind and a growth of the global population, with an increase in needs for resources and energy. These quick steps forward have been supported by a massive utilization of fossil fuels that, upon combustion, and together with other human activities required to guarantee modern standards of living, release several noxious substances in the atmosphere. Among those are the so-called Greenhouse Gases (GHGs), mostly carbon dioxide and methane, which are responsible for the greenhouse effect.

Life on our planet is made possible by the light energy from the Sun. From a thermodynamic point of view, the energy hitting the Earth is filtered by the atmosphere and about half of it makes it to the surface, where it is absorbed and radiated back to space in the form of infrared emissions, representing a heat loss in Earth's energy balance. GHGs act like a blanket wrapped around the planet, trapping the heat radiating from Earth toward space, causing about 90% of this heat to be absorbed and re-radiated, reducing the heat loss to space and hence slowing down the cooling process, contributing to global warming.

Scientists agree on blaming the trends of the last 200 years on human activities, as natural causes alone would not suffice. As an example, with respect to 1750, the atmospheric carbon dioxide levels have raised by nearly 50%, while the average amount of energy from the Sun either remained constant or slightly increased [3]. When compared to pre-Industrial times (before 1750), the average temperature is nowadays 1.1°C higher, warmer than it has been in the last 100,000 years and expected to reach (or even exceed) 1.5°C within a few decades.

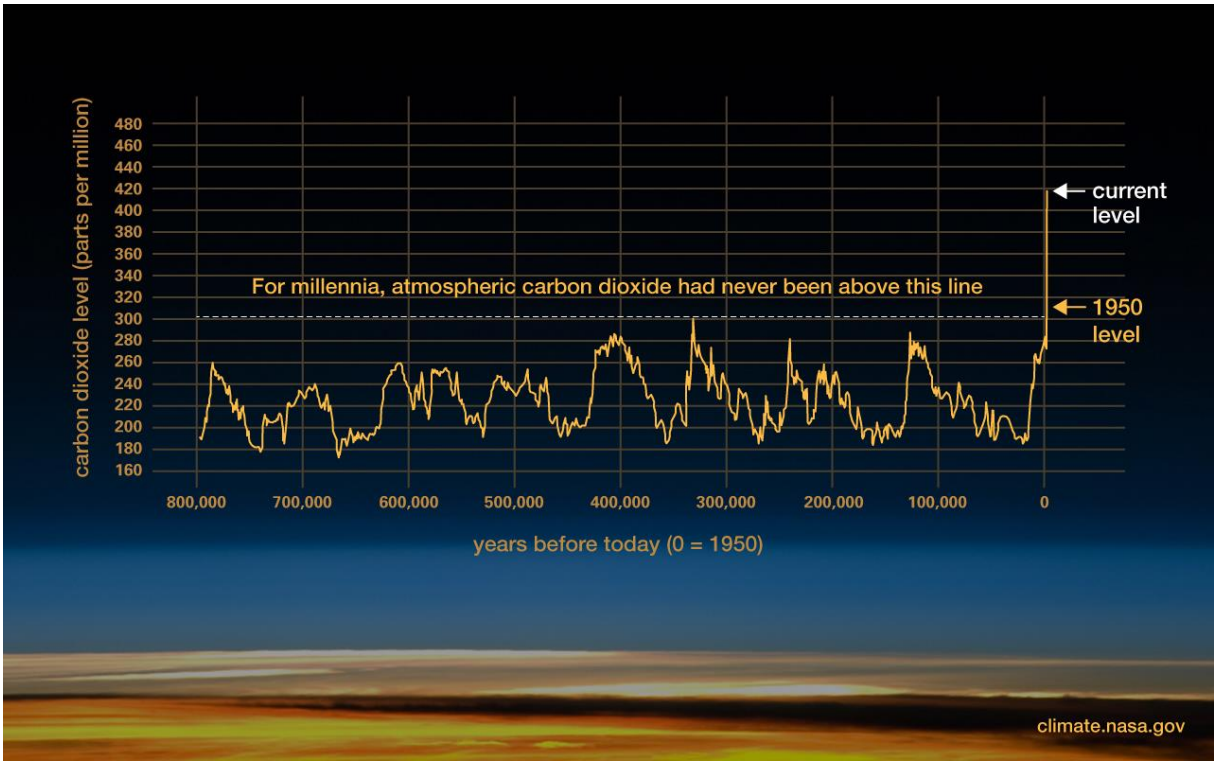

Figure 1.1 - Atmospheric concentration of carbon dioxide in the last 800,000 years [2]

Each of the last four decades has been warmer than any previous since 1850, with the last one (2011-2020) being the warmest on record [1], [4]. If an increase of solar activity would have been the cause of the warming, scientists would expect Earth's atmosphere temperatures to increase evenly. What can be observed, instead, is a cooling of the outer layers and a warming of those close to the surface, serving as evidence to the heat-trapping mechanism. Thinking of Earth as a system, it is clear how changes in a geographic area can affect all the others, with the rise of the average temperature being merely the tip of the iceberg.

Consequences range between water scarcity, rising sea levels, flooding, melting of polar ice, shrinking of glaciers, and declining biodiversity. Some of these changes are occurring even faster than scientists previously assessed (such as intense droughts, severe wildfires, and catastrophic storms). All these phenomena impact our lives in different ways, and the consequences can be experienced on various levels, affecting our health directly or indirectly. Heat and cold waves, together with droughts, can compromise agriculture and our ability to grow food, with intense storms and rainfalls representing other serious threats to crops, putting millions of people at risk of famine.

The shrinking of glaciers is a menace to several habitats and sweet water reserves. Oceans play a huge role in our planet equilibrium. The melting of polar ice is causing many animal species to become extinct and contributes to modify seawater salt levels and oceanic currents, which have a direct effect on climate all over the globe. Moreover, oceans soak up most of the heat from global warming, causing them to warm up and increase their volume due to thermal expansion, leading to an increase of sea level (made even worse by the melting of ice sheets). This, together with saltwater intrusion is pushing people on small island, coastlines, and water courses to relocate. Lastly, oceans absorb the majority of carbon dioxide in the atmosphere, helping to mitigate the greenhouse effect. However, carbon dioxide makes water more acidic, endangering marine life and coral reefs.

Wildfires can erase whole forests, emitting large quantities of carbon dioxide and reducing Earth's ability to absorb it.

These are just some of the effects of climate change at the roots of climate migration, that is the voluntary movement of people to new places in the hope to escape the consequences of global warming, with the number of "climate refugees" expected to rise in the next years.

Measures are being taken to contrast climate change and its effects, and several international treaties have been signed in the last decades. Among these, the Paris Agreement of 2015, signed by 196 parties, aims to limit the temperature increase to 1.5-2°C above pre-industrial levels by the end of the century. To achieve this goal, it becomes crucial to reduce GHGs emissions, performing an energy transition towards new sustainable and renewable sources.

1.2 Hydrogen as an energy carrier

The reduction in use of fossil fuels in favour of a higher penetration of renewable energy sources (RES) in the energy mix represents a challenge for energy networks and sets the necessity to store energy. Indeed, energy sources like solar photovoltaic

(PV) and wind are non-programmable, meaning that energy production is subdued to an uncontrollable source availability (i.e., the Sun is shining, or the wind is blowing). Thus, energy production and demand curves may not always coincide, causing gaps when demand is not met by production or vice versa. From here the need to store energy when an excess is produced, so to make it available when demand exceeds production, filling production-demand gaps by matching the curves and overcoming RES volatility.

A large number of energy storage technologies have been developed and, despite further categorizations according to storage duration, response time and function are possible, one main distinction can be made based on the type of stored energy: mechanical (e.g., pumped hydro, compressed air, flywheel), electro-chemical (e.g., secondary and flow batteries), chemical (e.g., hydrogen), thermal (e.g., sensible and latent heat) and electrical (e.g., supercapacitors) [5]. This combination of RES and storage is a viable way to electrify many industrial and transport sectors, switching their primary energy sources to low-emitting ones.

However, direct coupling is just not possible for some sectors. It is the case of heavy industry (e.g., steel and cement production, ammonia, and other chemical products), and aviation or maritime transport, as these sectors are very energy intensive and require either high process temperatures or large fuel storages to operate. Thus, they still mostly rely on fossil and are highly carbon-intensive (around 30% of global GHGs emissions with $1 \cdot 10^{10}$ t/y, [6]): from here the definition of *hard-to-abate sectors*.

This is one of the main reasons behind the interest aroused by hydrogen in recent years, as it can become a strong candidate to overcome this problem. From the perspective of a Net-Zero Emissions (NZE) Scenario [7], hydrogen has the potential to prevent GHGs emissions for up to $7 \cdot 10^{9}$ t/y by 2050, with the capability to improve 20% of the overall abatement required. Moreover, hydrogen is the only scalable, cost-efficient, and long-term alternative to decarbonize hard-to-abate sectors. It is highly energy intensive (LHV = 119.96 MJ/kg) and can be used both as an energy carrier as well as a feedstock. It allows the storage and transportation of large quantities of energy for long distanced through piping and vessels, providing adaptability and enhancing integration on RES in the energy mix [8].

Albeit being the most abundant element in the whole universe, hydrogen in its molecular form (H_2) is very rare on Earth and is mostly found as part of other chemical compounds. Thus, the need to produce hydrogen in its molecular form for energy production purposes and the necessity to use energy to separate it from other chemical compounds. There are different methods for hydrogen production, but not all of them are suitable with a NZE Scenario and emissions abatement, as will be later explained.

1.2.1 Classification and labelling

Hydrogen is commonly labelled using colours, which refer to the process and the energy source used for its production. According to the colour convention in use, hydrogen can be labelled as: black/brown, grey, blue, turquoise, green, and purple. The meaning of each of these labels is explained in the following.

- **Black/brown hydrogen:** production occurs through a thermochemical process called "coal gasification", which is the production of syngas starting from water, coal, and air/oxygen. The colour indicates if either bituminous coal (black) or lignite (brown) is used, even though also sub-bituminous and anthracites are used. This process is polluting and causes emissions of CO and CO_2, which are byproducts contained in syngas alongside hydrogen.
- **Grey hydrogen:** production occurs through natural gas steam reforming, also referred to as steam methane reforming (SMR). The chemical reactions involved are the following:

$$CH_4 + H_2O \rightarrow CO + 3H_2 \tag{1.1}$$

$$CO + H_2O \rightarrow CO_2 + H_2 \tag{1.2}$$

  This label also implies the absence of carbon capture, utilization, and storage (CCUS), with CO_2 emissions from production estimated in $830 \cdot 10^6$ t/y. Grey hydrogen, together with black/brown, currently represents the largest share of hydrogen on the market, and around 40% of it is a by-product of other chemical processes. This type of hydrogen is mostly used in the petrochemical industry and ammonia production [9].
- **Blue hydrogen:** produced like grey hydrogen, but with the use of CCUS technologies. Applying CCUS to steam methane reforming helps reducing CO_2 emissions up to 90%. Blue hydrogen can be considered as a momentary solution during the full transition to cleaner types of hydrogen [9].
- **Turquoise hydrogen:** produced through methane-pyrolysis, a long-known three-steps process already used for other industrial applications. The single steps are thermal decomposition, plasma decomposition and catalytic decomposition. Hydrogen can be produced by arresting the process at the first step:

$$CH_4 \rightarrow 2H_2 + C \tag{1.3}$$

  Solid carbon in the form of filaments or nanotubes is obtained as a by-product, making it usable for other processes or simply easier to store, reducing the carbon footprint [9].
- **Green hydrogen:** produced through water electrolysis using electricity from renewable sources. There are different technologies to perform water

electrolysis, which will be discussed in the following. The main characteristic of green hydrogen is that it does not cause direct GHGs emissions in its production phase, as the only by-product is oxygen. Also, a very high level of purity can be achieved (>99.95%) [9].

- **Purple hydrogen:** produced like green hydrogen, but the process is sustained by electricity produced from nuclear power plants (NPPs). Like in the case of green hydrogen, there are no GHGs emissions directly linked to this label. Currently, hydrogen from water electrolysis (green, purple, and using grid electricity) represents a very small fraction of the total production, around 0.03% [9]. The analysis on this work will be performed on this production route, and the reasons for that will be provided in the following.

Other labelling colours can be found in literature, but in the end they all refer to the main classification showed above.

It becomes obvious that, in an NZE scenario, only green and purple hydrogen become a viable alternative as their GHGs emissions are null.

1.2.2 Market forecast and energy sources competitiveness

As already discussed, there are several scenarios indicating a path for achieving climate goals by 2050. Many of these scenarios expect a significant increase in the use of hydrogen, and hence of its production and demand.

Typically, when dealing with hydrogen strategies, three different time horizons with different priorities are set: short-term (2025), medium-term (2035), and long-term (2050). The goals in the short-term are closing the competitive gap between fossil fuel and water electrolysis, and to decarbonise the existing usages of hydrogen. In the medium-term, hydrogen production is expected to grow as new production facilities in the scale of an electric gigawatt become available. Industrial applications are still expected to lead the demand, even though new usages in the transport sector are going to enter the market. On the long-term, given the growingly stringent carbon constraints, hydrogen production from low and high temperature electrolysis using low-carbon electricity is expected to dominate the market. Hydrogen will become a widely used flexible storage vector, and its use in industrial and transport sectors will be more and more commoditised. This will cause markets to be no longer limited to small areas of production and consumption, leaving the concepts of “hydrogen valleys” or “hydrogen hubs” behind [10].

According to a report from the International Energy Agency (IEA), in the NZE scenario, global hydrogen use expands from less than 87 Mt in 2020 to 528 Mt in 2050, with an intermediate value of 212 Mt in 2030, 54% of which is expected to come

from water electrolysis [11]. The production of this amount of hydrogen from electrolysis would require an additional electrical demand around 1.5 times the current European demand, leading to a huge increase in installed capacity.

Obviously, this means that the different energy production technologies will affect the final cost of hydrogen. It is easy to imagine how renewables will represent the largest share of future low-carbon sources, but their variability rises issues with a vast deployment and high penetration in the energy mix. In this sense, nuclear energy represents a source of dispatchable and low carbon electricity, which would make it possible to operate the electrolyser at high load factors without compromising hydrogen's carbon intensity [10].

In a report from OECD and NEA [10], the Levelized Cost of Hydrogen (LCOH) and the Levelized Cost of Hydrogen Delivery (LCOHD) are provided for different business models. Figure 1.2 shows the comparison between LCOH of hydrogen from water electrolysis combined to renewables or nuclear energy and that of hydrogen from steam methane reforming for two different natural gas prices: 20 USD/MWh and 100 USD/MWh. This cost only accounts for production, but storage and delivery of hydrogen could represent an important factor in the cost structure according to the different scenarios and business models. Figure 1.3 shows how storage, distribution, and transport of hydrogen impact on its cost structure.

However, it is important to remind that LCOH and LCOHD only allow for a first analysis of the relative competitiveness of different technologies, providing just a superficial overview. Indeed, just like any other energy carrier on the market, hydrogen needs production and consumption profiles to match so to have an efficient infrastructure design.

To perform a correct assessment, the whole value chain should be analysed to contribute to cost-efficient infrastructures and enhance potential synergies, and a key insight is that the total cost of the value chain will determine the competitiveness of different business models for hydrogen production.

The analysis highlights how, in the short term, most of the demand of hydrogen will come from the industry, which would be better served by a steady production. In this perspective, when value chain costs are added to hydrogen production costs for different options of electricity generation, nuclear energy stands out as a competitive solution: it would be a dispatchable and large-scale solution, enhancing co-location synergies with large-scale demand, and minimising infrastructure costs for hydrogen storage, transport, and distribution (i.e., given an electrolyser scale, nuclear-based hydrogen allows for a larger volume and continuous production, so to have a cost-efficient deployment of all infrastructures).

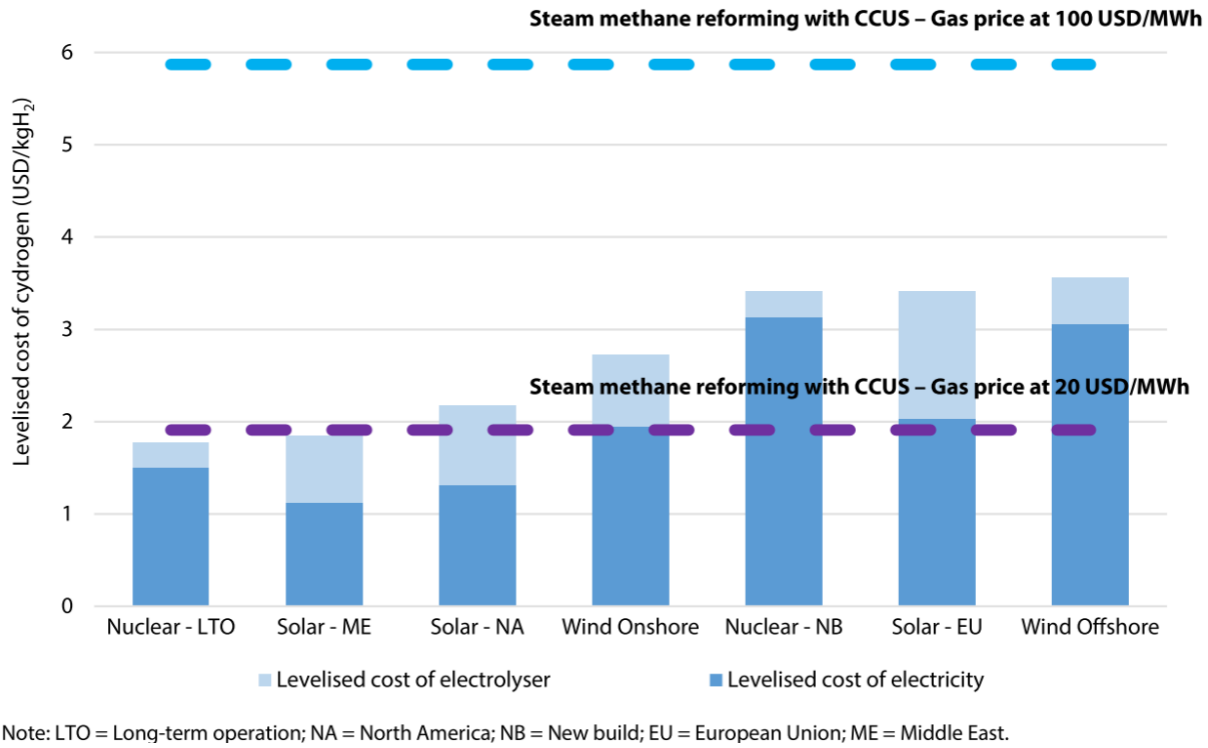

Note: LTO = Long-term operation; NA = North America; NB = New build; EU = European Union; ME = Middle East.

Figure 1.2 -LCOH for different energy sources [10]

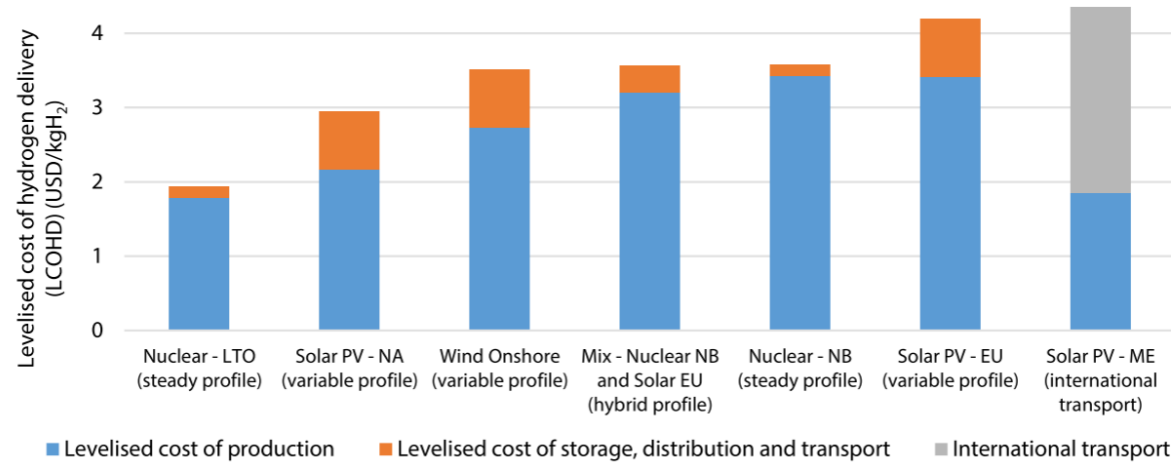

Note: LTO = Long-term operation; NA = North America; NB = New build; EU = European Union; ME = Middle East.

Figure 1.3 - LCOHD for different energy sources [10]

Moreover, nuclear-hydrogen hubs could further improve their economics by using clean heat from nuclear for other industrial processes nearby, or by exploiting synergies with renewable sources like solar PV, leveraging nuclear steadiness and PV low-cost electricity so to optimise both hydrogen cost of production and delivery [10].

1.3 Electric grid stability and flexibility

An electrical grid is a complex network of interconnected infrastructures which allow the electric power generated by power plants to be delivered to end-users in an efficient and reliable way. A simplified electrical grid can be imagined as a cascade of power generation facilities (which can span a large variety of technologies, from classical thermoelectric plants to solar PV and wind), transmission lines, distribution substations and users. However, reality is much more complex, and many other components are present in actual electrical grids, such as control systems and backups. Different electrical grids may even be interconnected, both on international and regional level, adding a further layer of complexity to the grid control.

A proper operation of the electrical grids is crucial for a reliable, consistent, and widespread distribution of electric power to support countless human activities and enhance the quality of life. Fluctuations in power supply, outages and interruptions are highly undesirable and to be avoided. Consequently, grid stability is one of the main characteristics that must be guaranteed when dealing with electrical grids. A well-designed, monitored and operated electrical grid should be able to maintain a steady electricity supply despite fluctuations and variations of operating conditions. Balancing of supply and demand through a correct management of grid components is of key importance to avoid disruptions.

Grid stability is a broad concept, and it consists of various aspects which must be considered altogether. Among these, some are strictly correlated to the power generation section of the grid or to the production-load balancing, such as grid frequency stability, electric generators rotor angle stability and transient stability.

Electrical grid inertia is a major factor in maintaining grid stability and can be seen as the resistance of the grid to sudden changes in its frequency, similarly to what is described by Newton's first law of motion. Indeed, under normal operating conditions, the frequency of an alternating current electrical grid is usually kept constant to 50 Hz or 60 Hz, and deviations from these values can cause disruptions and blackouts.

Traditional fossil fuel or nuclear power plants rely on rotating machines to convert thermal power into electric power. Turbines and electric generators involved in the energy conversion process have huge masses, meaning that these machines possess a significant quantity of kinetic energy when in motion. When a change in electric demand or production occurs (e.g., the transient represented by the sudden disconnection of a large power plant from the grid), grid frequency could deviate from the constant value, likely leading to system failure. The kinetic energy held by the rotating masses helps to dampen these effects and keep grid frequency

oscillations within a narrow range. Grid inertia is strictly linked to synchronous generators, typical of the above-mentioned technologies.

In the past decades, renewable energy sources have become increasingly relevant. Technologies like solar PV or wind turbines are viable alternatives for low-carbon electric power production, but they lack the inherent rotational inertia typical of thermoelectric power plants (solar PV) or make use of non-synchronous electric generators (wind). In both cases, electric generators are connected to power converters, decoupling the generator from the grid, and not inherently contributing to inertia. The increasing share of variable renewable energy (VRE) in the energy mix causes the reduction of conventional synchronous sources and the increase of non-synchronous generators. If the latter cannot not provide synthetic inertia to the grid, frequency control and grid stability can be compromised [12].

An energy system with a high VRE penetration may face problems linked to their intermittency, location-specific output, uncertainty, and limits in predictability. These factors could force the grid operator to allow less wind or solar PV generation than possible to maintain grid inertia and stability: this amount of energy that could be potentially used is known as curtailment. To reduce curtailment and allow a larger share of VRE in the energy mix in compliance with climate goals, it becomes necessary to increase grid flexibility, so to allow the energy system to quickly adapt to new operating conditions. Among the solutions proposed to increase flexibility are grid expansion, optimal ratios between wind and solar generation, curtailment of VRE, energy storage, flexible generation of traditional power plants, demand response, power-to-X technologies, system diversity, forecast improvement and institutional changes [12].

1.3.1 The role of nuclear energy

Not all the technologies for electric power production have the same capabilities in terms of flexibility due to technical or economic constraints. Power plants can be classified as inflexible, flexible, and highly flexible. A further distinction can be made basing on their dispatchability, with electric power technologies classified as non-dispatchable, partially dispatchable, and highly dispatchable.

VRE are non-dispatchable technologies, as their production is non-programmable and can only deliver energy when the main resource (such as wind or sunlight) is available. When VRE are not able to meet the energy demand, other energy sources are required to perform load following and maintain grid equilibrium.

Technologies used for this purpose belong to those classified as highly flexible plants, which include reservoir hydroelectric, aero-derivative, and simple cycle gas

cycles. Natural gas power plants are usually used for peak load operation since they have low capital cost, high operating cost, but emit significant quantities of GHGs. They are designed to work as peak load, and the operating price to increase their flexibility can be very low [12].

On the other side of the spectrum are inflexible power plants, which are usually designed for baseload operation, meaning that their production is kept as constant as possible due to their ramp rates, long start-up times or minimum load limits which do not allow for an efficient load-following operation. Among these technologies are nuclear, inflexible combined-cycles and some types of coal-fuelled power plants.

A high penetration of VRE in the energy leads to volatile electricity prices during the day, as energy market is strongly dependent on their production. When production peaks, electricity price goes down.

In this context, because of grid inflexibility, since NPPs are traditionally operated at baseload and at maximum capacity to minimize LCOE, they might have to sell surplus electricity at low or even negative prices (that is, producer pays the market to absorb its surplus production and avoid undesirable regulation on inflexible plants) when demand is low [13].

What emerges is that, in the effort to decrease the emissions from the energy sector, NPPs represents a valid alternative to conventional fossil fuels due to their high reliability, high dispatchability, large capacity factors and low carbon footprint. Moreover, a high share of VRE in the energy mix might represent a major drawback for grid stability due to their inability to provide grid inertia, which could be guaranteed by NPPs to maintain overall low emissions. However, this energy mix also requires an enhanced grid flexibility to avoid negative energy prices and grid failures. Among the possible solutions, power-to-hydrogen represents an interesting option to store excess energy, decarbonize had-to-abate sectors and increase the grid flexibility.

1.3.2 Overview of fission NPPs

Nuclear energy can be produced in two different ways: nuclear fission and nuclear fusion. In a nuclear fission reaction, the heavy nucleus of an atom is split in two or more smaller nuclei, releasing energy in the process. In a nuclear fusion reaction, instead, two light nuclei of different atoms merge and energy is released during the process.

The NPPs currently on the market exploit nuclear fission reactions to produce electric power. The fission reaction happens in the core, where a nucleus of a fissile material (usually Uranium-235) is bombarded by a neutron. The nucleus of Uranium-235

splits into a barium nucleus and a krypton nucleus, two or three neutrons, and a certain amount of energy in the form of heat is released. The neutrons released in this process will bomb the other surrounding atoms of Uranium-235, initiating a controlled and self-sustained chain reaction [14]. The heat from the reaction is used to produce steam, whose thermal power can be converted into electricity by means of a steam cycle. Since the energy production process does not involve fossil fuels combustion, no carbon emissions are directly linked to NPPs. Even with a complete life-cycle assessment, NPPs release the same amount of equivalent CO_2 emissions per unit of produced energy as wind power, and about one third of solar PV (Figure 1.4).

As of November 2023, there are about 440 operating NPPs with a combined capacity of about 390 GW_e. These NPPs provided 2545 TWh in 2022, which is about 10% of the world's electricity. About 60 reactors are currently under construction in the world (most of them in Asia), and a further 110 are planned. In the last 20 years, 108 reactors were retired and 97 started operation [15].

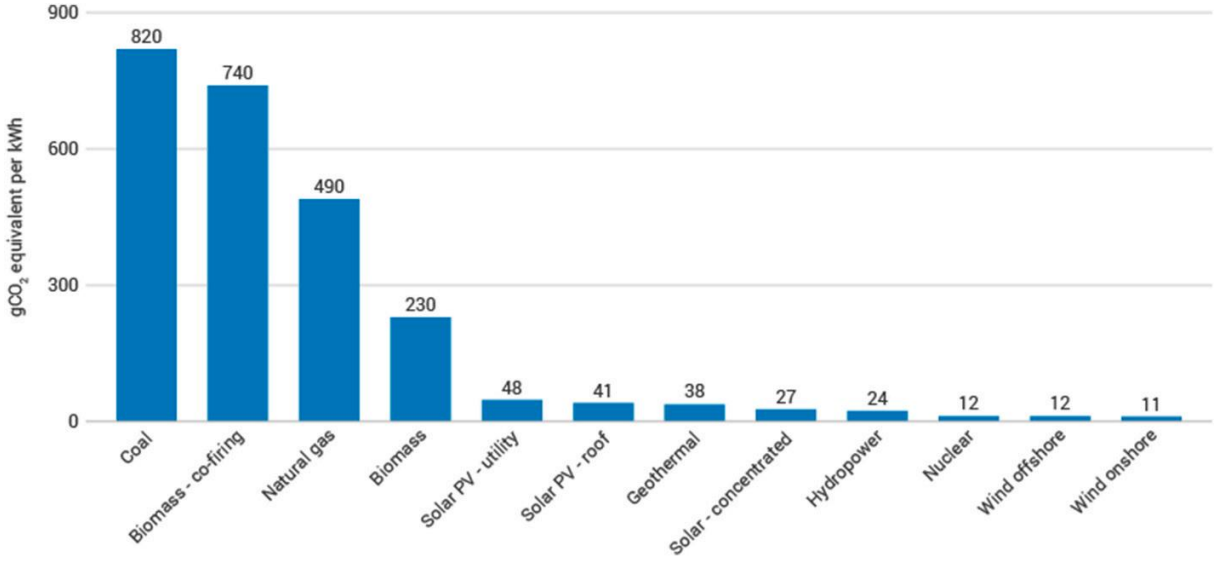

Figure 1.4 - Equivalent CO_2 emissions per unit produced energy for different energy sources [14]

Nuclear reactors use a cooling fluid to keep the core temperature below the safety limits by removing the thermal power released by the fission reactions and making it available for energy transformation through one or more circuits. The moderator is a material whose purpose is to slow down the neutrons released by the fission reactions, helping to achieve and maintain the chain reaction. There are different types of nuclear reactors, which can be classified according to the fuel they use, the cooling fluid, and the moderator. In Table 1.1 are reported the main features of each type of reactor and their diffusion.

The most diffused type of reactor is by far the Pressurized Water Reactor (PWR) with 307 operable reactors as of May 2023, representing a total installed capacity of 292.8 GW_e. This type of reactor uses enriched uranium dioxide as a fuel, and ordinary water both as a coolant and a moderator. Figure 1.5 is a schematic representation of a PWR reactor. Water reaches about 325°C in the core, and since boiling must be prevented in this type of reactor, the coolant is kept at around 150 times the atmospheric pressure. The pressure is guaranteed by a steam pressurizer. The core coolant flows at the hot side of the steam generator, heat is transferred to the cold side, and the coolant is sent back to the core, where it restarts the cooling cycle (this is called "primary circuit"). Water from the secondary circuit enters the cold side of the steam generator, where is transformed in steam by the heat from the core coolant. This steam is sent to a turbine, where it is expanded, and then is sent to the condenser, where it turns back to water and restarts the cycle. The turbine drives an electric generator, which produces electricity.

Table 1.1 - Classification and diffusion of nuclear reactors [16]

Reactor Type	Pressurized Water Reactor (PWR)	Boiling Water Reactor (BWR)	Pressurized Heavy Water Reactor (PHWR)	Light Water Graphite Reactor (LWGR)	Advanced Gas-cooled Reactor (AGR)	Fast Neutron Reactor (FNR)	High temperature Gas-cooled Reactor (HTGR)
Fuel	enriched UO_2	enriched UO_2	natural UO_2	enriched UO_2	Natural U (metal), enriched UO_2	PuO_2 and UO_2	enriched UO_2
Coolant	water	water	heavy water	water	CO2	liquid sodium	helium
Moderator	water	water	heavy water	graphite	graphite	none	graphite
Operable reactors in May 2023	307	60	47	11	8	2	1
Total installed power [GW_e]	292.8	60.9	24.3	7.4	4.7	1.4	0.2
Main countries	USA, France, Japan, Russia, China, South Korea	USA, Japan, Sweden	Canada, India	Russia	UK	Russia	China

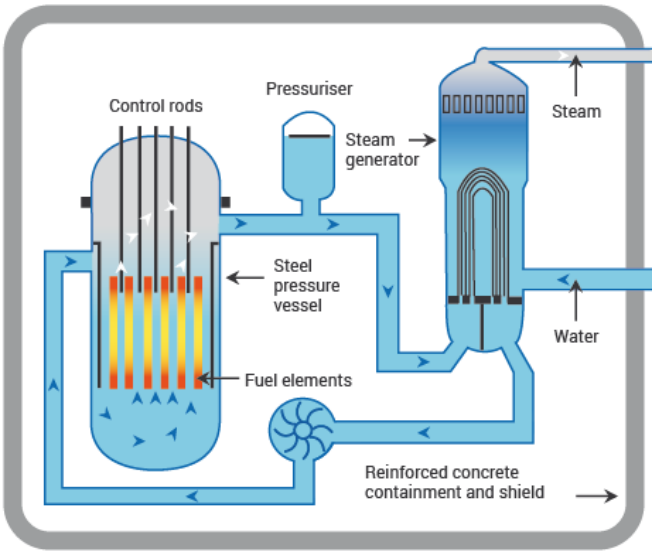

Figure 1.5 - Schematic representation of a PWR [16]

A NPP produces negligible quantities of waste compared to other energy sources, around 10,000 times less than a coal plant of the same size on an annual basis. However, high-level nuclear waste (HLW) has several undesirable characteristics and potentially represent an environmental risk. Therefore, proper management and safe decommissioning of HLW and spent nuclear fuel (SNF) are the major aspects of energy production by NPPs.

Several countries consider SNF as a waste and, instead of reprocessing it, they plan to dispose it in deep geological formations. However, this solution could become problematic given the increase in use of nuclear power. A more sustainable solution is the reprocessing of SNF to recover uranium and plutonium, and then the conditioning in the form of HLW containing mainly fission and activation products, and so-called minor actinides. Furthermore, recycling helps reduce hazardous waste storage and reduces environmental pollution [17].

2. Integration of Small Modular Nuclear Reactors and SOEC

2.1 Small Modular Nuclear Reactors

A small modular nuclear reactor (SMNR) is a type of nuclear reactor characterized by a smaller size and a modular design. Usually, the acronym used to refer to this type of reactor is SMR (small modular reactor), emphasizing its natural suitability for modular deployment. However, this abbreviation has already been used in this work for steam methane reforming, therefore the acronym SMNR has been proposed to solve this conflict. The International Atomic Energy Agency (IAEA) uses the acronym to refer to "small" and "medium" reactors, indicating nuclear reactors with powers below 300 MW_e and 700 MW_e, respectively, recognizing that the boundary between them is relatively labile [18].

Traditional large-scale NPPs have typical electric capacities around 1 GW_e or more, while SMNRs are designed for power generation on a smaller scale, typically in the range between 10 and 300 MW_e. Their modular design allows to meet various power demands through the combination of different smaller reactor units, enhancing constructability and phased deployment [19].

Major stakeholders involved in the decision-making process in the nuclear energy sector consider that SMNRs are a viable option for the expected large replacement of the ageing fossil-fuelled power plants and are to play an integral role with the VRE on the electrical grid [19].

Moreover, on October 4th, 2023, Edison Energia S.p.A. announced the goal of installing and starting operation of two SMNRs with a power of 340 MW each between 2030 and 2040, possibly representing the return of nuclear in Italy [20].

In the next paragraphs, a more accurate description of their characteristics and the advantages linked to their deployment will be provided.

2.1.1 Main characteristics

As already mentioned, the main differences of a SMNR with respect to a traditional large-scale nuclear reactor lie in the smaller size and the modularity, which also represent the driving forces in the development of SMNRs. These factors allow for in-factory fabrication rather than in situ like for traditional large-scale reactors, shortening the design-to-market phase and the construction time. On absolute cost basis, SMNRs are a lower-cost nuclear option and allow lower upfront capital costs, with an estimated decrease in capital expenditures of 5-10% for each cumulative doubling of production. The smaller size and modular structure of SMNRs allow for an incremental deployment to closely match increasing energy demand, resulting in a moderate financial commitment for countries or regions with smaller electricity grids [19]. The mitigation of financial risk associated with traditional large-scale NPPs could be significantly reduced by SMNRs, allowing them to effectively compete with other energy sources [21].

These features also allow for an increased operational flexibility, making SMNRs a technically sound option to cope with the shortcomings of VRE, both in base and load-following mode. Indeed, traditional NPPs already have an embedded capability to perform load follow and load rejection from the grid, meaning that SMNRs have at least a similar load-following capability as advanced large-scale reactors [19]

The lower thermal power output allows for a decreased discharge of warm cooling water from the hot side of the condenser to the ultimate heat sink, resulting in more opportunities for siting and a reduced environmental impact. These factors are positively affected by other factors (some of them are still under development) such as longer fuel cycles, different refuelling schemes (both on-site or not), transportable units or components, in-factory fabrication, smaller civil structures, less detrimental effects on the land due to construction, lower land requirements and reduced emergency planning zone size [19].

One last significant aspect of SMNRs is increased safety, as advanced designs incorporate safety features aiming to reduce or even eliminate any reliance on off-site power. This means that the active safety systems within the NPP do not rely on continuous or secure off-site power in the short or medium-term, significantly simplifying and reducing the electric grid requirements [19]. However, this only represents the las tier of safety, as two previous safety steps are usually adopted: safety-by-design, which intrinsically eliminates incidents through design, without having to cope with their consequences; and passive safety systems which shield against the remaining potential accidents and mitigate their consequences [18].

2.1.2 Hybrid nuclear-renewable energy systems

When coupled with VREs, SMNRs can create synergisms among technologies as a flexible base-load supply for electricity generation along with other co-products (when considering cogeneration applications), promoting low-to-zero carbon energy production and enhance supply security. Such a hybrid system would allow to fully exploit the inherent qualities of SMNRs (discussed in section 2.1.1) with positive effects on protection against supply disruptions and its economic sustainability, electricity price volatility, and reduce fuel import.

As already explained in section 1.3, a high penetration of VRE makes grid balancing and utilization of excess power particularly difficult. This effect is even more pronounced in small or decentralized energy systems, which do not benefit from a flatter demand and a smoother VRE generation profile. Hybridization with SMNRs would allow to overcome the issues linked to fluctuations in power production while providing inertia to the grid. Moreover, this type of hybrid system would boost the use of excess power for other applications beyond power generation and in energy storage [19], as will be later discussed.

Lastly, a synergy can also be created in land use. Since NPPs need to have an exclusion zone around them (which is reduced in the case od SMNRs), whenever possible, this area could be used as a site for VREs. Usually, VREs have low energy density factors, meaning that they require vast areas to produce large quantities of electricity, and siting could become a problem. The use of exclusion zone around a NPP is prevented for several industrial activities, so it could be potentially used for energy production through VRE. Of course, VRE operation must be compliant with the safety regulations of the NPP (e.g., attention must be paid to the moving blades of a wind farm) [19].

2.1.3 Current deployment and future development

More than 80 designs for commercial SMNRs are currently being developed in 19 countries, targeting different sizes and applications [22].

The first NPP ever being powered by a SMNR was Akademik Lomonosov in Pevek, Russia. This is also the first floating NPP in the world and began operation in December 2019, generating both electricity and heat with two PWR-type KRT-40S reactors with a gross power of 35 MW_e each. The NPP was connected to the grid and started commercial operation in May 2020 [23].

Since then, three more SMNRs have become operative: CNP-300 (a 300 MW_e PWR), PWHR-220 (a 220 MW_e PWHR) and RITM-200 (a 50 MW_e integral PWR for civil marine) [24].

Other SMNRs are under construction or in licensing phase in many countries, and two SMNRs are in advanced construction phase.

The first one is CAREM in Zarate (Argentina): it is an integral PWR with a gross electric power of 100 MW_e (this model follows a smaller 30 MW_e prototype [23]) developed by the National Atomic Energy Commission (CNEA), representing the first nuclear reactor ever designed in Argentina.

The second one is HTR-PM, a high temperature gas-cooled reactor with a 210 MW_e capacity in People's Republic of China [23].

In Western countries, SMNR development is proceeding with significant private investment, indicating a profound shift from nuclear R&D led and funded by governments to that led by the private sector and people with strong entrepreneurial goals. Technology roadmaps promote enhanced collaboration, knowledge sharing and help to ensure that the efforts are focused on a common objective. The driving forces in the development of SMRs is often deployment of affordable clean energy, with low carbon dioxide emissions [19], [24].

2.2 Water electrolysis

Water electrolysis is an electrochemical process in which water molecules are split in oxygen and hydrogen according to the following reaction:

$$H_2O \rightarrow \frac{1}{2}O_2 + H_2 \tag{2.1}$$

This process is not spontaneous, so it needs to be driven by an external source of energy represented by a direct electric current.

There are different technologies available on the market to perform such a process, each of them with its own peculiarities. The range of options for green/purple hydrogen production can be narrowed down to alkaline (ALK) water electrolysis, anion exchange membrane (AEM) water electrolysis, proton exchange membrane (PEM) water electrolysis, and solid oxide water electrolysis. A general overview of each of these technologies will be provided in the following.

2.2.1 Alkaline water electrolysis

ALK water electrolysis is a well-established and long-known technology dating back to 1789, making it mature and widely used. The process is performed by cells consisting of two electrodes (namely anode and cathode) separated by a thin, porous diaphragm (or separator), and submerged in a liquid electrolyte, that is a

concentrated alkaline solution of potassium or sodium hydroxide (5M KOH/NaOH), in the presence of electricity. The electrolysis process consists of two individual half-cell reactions: hydrogen evolution reaction (HER) at the cathode, and oxygen evolution reaction (OER) at the anode.

First, two moles of water are reduced at the cathode side, producing a mole of hydrogen (H_2) and two moles of hydroxyl ions (OH^-):

$$HER: \ 2H_2O + 2e^- \rightarrow H_2 + 2OH^- \tag{2.2}$$

Then, hydrogen is released from the cathode surface and, under the electric circuit effect between the electrodes, OH^- ions move to the anode side through the diaphragm due to its positive attraction. Here, the ions are recombined into half a molecule of oxygen and one molecule of water:

$$OER: \ 2OH^- \rightarrow H_2O + \frac{1}{2}O_2 + 2e^- \tag{2.3}$$

Figure 2.1 is a schematic illustration of the ALK cell and of the reactions taking place inside of it.

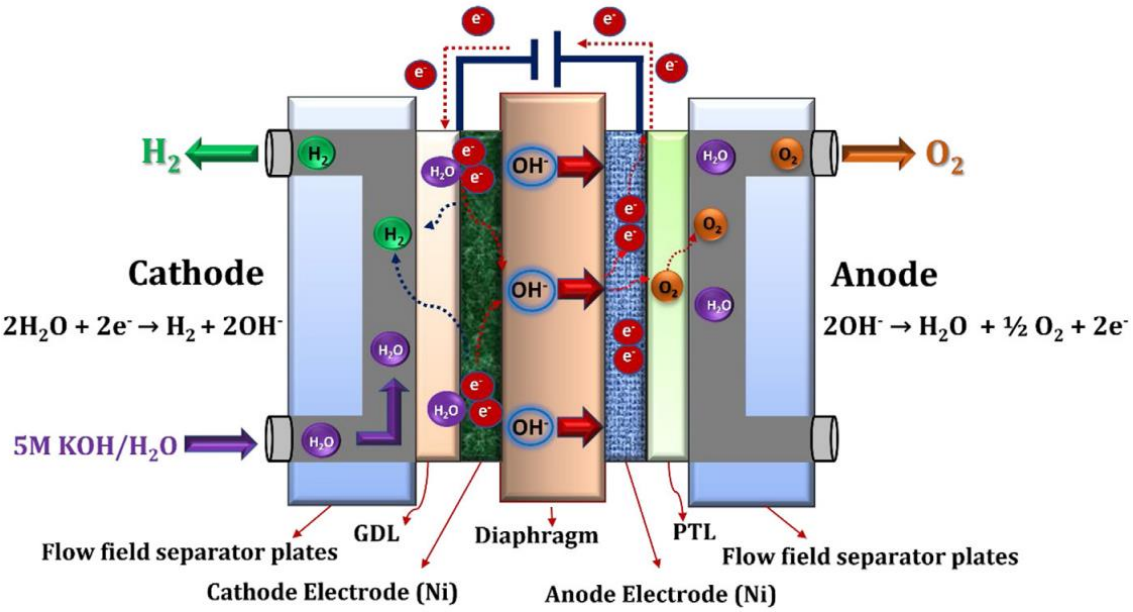

Figure 2.1 - Scheme of an ALK cell [25]

Usually, the electrodes are made of perforated stainless-steel plates coated in nickel, the bipolar plates made of stainless-steel plates (sometimes covered in nickel), the gas diffusion layer is a nickel mash, and the diaphragm is made of Asbestos, nickel or Zirfon (state of the art).

ALK cells have an electrode area of 10,000-30,000 cm^2, operate between 70°C and 90°C with ranges of voltages and current densities of 1.4-3.0 V and 0.2-0.8 A/cm^2, respectively. Efficiency is in the 58%-70% range, expected stack lifetime is 60,000 h or more, and the achieved hydrogen purity is in the 99.5-99.9998% range [26].

Given its long-time industrial use and its maturity, ALK water electrolysis is a strong candidate for large-scale applications, with investment costs of 500-1000 USD/kWh. ALK water electrolysis also benefits from its long-term stability and its noble metal-free electrocatalysts.

However, ALK technology presents low operative current density due to the corrosive electrolyte (KOH) and low OH^- ions mobility. Moreover, KOH is highly reactive with ambient carbon dioxide, causing the formation of K_2CO_3 salt which occludes the pores of the anode gas diffusion layer, resulting in the decrease of OH^- ions formation, ionic conductivity, and hydrogen formation. Lastly, the diaphragm does not fully prevent gasses crossover between the two halves of the cell, resulting in poor hydrogen quality [26].

2.2.2 Anion exchange membrane electrolysis

AEM water electrolysis is a recent technology, with its first journal publication only dating back to 2011.The working principle and the reactions are the same as in ALK technology, however materials used in the cell are different and allow for the use of a DVB polymer support with a less concentrated electrolyte (1M KOH/NaOH), a significant advantage with respect to ALK [26].

Figure 2.2 is a schematic illustration of the AEM cell and of the reactions taking place inside of it.

Compared with an ALK cell, in a AEM cell the diaphragm is substituted by an anion exchange membrane, typically a quaternary ammonium ion exchange membrane (Sustanion®, Fumasep or Fumatech). Cathode is in nickel, while anode is in nickel or NiFeCo alloys. The gas diffusion layer is a nickel foam or a carbon cloth, the bipolar plates are in stainless-steel, while end plates are in nickel-coated stainless-steel.

AEM cells have an electrode area of less than 300 cm^2, operate between 40°C and 60°C with ranges of voltages and current densities of 1.4-2.0 V and 0.2-2.0 A/cm^2, respectively. Efficiency is in the 57%-59% range, expected stack lifetime is 30,000 h or more, and the achieved hydrogen purity is in the 99.9-99.9999% range. The capital cost is still unknown for a MW scale or larger [26].

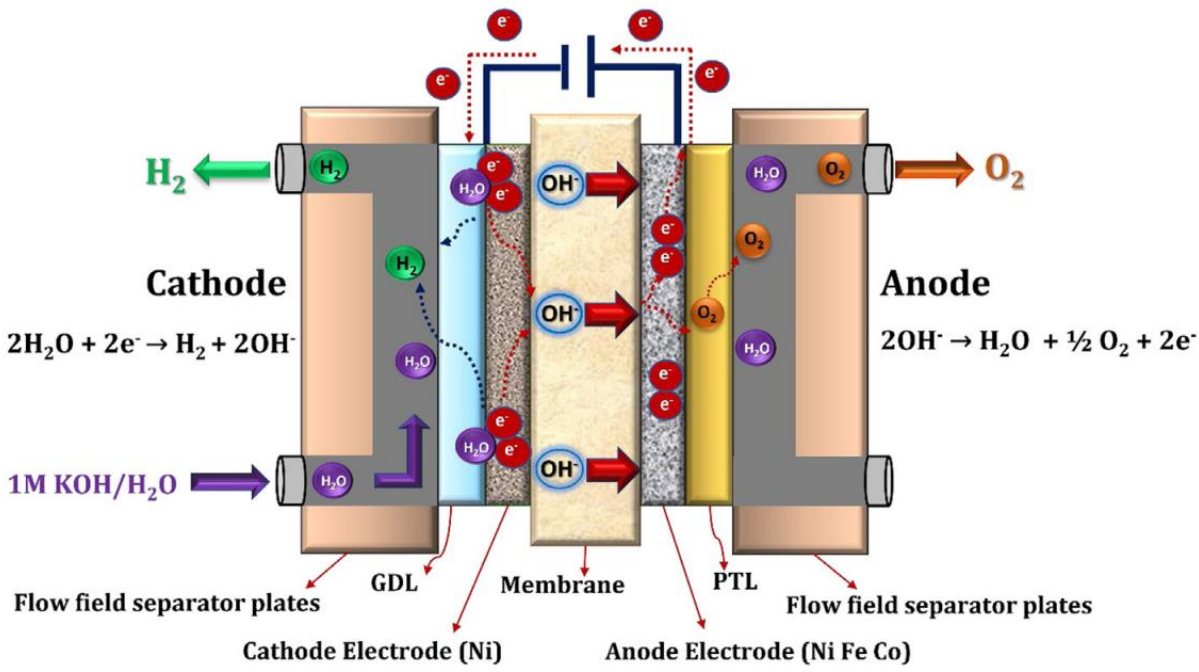

Figure 2.2 - Scheme of an AEM cell [25]

2.2.3 Proton exchange membrane electrolysis

The first idea of PEM water electrolysis was developed by General Electric in the 1960s to overcome the drawbacks associated with ALK technology. A PEM cell can be imagined as two electrodes (namely cathode and anode) separated by a solid polymer electrolyser (SPE).

Even though the overall water hydrolysis reaction is the same as for the ALK and AEM technologies, the intermediate reactions are different. The OER takes place at anode side, where a water molecule is supplied to the catalyst and oxidised in half a molecule of oxygen, two protons and two electrons:

$$OER:\ H_2O \rightarrow \frac{1}{2}O_2 + 2H^+ + 2e^- \tag{2.4}$$

At this point, oxygen is removed from the anode, while protons and electrons travel to the cathode through the proton-conducing membrane and an external circuit, respectively. The HER takes place at cathode side, where protons and electrons react to form a hydrogen molecule:

$$HER:\ 2H^+ + 2e^- \rightarrow H_2 \tag{2.5}$$

Figure 2.3 is a schematic illustration of the PEM cell and of the reactions taking place inside of it.

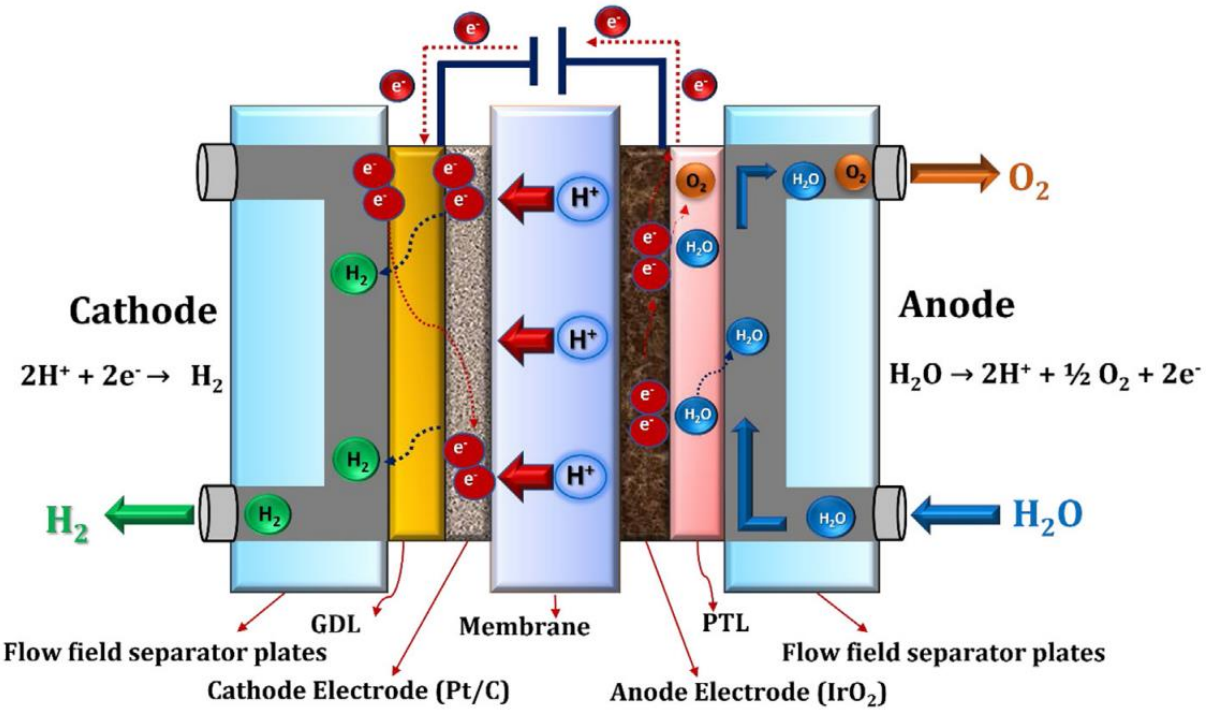

Figure 2.3 - Scheme of a PEM cell [25]

The proton exchange membrane not only allows the passage of protons from anode to cathode, but also provides electrical insulation of the electrodes and separates product gases. This membrane is typically in Nafion® due to its high proton conductivity, mechanical strength, chemical stability, and high current density, but membranes in Fumapem®, Flemion® and Aciplex® also exist.

The state-of-the-art technology for the electrodes involves the use of noble metals. In particular, the cathode uses carbon-supported platinum as a catalyst, while the anode uses iridium oxide (IrO_2). This, however, is a significant drawback as iridium is even more expensive than platinum. Indeed, a 10 MW PEM water electrolyser working at 1 A/cm^2 of current density with an assumed catalyst loading of 2-3 mg/cm^2 would require the use of 15 kg of iridium that, with a price of 196,119 USD/kg (price in August 2021), would imply a cost of 2,941,789 USD [26].

Anode and cathode diffusion layers consist of porous titanium or a titanium mesh and a carbon cloth, respectively. Bipolar plates are made of titanium coated in platinum (separators) or gold (end plates). Several flow field designs have been developed, with the straight parallel flow showing the best performances. However, these separator plates are extremely expensive given the materials involved, representing up to 48% of the overall cell cost [26].

PEM cells have an electrode area of 1500 cm^2, operate between 50°C and 80°C with ranges of voltages and current densities of 1.4-2.5 V and 1-2 A/cm^2, respectively. Efficiency is in the 50%-83% range, expected stack lifetime is 50,000-80,000 h, and the achieved hydrogen purity is in the 99.9-99.9999% range. Capital costs are around 400 USD/kW for stack of 1 MW minimum, and 700-1400 USD/kW for stacks of 10 MW minimum [26].

If compared to ALK technology, PEM benefits from faster HER kinetics caused by the highly reactive electrode surface (due to the presence of Pt) and a lower pH of the electrolyte. Moreover, PEM cells are more compact, safer due to the absence of caustic electrolytes. Stability is very good, with negligible loss of performances up to 60,000 h and a target of 1,000,000 h. However, despite being a commercialized technology, the materials involved represent a major drawback for this technology, and further research on the matter is needed to reduce costs [26].

2.2.4 Solid oxide electrolysis

Solid oxide technology was introduced by General Electric and Brookhaven National Laboratory in the 1970s and uses Solid Oxide Electrolysis Cells (SOEC) to perform water hydrolysis. In contrast to the other above-cited technologies, SOECs use water in the form of steam and have significantly higher operative temperatures (500-900°C): for this reason, this technology is also referred to as high temperature steam electrolysis (HTSE).

SOECs are composed of three main parts: two porous electrodes (namely cathode and anode), and a dense ceramic electrolyte able to conduct oxide ions. The hydrolysis reaction is composed, as usual, by two half reactions. First, at cathode side, a water molecule is reduced by two electrons and forms a hydrogen molecule and an oxide ion:

$$H_2O + 2e^- \rightarrow H_2 + O^{2-} \tag{2.6}$$

Hydrogen is released, while the oxide ions pass through the electrolyte to the anode side. Here, ions react to form half an oxygen molecule and two electrons:

$$O^{2-} \rightarrow \frac{1}{2}O_2 + 2e^- \tag{2.7}$$

Figure 2.4 is a schematic illustration of a SOEC and of the reactions taking place inside of it.

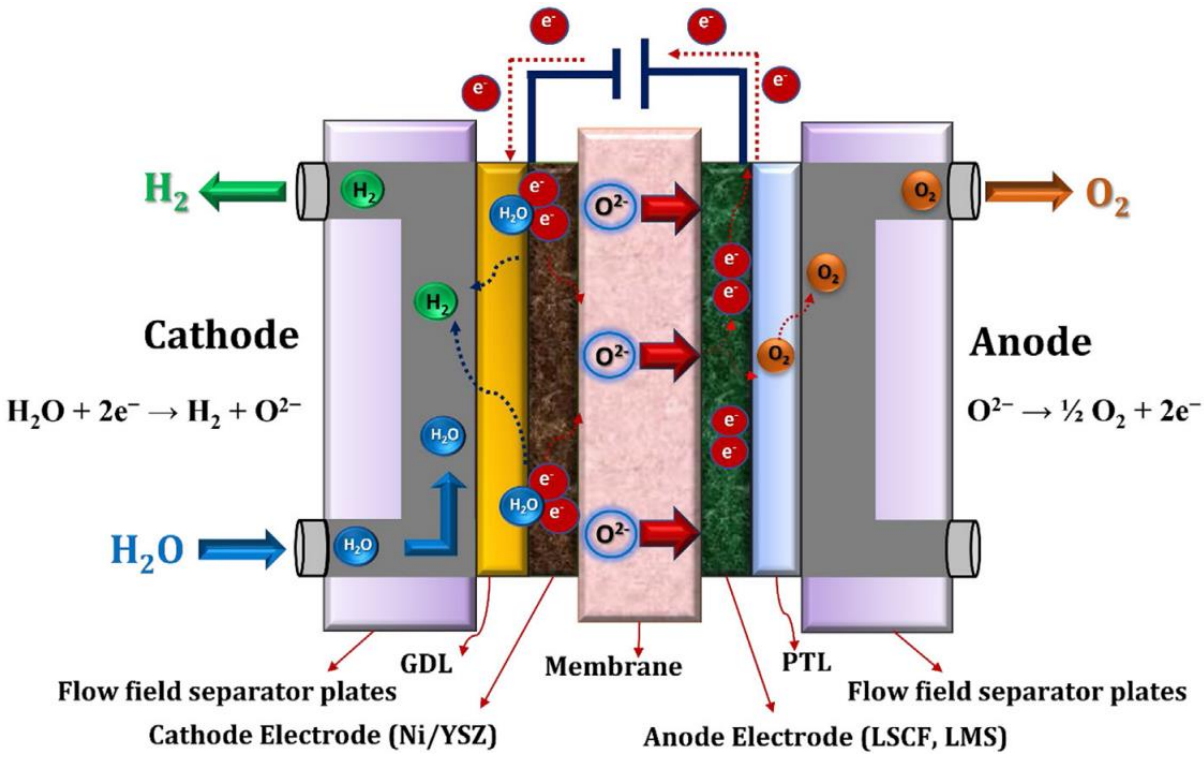

Figure 2.4 - Scheme of a SOEC [25]

The electrolyser is usually made of yttria-stabilized zirconia (YSZ), a material with high ionic conductivity, allowing for good thermal and chemical stability even at high operative temperatures. The state-of-the-art cathode is made of a ceramic metal composed of nickel and YSZ (Ni-YSZ), a non-noble metal with high electronic conductivity. The anode is usually in perovskite materials, typically LSM.

SOECs have an electrode area of 200 cm^2 maximum, operate between 500°C and °C with ranges of voltages and current densities of 1-1.5 V and 0.3-1 A/cm^2, respectively. Efficiency is around 89% (laboratory), expected stack lifetime is in the range of 20,000 h, and the achieved hydrogen purity is 99.9%. Capital costs are still undetermined for stacks in the MW scale [26]

The high-temperature operation allows this technology to drastically reduce the energy demand to perform water electrolysis, leading to a reduction in power usage (which is the main cost associated with hydrogen production) and, consequently, to an unmatched energy efficiency. High temperatures are also beneficial for conversion efficiency as they allow for favourable thermodynamics and reaction kinetics. Moreover, this technology does not require the use of noble materials. However, SOECs are still in development phase and yet to be commercialized for industrial-scale applications.

Nonetheless, the significant advantages offered by this technology in a future perspective, with green/purple hydrogen production to grow significantly by 2050, makes SOECs the hydrogen production technology of choice for this work. For this reason, a more detailed analysis SOECs will be provided in the following.

Table 2.1 provides an overall panoramic on the four water electrolysis technologies introduced, allowing for a quick comparison between them.

Table 2.1 - Main characteristics of technologies for water electrolysis

Technology	ALK	AEM	PEM	SOEC
Nominal current density	0.2-0.8 A/cm²	0.2-2.0 A/cm²	1.0-2.0 A/cm²	0.3-1.0 A/cm²
Voltage range	1.4-3.0 V	1.4-2.0 V	1.4-2.5 V	1.0-1.5 V
Operating temperature	70-90°C	40-60°C	50-80°C	500-900°C
Electrode area	10,000-30,000 cm²	<300 cm²	1500 cm²	200 cm²
Efficiency	50-78%	57-59%	50-83%	89% (laboratory)
Hydrogen purity	99.5-99.9998%	99.9-99.9999%	99.9-99.9999%	99.9%
Development	Mature	R&D	Commercial	R&D

2.3 Analysis of solid oxide electrolysis cells

Given the advantages of SOECs for hydrogen production with respect to the other technologies discussed in section 2.2, a more exhaustive analysis of this technology will be now provided.

For these cell to perform water electrolysis, a voltage needs to be applied to the cell, meaning that electric power is required to drive the chemical reaction. The reactions happening at anode and cathode sides, respectively, have already been introduced together with the general reaction for water electrolysis, so the focus can move on the thermal behaviour of these cells. To do so, the equation for Gibbs' free energy (ΔG) for electrolysis can be introduced:

$$\Delta G = \Delta G^0 + R \cdot T \cdot \ln(Q_R) \ [J] \tag{2.8}$$

This represents a thermodynamic potential that measures the maximum reversible work that can be performed by a system at constant temperature and pressure. The

first term in Equation (2.8) first term represents the Gibbs' free energy if reactants and products are all in their thermodynamic standard states, R is the universal gas constant (8.314 J/mol K), T is the temperature [K] and Q_R is the reaction quotient, which for water electrolysis can be expressed as:

$$Q_R = \frac{a_{H_2O}}{a_{H_2} \cdot a_{O_2}^{0.5}} \tag{2.9}$$

The coefficients in Equation (2.9) are the stoichiometric coefficients of the balanced water electrolysis reaction (reactants at numerator and products at denominator). Two equations can be written to express the relation between Gibbs' free energy and the cells potential:

$$\Delta G = -n \cdot F \cdot E_{cell} \tag{2.10}$$

$$\Delta G^0 = -n \cdot F \cdot E_{cell}^0 \tag{2.11}$$

In these equations, n [mol] is the number of moles transferred in the reaction, F is the Faraday's constant (96.485 C/mol) and E_{cell} [V] is the cell potential, while E^0_{cell} [V] is the standard cell potential under standard conditions and can be expressed as:

$$E_{cell}^0 = \frac{\Delta H_f^0}{2F} \tag{2.12}$$

Where ΔH^0_f is the enthalpy of formation. Equations (2.10) and (2.11) can be combined to express Nernst's law, which relates the equilibrium cell potential of an electrochemical cell to the standard cell potential, temperature, and the concentration of ions involved in the electrochemical reaction:

$$E_{cell} = E_{cell}^0 - \frac{R \cdot T}{n \cdot F} \cdot \ln(Q) \tag{2.13}$$

Renaming the cell voltage as V_{Nernst} and E^0_{cell} as V_{tn} (the thermoneutral voltage, which will be later discussed), the following equation for the reaction heat flux Q_{react} [W/m^2] can be written:

$$Q_{react} = j \cdot 2F \cdot T \cdot \Delta S = j \cdot 2F(\Delta H \cdot R + \Delta G) = j \cdot (V_{tn} - V_{Nernst}) \tag{2.14}$$

Where ΔS [J/K] is the entropy variation in the electrolysis reaction (which depends on the temperature of the process as well as on the partial pressures of the reactants and the products) and j is the current density [A/cm^2].

The polarization heat flux Q_{loss} [W/m^2] accounts for the losses associated to overpotentials (Joule effect) and other non-ohmic irreversibilities. This quantity can be expressed as:

$$Q_{loss} = j \cdot (V - V_{Nernst}) \quad (2.15)$$

The difference between Equation (2.14) and (2.15) gives the cell net thermal flux of the SOEC, Q_{SOEC}:

$$Q_{SOEC} = Q_{react} - Q_{loss} = j \cdot (V_{tn} - V) \quad (2.16)$$

This value can either be positive, negative, or null. According to Equation (2.16), three different ranges for operating voltage applied to the cell can be distinguished. The first region is for $V<V_{Nernst}$, and no water electrolysis can happen for these values of applied voltage.

The second range is for $V_{Nernst}<V<V_{tn}$, where electrolysis is possible by also providing heat to the cell ($Q_{SOEC}>0$): the cell has an endothermic behaviour, and this region is hence referred to as "endothermic region".

A peculiar condition is achieved for $V=V_{tn}$. The cell is adiabatic, and the heat generated by irreversibilities is enough to sustain the electrolysis reaction: the cell has a thermoneutral behaviour and the value of voltage at which this situation occurs is hence referred to as "thermoneutral voltage", as already hinted above. In this condition, electric power input to the cell perfectly matches the whole enthalpy change in the electrolysis reaction.

The third range is for $V>V_{tn}$, where electrolysis happens with heat dissipation from the cell due to losses. This causes an increase in the temperature of the process, unless heat is removed ($Q_{SOEC}<0$) by a cooling system and released to the atmosphere: the cell has an exothermic behaviour, and this region is hence referred to as "exothermic region".

One major consequence of this distinction is that operation is possible by partially offsetting the electric energy consumption with thermal power. This means that when the cell is operating in the endothermic region, a portion of the heat demand is produced by internal irreveribilities, decreasing the share of heat that must be provided by external sources, increasing the cell efficiency. However, operation in this region requires a larger stack size to support hydrogen production, causing investment costs to increase: a trade-off between increased efficiency and increased costs is necessary to find the optimal configuration.

It is important to point out that the fuel stream (cathode-side) does not consist of pure water, but it also includes a variable share of hydrogen which is needed to maintain a reducing environment. Indeed, the fuel gas composition is an important design parameter which affects the cell performances and durability, as high ratios of H_2O/H_2 accelerate the degradation process of the cathode due to microstructural

changes. In this work, a fuel composition of 90% water and 10% hydrogen on a molar basis was adopted.

Another important parameter to consider when dealing with SOECs performances is the steam utilization factor (UF), which is defined as:

$$UF = \frac{n_{H_2,out}}{n_{H_2O,in}} = \frac{\frac{j \cdot A \cdot a}{2F}}{x_{H_2O} \cdot n_{H_2O,in}} \tag{2.17}$$

This quantity expresses the conversion rate as the ratio of outlet moles of produced hydrogen over the inlet moles of water (e.g., for UF=0.7, 7 moles of hydrogen are produced every 10 moles of water entering the cell). Remembering that one mole of molecular hydrogen can be obtained from one mole of water, UF can also be thought as the ratio between the actual hydrogen production over the amount that could be produced under ideal conditions. So, in a sense, it is a measure of how effectively the cell is converting electrical energy into hydrogen. The UF affects the cell operating voltage and its efficiency, making it a crucial parameter for the SOEC operation: its value should be carefully evaluated to maximize the system efficiency.

2.3.1 Types of cells

One first major distinction can be made on the shape of SOECs, which can be either planar or tubular. The first SOECs were developed with a tubular shape to solve the issues related to gas sealing, as the produced H_2 should be separated from O_2, and offered better mechanical strength of the cell, providing enhanced integrity.

However, planar cells have an easier manufacturing process and a better flexibility for scaling and potentially allow for a greater cost reduction. Moreover, this type of cells can be arranged in planar stacks with a smaller volume, making them easier to handle and manage. Lastly, planar cells also reduce the current path, providing a lower Ohmic resistance within the cell. For these reasons, this type of cells is the most used and investigated among the two.

Sticking to planar cells, as already discussed in section 2.2.4, a SOEC can be imagined as consisting of three layers: two electrodes (a cathode and an anode) with a solid oxide electrolyte placed between them. From here, a first distinction can be made between electrode-supported and electrolyte-supported cells, depending on which layer provides structural support.

An electrolyte-supported cell (ESC) employs the electrolyte as the support structure, which is the thickest structure in the cell. This type of cell is suitable for high temperature operation, which helps to reduce the (often large) Ohmic resistance associated with a thick electrolyte.

In an electrode-supported cell, on the other hand, one of the electrodes is the thickest part of the solid structure. Such a design has been developed to minimize Ohmic resistances in solid oxide fuel cells (SOFCs) operating at intermediate temperatures, but it can also be applied to intermediate temperature SOECs [27]. In this category, a further distinction can be made between cathode-supported cells (CSCs) and anode-supported cells (ASCs) according to which electrode provides the structural support.

Usually, CSCs offer flexibility in the choice of materials and better electrochemical performances. However, this type of cells suffers from anode delamination at high current densities due to enormous gaseous oxygen formation at the anode-electrolyte interface. The loss of adhesion is caused by the low sintering temperatures used to ensure high anode porosity, and cathode pulverization due to potential nickel redox reaction [28].

Since operation at high current densities is beneficial for hydrogen generation, technologies to support such operating conditions are being researched. In this context, ASCs offer better mechanical stability with respect to CSCs and could represent a solution to achieve high operating current densities without affecting the cells integrity. these, the ASCs could allow operation at high current densities while solving the. As an example, ASCs with firm anode-electrolyte interface are being investigated. This type of structure allows the co-sintering of anode support and electrolyte at high temperatures to form strong interface adhesion, allowing to reach current densities up to 2.5 A/cm^2 [28]. However, this technology is still marginal and the SOEC industry is focusing on CSCs due to their better performances and cost reduction potential.

Figure 2.5 provides a schematic representation of the three types of SOECs according to the element which provides structural support.

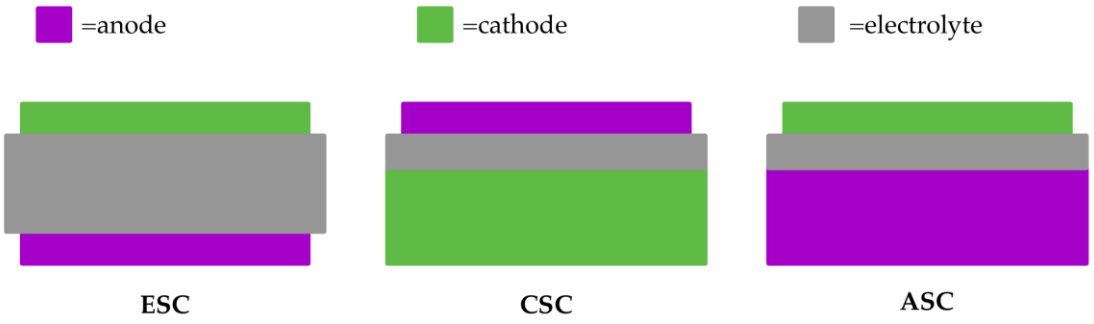

Figure 2.5 - Types of SOECs

2.3.2 Polarization curve

The polarization curve is a crucial tool to assess the electrochemical performances of a SOEC. It illustrates the relationship between cell voltage [V] (usually reported on the y-axis) and current density [A/cm^2] (usually reported on the x-axis) during the electrolysis process under steady state or dynamic conditions.

The value of the operating voltage hen the SOEC circuit is open, and no current is provided to the cell (j=0 A/cm^2), is called open circuit voltage (OCV).

As current density is increased and electric power is provided to the cell, the value of the operating voltage starts to diverge from the OCV. This is caused by the polarization losses of the cell, which are caused by three different phenomena predominantly occurring in three different areas of the plot. At low values of current density, the so-called activation losses are predominant. Then, as current density increases, Ohmic losses become predominant and linearly increase with j. The, at very high values of current density, the concentration losses become predominant as the reactants in the electrodes get depleted.

The sum of the polarization losses is called overpotential, indicating that the cell requires more energy than thermodynamically expected to perform the electrolysis reaction. This, of course, is caused by the above-mentioned losses. Figure 2.6 shows several experimental polarization curves taken from literature for different types of cells, operating temperatures, operating pressures, and anode-side gas composition. All of them refer to a fuel composition of 90% water and 10% hydrogen on a molar basis at cathode side, as already hinted in section 2.3. The black horizontal line in the middle of the figure represents the thermoneutral voltage, which is equal to 1.29 V. The region below V_{tn} is the endothermic region, while the one above V_{tn} is the exothermic region.

The polarization can be approximated as a straight line on the range of current densities of interest (below 1.1 A/cm^2), as strong deviations only occur for values of j well above the usual operating values. The slope of these lines is expressed by the area-specific resistance (ASR, [Ω cm^2]). This quantity can be determined by measuring the voltage drop across the cell for a given current density and can be used to express the electrochemical performances of a cell. The lower is the slope of the curve, the higher is the efficiency of the cell. The values for the OCV of the linearized curves and their ASR are reported in Table 2.2

The linearization process causes to overestimate the actual OCV of the cell, as the actual polarization curve bends downwards when in proximity of the y-axis. However, this effect is not particularly relevant as operation at such low values of current density is extremely unusual for practical applications, while the curve is

well approximated at values of current densities typical of actual operating ranges. Moreover, the behaviour around OCV is similar for all the curves as they all operate with air at anode side. The only exception is represented by the curve for cell number 4 operating with only oxygen at anode side.

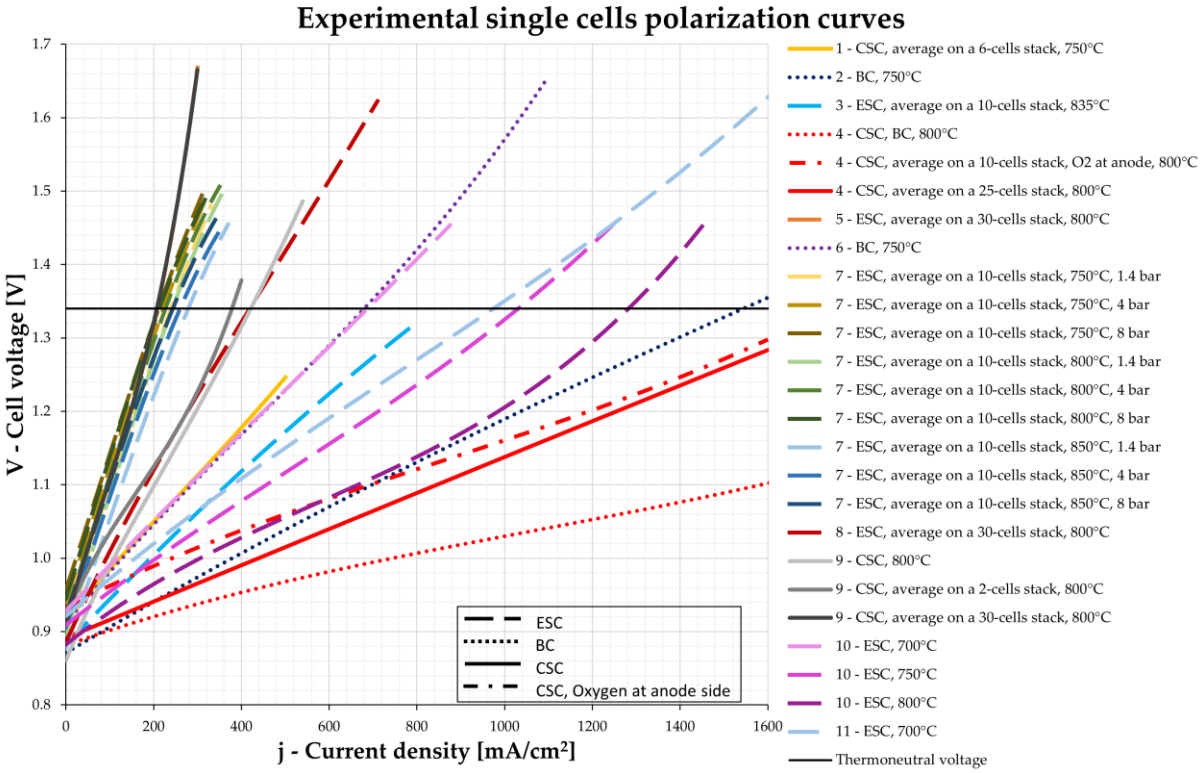

Figure 2.6 - Experimental polarization curves

When looking at the groups of curves for the same cells under different operating conditions, a few considerations can be made by keeping all the other parameters unchanged. Higher temperatures positively affect the cells' performances (e.g., the slope of the curves for cell number 7 decreases as temperature rises) as they allow for better thermodynamics and kinetics of the electrolysis reaction.

On the contrary, higher pressures cause the slope to increase (hence, efficiency to decrease). However, this effect is much less evident than that of temperature. Indeed, in the logic of a whole hydrogen production plant, operation at higher pressures could become favourable as hydrogen is stored at high pressure, and already producing it at high pressures would decrease the compression work and possibly increase the overall efficiency of the system despite the decrease of the cell efficiency. For this reason, performances at high values of pressure are being investigated despite the negative effect on the cells' performances.

Table 2.2 - Data for polarization curves

Curve number	Reference	Cell type	Cells in the stack	Cell dimensions	Active area	Anode-side gas	Operating temperature [°C]	Linearized OCV [V]	ASR [Ω cm²]
1	[29]	CSC	6	-	80 cm²	Air	750	0.868	0.654
2	[30]	BC	-	ϕ = 1,8 mm	-	Air	750	0.851	0.288
3	[31]	ESC	10	-	127 cm²	Air	835	0.899	0.466
4	[32]	CSC	-	ϕ = 5 cm	3.1 cm²	Air	800	0.867	0.113
			10	12 x 12 cm	100 cm²	O_2		0.914	0.196
			25	12 x 12 cm	100 cm²	Air		0.848	0.241
5	[33]	ESC	30	10 x 10 cm	63 cm²	Air	800	0.827	2.386
6	[34]	BC	-	5.3 x 5.3 cm	16 cm²	Air	750	0.878	0.600
7	[35]	ESC	10	-	127.8 cm²	Air	750	0.964	1.413
								0.987	1.423
								1.006	1.413
							800	1.059	1.088
								1.105	1.003
								1.090	1.104
							850	0.997	1.101
								1.081	0.899
								1.064	1.020
8		ESC	30	10 x 10 cm	62 cm²	Air	800	0.867	0.994
9	[36]	CSC	-	10 x 10 cm	63 cm²	Air	800	0.838	1.050
			2			Air		0.873	1.048
			30			Air		0.854	2.460
10	[37]	ESC	-	-	9.08 cm²	Air	700	0.881	0.597
						Air	750	0.858	0.421
						Air	800	0.831	0.347
11	[38]	ESC	-	5 x 5 cm	10.2 cm²	Air	700	0.872	0.442

The number of cells in a stack also affects the performances of the single cells. It can be seen how the button cells (BC), which are small cells tested in a laboratory under extremely controlled conditions, always offer better performances of the respective regular cell. The single cell, in turn, always has a better efficiency when not operating in a stack. This is due to the boundary effects and worst circulation related to stack operation. Moreover, the effect is more and more evident as the number of cells in the stack increases. Curves for cells 4 (the ones referring to operation with air at anode-side) and 9 offer a clear representation of this phenomenon.

Since CSCs currently represent the vast majority of the SOECs on the market, the focus can be entirely moved on the curves for this type of cells, which have been isolated in Figure 2.7 for the sake of clarity.

The curves for cell number 4 highlight how using pure oxygen at anode-side (red dash-dotted line) rather than air (red solid line) contributes to increase the OCV.

The curves for cell number 9, instead, provide a clear representation of how the number of cells in a stack affect its performances: the curves' slope increase as the number of cells in the stacks increases from 1 to 30. This is coherent with what was explained before, as the slope of the curve (and hence its ASR) is proportional to the losses in the cell, which increase with the stack dimensions.

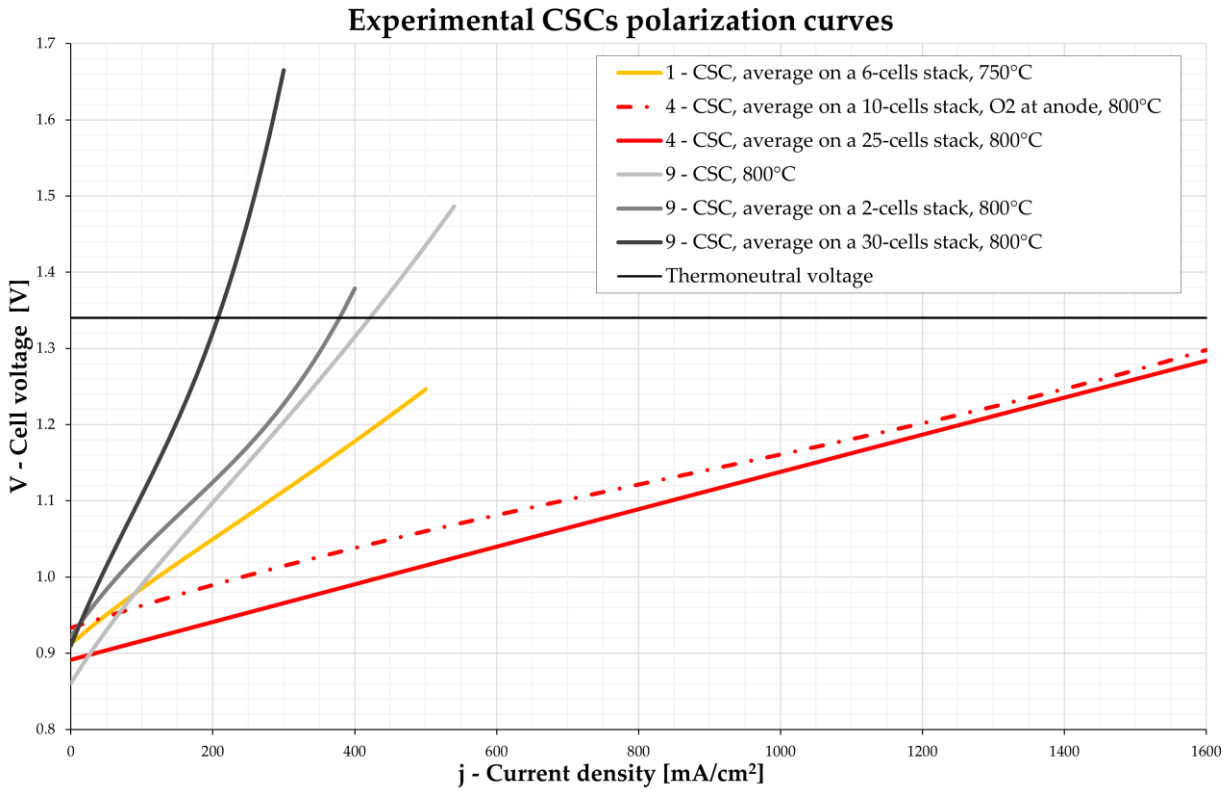

Figure 2.7 - Experimental polarization curves for CSCs

2.3.3 Current limits and future development

When dealing with hydrogen production from SOE, the current target is "$1 for 1kg in 1 decade". This means that efforts are being made to achieve 1 $/kg of hydrogen by 2031, and 2 $/kg by 2026. To achieve this goal, the roadmap plans to solve the current limits of this technology to fully exploit its potential. As already mentioned in the previous sections, the main objectives are to increase efficiency, enhance durability and reduce costs.

A report from the U.S. Department of Energy states that addressing the gaps in research is crucial to enhance manufacturing rates and speed up the deployment of this technology. The limited fundamental knowledge on degradation mechanisms causes a lack of standardized accelerated stress tests, which are crucial to examine cell and stack lifetime in shorter times than the actual average of seven years for existing performance metrics and test designs. Other key barriers to large-scale manufacturing are the fabrication time, the cost, and the automation of stack assembly and quality assurance/quality control (QA/QC). A stack cost of less that 100 $/kW can be achieved by increasing cell size, using advanced fabrication methods, reducing the number of processing steps, QA/QC development, and predictive modelling to aid in manufacturing. Mass-production is one of the key drivers to lower costs, leading to a predicted 80% decrease in system costs related to manufacturing. Other factors such as electricity price, thermal integration, performance and lifetime improvements, and the advances discussed above will also enable a lower LCH (section 1.2.2) [39].

A paper from T. Cui et al. [40] investigates the efficiency of SOE when coupled with different external heat sources. Three different scenarios are proposed: the first does not include any external heat source, and only electric heating is used to perform electrolysis; the second scenario uses a low temperature source to perform water evaporation, but superheating is still performed by electric heating; the third scenario, the only is provided only by a high temperature heat source (such as a SMNR). Each scenario is simulated by also varying some operative parameters: steam utilization, steam concentration at fuel electrode, flow rate of fuel electrode and stack operating temperature. The results suggest that high efficiency, high hydrogen production, and long lifetime can be achieved in the lest scenario. Moreover, high stack operating temperature can improve hydrogen production and efficiency, allowing for operation at high steam concentration.

2.4 Integrated nuclear-hydrogen energy systems

An integrated energy system (IES) consists in an intricate framework designed to optimize the synthesis, conversion, distribution, storage, and consumption of energy sources across diverse sectors, providing several outputs besides electricity. These systems strategically amalgamate an array of energy sources, encompassing VRE alongside conventional sources such as hydro and nuclear power, as shown in Figure 2.8.

A core feature is the incorporation of Combined Heat and Power (CHP) systems, ensuring simultaneous electricity and heat production to maximize overall energy efficiency. Advanced energy storage technologies play a pivotal role in addressing temporal mismatches in energy supply and demand. For this reason, IESs use demand-response strategies for the energy management to increase overall flexibility and efficiency. The dynamic switching facility in Figure 2.8 represents the dynamic switching facility, which can be defined as the control station that regulates and monitors the performances of the subsystems, assuring that the entire IES satisfies the operational and safety requirements when switching from excess power generation to other forms of products or storage. In this sense, cost-effectiveness for the energy utilization represents a key factor for the design of the dynamic control [19].

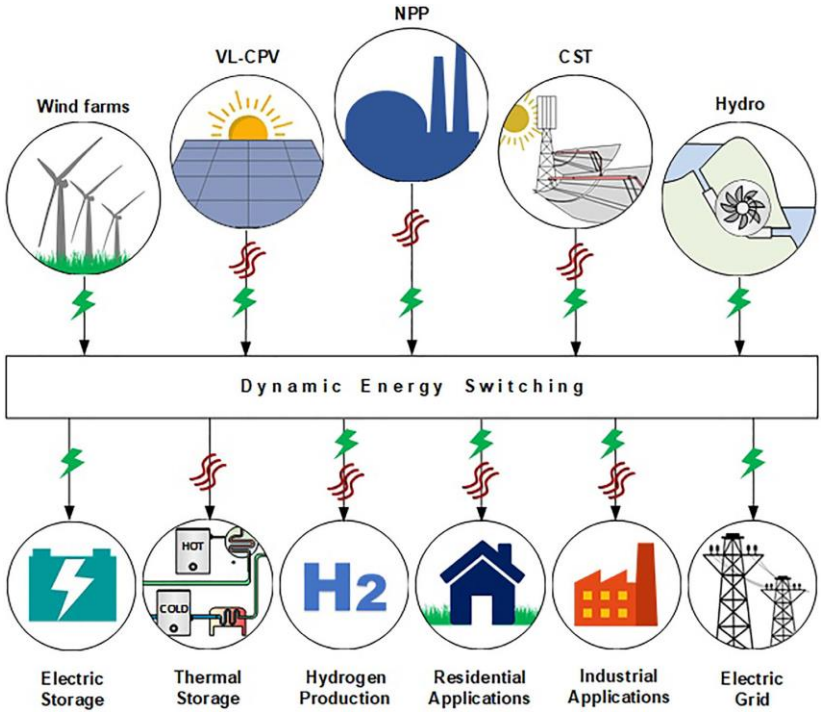

Figure 2.8 - Schematic representation of an integrated energy system [19]

The deployment of IESs for multigeneration allows a broad range of operations to maximize the overall system performance and profitability. There are several possibilities for multigeneration, with electric-only applications (electricity delivered to the grid or electric storage), thermal-only applications (thermal storage), and applications requiring both electricity and thermal power at the same time (hydrogen production, residential or industrial applications) [19].

As already hinted in Chapter 1, integrated nuclear-hydrogen systems represent a promising solution for sustainable hydrogen production, offering several advantages to address key challenges in the energy landscape. By leveraging NPPs, these systems can contribute to significantly reduce GHGs emissions, serving as a reliable, dispatchable and low-emitting source for hydrogen generation.

The inherent characteristics of nuclear power play a pivotal role in ensuring the reliability and continuity of hydrogen production, dampening the intermittency and the other issues associated with VRE. NPPs enhance energy security by offering a diversified and resource-abundant alternative to conventional fossil fuels. The high-temperature heat output of nuclear reactors proves particularly advantageous for the coupling with processes such as high-temperature electrolysis performed with SOECs, reducing the dependency on natural gas of the hydrogen production process, thereby addressing environmental concerns while optimizing the overall efficiency of the IES at the same time.

The decentralized deployment potential of SMNRs would allow localized hydrogen production, reducing the need of extensive storage and transportation infrastructure [41]. However, it is imperative to address challenges inherent to nuclear energy, including safety considerations on the proximity of non-electrical applications to the NPP [19].

2.4.1 Operational projects

The integration of NPPs and systems for hydrogen production is already being tested in various countries. As of October 2023, there are three operational projects [42], whose main characteristics are reported in Table 2.3. These projects rely on already-existing NPPs and use well-established technologies for hydrogen production through water electrolysis (section 2.2).

The fist to become operational was the one in Oskarshamn NPP (Sweden), which started producing hydrogen in 1992 through ALK for internal consumption within the NPP (hydrogen was added to the reactor coolant to reduce the risk of stress corrosion cracking of the reactor piping by reducing the amount of free oxygen in the coolant). However, two of the three units of the NPP closed in December 2016 and

June 2017, respectively, and the plant produced more hydrogen than needed. For this reason, Linde decided to first use the excess hydrogen "in the green transition of the Swedish industry, but also for the supply to its existing customer base", aiming to expand the current capacity of the plant (12 kg/h) [43].

The second project is the one built in the Kola NPP (Russia), operational since 2022 and becoming a pilot project in Russia. Like Oskarshamn, this system produces hydrogen to be used in the reactor coolant. However, this was the first project to use PEM and the size of the hydrogen production facility is expected to be increased to 10 MW_e in the next years [44].

Table 2.3 - Operational projects of integrated nuclear-hydrogen systems

Project name	Kola Nuclear Power Plant Demo	Oskarshamn nuclear plant	Constellation – Nine Mile Point Nuclear Plant
Country	Russia	Sweden	United States
Date online	2022	1992	2023
Nuclear technology	VVER (PWR)	BWR	BWR
Hydrogen technology	PEM	ALK	PEM
Hydrogen system size [MW_e]	1	0.7	1
Hydrogen system capacity [$Nm^3(H_2)/h$]	192	152	192
References	[44], [45]	[43]	[46]

The last project to become operative was in Constellation's Nine Mile Point NPP (NY, U.S.) in March 2023. This represents the first demonstration-scale project in the United States, expected to demonstrate the potential for hydrogen to power a clean economy. The system uses PEM manufactured by NEL Hydrogen to produce 560 kg/d of hydrogen and was awarded $5.8 million from the US Department of Energy (DOE). The plant already produces more than enough to satisfy the NPP internal consumption, and Constellation Energy expects the project to set the stage for possible large-scale deployments at other clean energy centres in its fleet that would couple clean hydrogen production with storage and other on-site uses [46].

Moving to hydrogen production by means of SOEC, there are four operational projects as of October 2023, but none of them involves NPPs [42]. All the projects are in Europe, and their main characteristics are reported in Table 2.4.

.

Table 2.4 - Operational projects for hydrogen production with SOECs

Project name	GrInHy2.0	REFLEX	MultiPHLY	HotFlex
Country	Germany	Italy	Netherlands	Austria
Date online	2020	2018	2023	2020
Electricity source	Grid	Solar PV + hydro	Dedicated renewable	Grid + renewables
Hydrogen system size [MWe]	0.7	0.038	2.5	0.15
Hydrogen system capacity [$Nm^3(H_2)/h$]	200	10	658	39
References	[47]	[48]	[49]	[50]

The first project to become operative was REFLEX (Italy) in 2018. Here, the SOE system is coupled to local solar PV and a mini-hydro to run a SOE system in an in-field demonstration in a technological park, moving the technology readiness level from 3 to 6 [48].

The Hotflex project (Austria) became operational in 2020 and uses renewables and the grid power from Mellach power station to run a hydrogen production system.

Project GrInHy2.0 (Germany) is operational since 2020 and represents the first implementation of a Megawatt-class high-temperature electrolysis system. It consists of eight modules with 720 or 1080 cells each, that is 24 or 36 stacks, respectively. The system produces 200 Nm^3/d of hydrogen running on waste heat of steel production and electric power from the grid.

Lastly, the MultiPHLY project (Netherlands) became operational in 2023 and is the world's largest installation of SOECs. The SOE plant, installed by Sunfire, is integrated in Neste's refinery process, and produces more than 60 kg/h of hydrogen using industrial waste heat as heat supply.

Including demonstrations in the count of active projects, two more can be added to the list, and they both rely on heat and electricity from NPP [42]. Table 2.5 reports their main characteristics.

The first project is the Solid Oxide Electrolysis System Demonstration (US) by FuelCell Energy, with partnerships from the Idaho National Laboratory and Versa

Power Systems. The aim is to validate that integration of solid oxide steam electrolysis with nuclear plants will provide a high-efficiency and low-cost alternative for production of hydrogen utilizing electricity and waste heat. The project uses a 250 kW_e module with 16 stacks able to produce 150 kg/d of hydrogen, while the integration with a NPP is simulated using a steam boiler which provides heat to the system. During the system operation, INL's Controller Hardware-in-the-Loop (CHiL) will simulate dynamic behaviour of a NPP, and stacks durability will be verified under dynamic operation. FCE's SOEC system is a potential candidate for a Department of State project announced at the COP27 Climate Conference related to cooperation between Ukraine and the USA to demonstrate production of hydrogen and ammonia using SMNR technology and innovative electrolysis technologies in Ukraine [51].

Table 2.5 - Demonstrations of integrated NPP-SOEC systems

Project name	Solid Oxide Electrolysis System Demonstration	Xcel's Energy Minnesota nuclear plant
Country	United States	United States
Date online	2020	2024
Nuclear technology	LWR (simulated)	PWR
Hydrogen technology	SOEC	SOEC
Hydrogen system size [MWe]	0.25	0.24
Hydrogen system capacity [$Nm^3(H_2)/h$]	66	632
References	[51]	[52]

The second project is Xcel's Energy Minnesota nuclear plant (US), and it should become operative in 2024. For this project, Bloom Energy announced its plans to install a 240 kW_e electrolyzer at Xcel Energy's Prairie Island Nuclear Generating Plant in Welch (Minnesota), a NPP that uses 2 PWRs. According to Bloom Energy, pairing solid oxide electrolysis with nuclear energy's technology is a preferred method of unlocking unmatched efficiencies, producing hydrogen more efficiently than low temperature electrolysis alternatives like polymer electrolyte membrane (PEM) or alkaline. These low temperature alternatives require roughly 40% more electricity, providing the Bloom Electrolyzer an efficiency advantage that is expected to significantly drive down the cost of hydrogen production [52].

2.4.2 State of the art of integrated SMNR-SOEC energy systems

As emerges from section 2.4.1, there are no operational projects of integrated nuclear-SOEC systems. Even more so, there are no operational projects for IES using SMNR, given the small number of currently operating SMNRs (section 2.1.3). However, this type of IES is subject to great interest in the scientific world and is being deeply investigated, even if research is currently limited to modelling and simulation.

The first aspect to analyse is the techno-economic feasibility of an integrated SMNR-SOEC system. A work from N. Chalkiadakis et al. [53] focuses on the simulation of a IES on the island of Crete, Greece. This work uses Crete's electricity demand values to propose three scenarios: in the first, a SMNR is sized according to the electricity demand on the island (350 MW_e, capacity factor 90%); in the second scenario a solar PV plant is sized in the same way and is added alongside the SMNR in the energy system; the third scenario adds an electrolysis system that produces 10 t/d. The results suggest that SMNR alone can provide electricity to the island 74% of time, sensibly reducing emissions, selling the excess electricity when produced and buying electricity from the grid when unable to match the demand. Adding the PV plant and the hydrogen system helps to further reduce GHGs emissions and provide a viable way to increase VRE penetration and promote hydrogen consumption.

Similar results were achieved in a paper from A. Ho et al. [54], which simulated a full operational year of an integrated system including a SMNR, a gas turbine and a large-scale hydrogen production system (using PEM) and a salt caver storage. The SMNR alone met the energy demand for 73.4% of the year, but the addition of the hydrogen production and storage system caused an increase of almost 20% in energy supply. This allowed the SMNR to run at base load 92.6% of the time and reduced the number of ramping cycles by 92.7%.

The technical feasibility of a SOE system coupled to a SMNR has been investigated in a work from J. S. Kim et al. [55], where a dynamic simulation was carried out to address the ramping time of a SOE system powered by an NPP. The proposed IES uses VREs (wind and PV) coupled with a SMNR (a 300 MW_e PWR) for electricity generation, while the hydrogen system is based on planar SOECs. The considered SMNR provides thermal energy at a temperature of 318°C, while SOECs operate at 850°C: for this reason, electric heaters have been adopted to boost the temperature in the hydrogen system. Three cases were studied, investigating the IES responses to a step change in VRE power input, and to load-following responses with PV and wind power. The system proved its flexibility with short response time and quick adaptability to new operating conditions, always respecting operative constraints and safety limits.

The introduction of hydrogen in IESs also has beneficial effects on the revenues generated by the system, as pointed out in a work from S. Pandey et al. [56]. Here, an IES with a SMNR and VREs was coupled with SOECs to produce hydrogen when electricity price is low, so to sell electricity when the price increased (using solid oxide fuel cells, SOFC). The SOE system could rely on the thermal power of the SMNR (considered constant at 600 MW_{th}), while deep reinforcement learning (DRL) was used to optimize the revenues from electricity according to the market price. The addition of hydrogen to the IES increased revenues by 27%, generating additional $48 million in a 120 days' time.

As already mentioned in section 2.4, costs linked to hydrogen storage and transportation can be reduce by leveraging the decentralized production enabled using SMNRs. A work from J. M. Lee et al [57] introduces the costs related to CO_2 to the overall evaluation, providing a deeper understanding of the advantage represented by SMNRs for hydrogen production. The proposed system uses a 300 MW_e VHTR, providing thermal energy at temperatures in the 900-1000°C range, while the capacity of the SOE system is fixed at 300 MW_e with a constant production of 8392 kg/h. The work also includes a sensitivity analysis according to plant capacity, grid electricity cost and carbon emissions costs. The results suggest that when the SOE system receives thermal power and electricity only by the VHTR, CO_2 emissions are the 27% of those if heat was provided by natural gas, while the cost is 60% of that resulting from the use of renewables. Even if large-scale NPP still results in the lowest hydrogen prices due to current technological advancements and deployment of SMNR, the technical limitations due to their large size suggest that SMNRs represent a viable alternative for decentralized hydrogen production.

3. Nuclear power plant

3.1 Integrated system overview

The proposed integrated system consists of a NPP powered by a SMNR, and a hydrogen production system working with SOECs. As a first approximation, the integrated system can be pictured as two separate systems interacting only by means a of heat exchanger, whose purpose is to supply the hydrogen system with the heat produced in the NPP. Figure 3.1 provides a generic view of the concept.

In the upper part of the figure, within the purple dashed line, is the layout for a generic NPP powered by a SMNR. We can think of the NPP system as composed by two subsystems: the SMNR itself and a power block. The SMNR provides thermal energy to the power block by means of a steam generator (SG). The core coolant removes the heat generated in the core due to fission reactions and flows at the hot side of the SG, where it gives off heat to the cold side and restarts the loop. The cold side inlet is subcooled feedwater, which undergoes evaporation in the SG, so that the cold outlet is superheated steam. The power block converts the thermal energy of the working fluid into electricity by means of a superheated steam Rankine cycle and an electric generator. A fraction of this electricity is used for internal consumption in the NPP (electric machines, control systems, backup and safety systems, utilities and more), while the rest of it can be delivered to the electrical grid.

In the integrated system, part of the SG outlet steam is drawn upstream the power block and diverted towards a heat exchanger, where it provides thermal energy to the hydrogen system, schematized within the green dashed line at the bottom of Figure 3.1. In this heat exchanger, part of the heat from the bled steam is used to evaporate the water which fuels the high-temperature steam electrolysis, while the remaining is sent back to the SMNR system. This heat exchanger is the only interface between the two systems and its operation is discussed in detail in chapter 4.

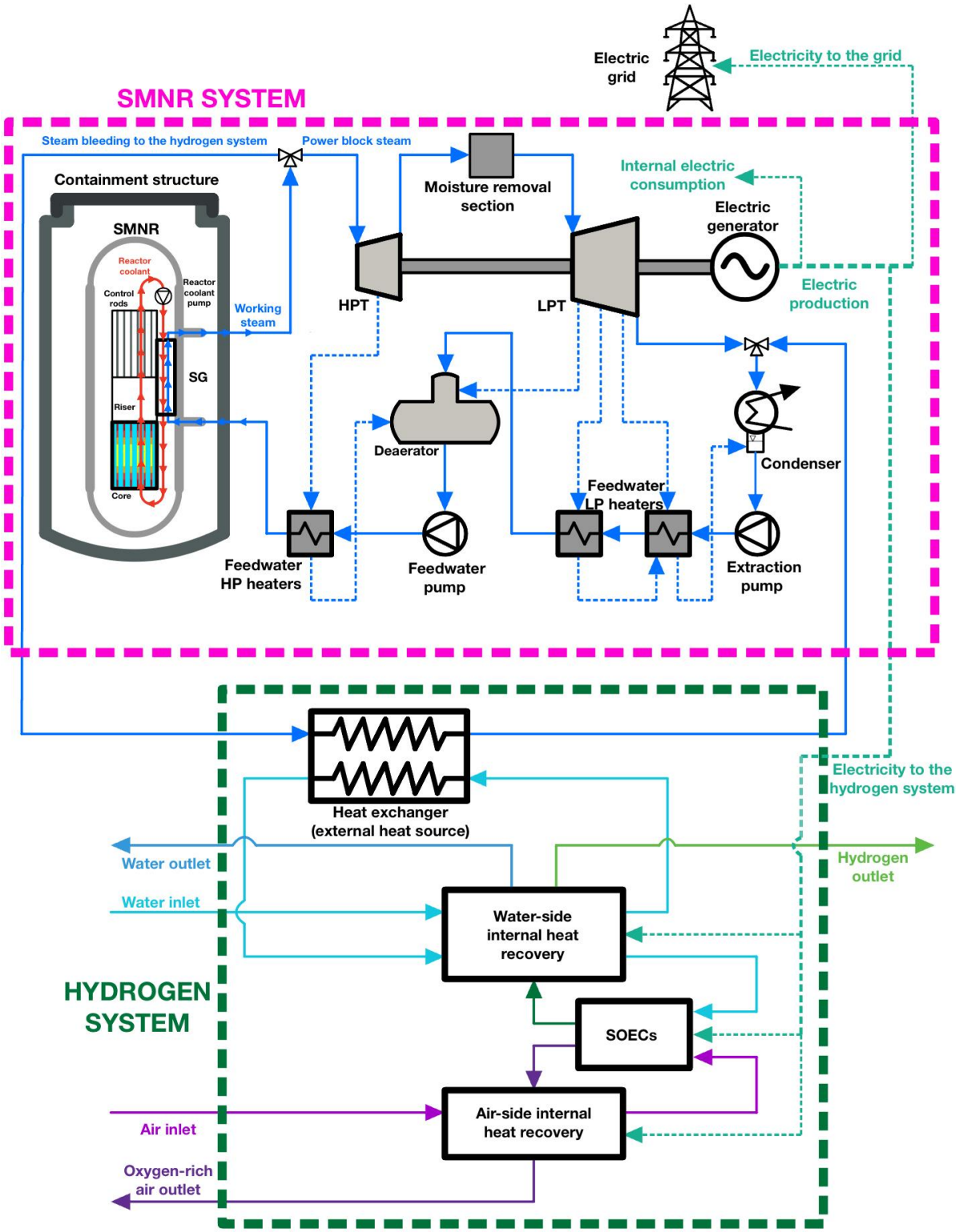

Figure 3.1 - Integrated system overview

The hydrogen system also needs electricity to perform electrolysis and operate its electric machines. Hence, a fraction of electric power available from the SMNR system is absorbed by the hydrogen system, while the remaining part is delivered to the electrical grid for transmission and distribution.

In the considered integrated system, the SMNR always operates at design conditions and the reduction in electricity production is due to the variation of the operating conditions of the power block alone. Indeed, as the bled steam mass flow rate increases, the thermal energy entering the power block decreases and, consequently, its electricity production. Thus, the integration of the two systems requires the knowledge of the power block behaviour in such peculiar conditions.

3.2 SMNR modelling

Given the novelty represented by this technology and the unexampled operation of the SMNR system, scientific literature is still lacking studies on the matter. Hence, it was necessary to model a SMNR power block and to simulate its functioning in the above-mentioned conditions to find the mathematical law that describes how the power production changes as the share of bled steam varies.

Modelling and simulation were performed on THERMOFLEX® by Thermoflow, a general-purpose heat balance software that allows to design a thermal system network and simulate its design and off-design operation. This software allows to model any type of power plant, including steam cycles, combined cycles, repowering, and a wide range of renewable energy plants and systems [58].

SMNRs are a recent technology, and as of mid-2023 only a very few of them is already operative, with the vast majority being under construction, in advanced or early development phases. Thus, scientific literature still does not provide any detailed description of the power block associated to a NPP powered by a SMNR, preventing to model a faithful replica of an existing power block. However, this is beyond the scope of this work, as the intention is to analyse the behaviour of the integrated system integrating a SOE system and a generic SMNR system.

The SMNR model of choice is the International Reactor Innovative and Secure (IRIS)[59], a PWR with a modular, integral primary system configuration. The IRIS development started in late 1999, led by Westinghouse Electric Company, initially under the U.S. Department of Energy (DOE) Nuclear Energy Research Initiative (NERI). IRIS garnered international interest and several international partners and research institutions (among which Politecnico di Milano) joined the project. As of today, IRIS is still not a commercial technology since the development and

deployment process of new nuclear reactor designs is a long and highly regulated process. Table 3.1 contains the main design parameters for a single IRIS module.

Table 3.1 - IRIS main design parameters

Section	Design parameter	Value	Value reference
Steam generator	Hot-side mass flow rate (core coolant)	4700 kg/s	[18], [59]
	Hot-side inlet pressure (reactor operating pressure)	155 bar	[18], [59]
	Hot-side inlet temperature (core outlet/riser temperature)	328.4-330°C	[18], [59]
	Hot-side outlet temperature (core inlet)	292°C	[18], [59]
	Hot-side (core) thermal power	1000-1005 MW_{th}	[18], [59]–[61]
	Cold-side inlet conditions	223.9-224°C 64 bar	[18], [59]–[61]
	Cold-side outlet conditions	317°C 58 bar	[18], [59]–[61]
	Cold-side mass flow rate (steam)	502-502.8-503 kg/s	[18], [60], [61]
Power	Net electric power	335 MW_e	[18], [59], [61]
	House load	33 MW_e	[61]
Condenser	Condenser pressure	0.0938 bar	[60]
	Condensate temperature	38-44.6°C	[60], [61]
	Condensate flow rate	384 kg/s	[60]
	Mass fraction to condenser	~51%	[61]
Turbine	Low-pressure turbine inlet conditions	257-259°C 10.34 bar	[60], [61]
	Mass fraction bled before high-pressure turbine (turbopump, reheating, ejections)	~9%	[61]
	Mass fraction available to low-pressure turbine	~65%	[61]

3.3 Power block design

The design and modelling only focused on the power block associated to the SMNR, whose layout is shown in Figure 3.2. Table 3.2, instead, shows the design parameters and the assumptions adopted in the process in accordance with data in Table 3.1. It should be mentioned that the principles that have been followed during the design process were to interfere as few as possible with the basic layout of the power block, and to maintain a safe approach in the SMNR side.

Table 3.2 - Values of the design parameters adopted for the power block sizing process

Section	Design Parameter	Value
Steam generator	Hot-side mass flow rate	4700 kg/s
	Hot-side inlet pressure	155 bar
	Hot-side inlet temperature	292°C
	Hot-side outlet temperature	330°C
	Cold-side inlet conditions	224°C 64 bar
	Cold-side outlet conditions	317°C 58 bar
Condenser	Hot-side outlet temperature	42.6°C
Turbines	LPT inlet conditions	272°C 10.3421 bar

On the left-hand side of Figure 3.2 is the steam generator (SG), which has been modelled as a generic heat exchanger (component 1) with core coolant flowing into the hot side and feedwater-steam flowing into the cold side. The core coolant inlet and outlet conditions are guaranteed by a heat source and a heat sink, respectively, with fixed temperature, pressure, and mass flow rate. This way, the steady working condition of the core is correctly represented and modelled through a constant thermal power at the hot side of the SG. For what concerns the cold side, outlet temperature and pressure are set to be constant, while the inlet pressure value is achieved thanks to an electric pump (component 16), and a turbopump (component 14) that expands steam bled downstream the reheating section (stream 27-62). An electric heater (component 41) has been added between the last feedwater heater and the SG inlet to keep feedwater temperature to the design value and maintain a constant temperature at the SG cold inlet. This measure was adopted in accordance

with the safety principle, as the core is extremely sensitive to the variation of the coolant thermodynamic conditions. A more accurate analysis on this design feature will be provided in section 3.4. Since the hot side of the SG has a fixed thermal power, and the cold side has constant inlet and outlet conditions, the mass flow rate flowing at the cold side could not be specified as the SG design would become over-constrained. So, the software provides a value of 521.4 kg/s, around 3.7% higher than the values reported in Table 3.1: the reason for this might lie in a different thermodynamic performance of the heat exchanger in the model with respect to the SG used in the datasheet. Anyway, the accuracy is widely acceptable given the high number of degrees of freedom in the modelling.

The SG cold-side outlet is sent through a first valve (component 17) which allows the steam bleeding for the hydrogen system operation, represented by stream 55 on the left of Figure 3.2. The design phase of the power block has been carried out for null mass flow rate flowing in this branch, representing the operative condition for which the hydrogen plant is in hot standby mode and the NPP is operating at nominal power. In real operating conditions, hot standby mode would still require a certain mass flow rate to provide heat. However, as a first approximation, this mass flow rate has been neglected and the hydrogen system is assumed to run in hot standby mode without any heat or electricity from the NPP.

When the hydrogen system is operative, the bled steam goes through a lamination valve (component 37) that decreases pressure to 5 bar so to reduce the pressure difference between hot and cold side of the NPP-SOE heat exchanger (the cold side is around ambient pressure), causing the steam temperature to drop about 57°C in the process. The NPP-SOEC heat exchanger (component 38) acts like an evaporator, but more on this will be discussed in chapter 4.

For what concerns the hot side of the heat exchanger, the mass flow rate is variable in accordance with the integrated system regulation, while the inlet and outlet values of temperature and pressure are fixed. More specifically, inlet conditions only depend on the reactor operation, while outlet conditions are determined by the control logic at the hydrogen system side: to avoid condensation of the hot stream in the tubes of the heat exchanger, the hot outlet is always saturated steam for any operative condition. This means that the hot-side outlet temperature is around 152°C, making the flow (stream 57) still suitable for further heat recovery before being sent back to the condenser. Applications could span from heat recovery in the preheating line to sanitary hot water or low-pressure steam production. However, as the goal of the simulation is just to provide a power curve for off-design operation, the heat recovery process has not been directly modelled to reduce the impact on the base power block layout.

Since saturated steam at relatively high temperature and pressure is sent directly to the condenser, heat rejection in the model will be higher with respect to the original system. Since the condenser is sized at the design condition (when the mass flow rate of streams 55-57 is null), it will result undersized when the hydrogen system is operative, and both its hot and cold-side outlet temperatures will increase. Cold side outlet temperature is strictly regulated in real life as it could be harmful to habitats and wildlife. The model does not consider these restrictions for their implications are beyond the scope of this work: an actual design of the plant would have to consider the temperature decrease of stream 57 due to heat recovery and size the condenser so to be compliant with regulations.

The other branch of the valve immediately downstream the SG (component 17) drives the steam to the NPP power block (stream 4). Before the steam enters the high-pressure group of the turbine (HPT), a second valve (component 7) allows to bleed part of the steam (stream 6) to provide thermal power to the re-superheating section downstream the HPT as it is common in steam cycles of similar plants [60]. The main flow (stream 5) goes through the HPT and then, since the vapor title at the outlet is lower than 1, the steam goes through the moisture separator reheaters (MSRs), where it is reheated (components 5 and 6) after the condensate removal (component 4). This step is required so that the vapor title at the inlet of the low-pressure group (LPT) is not too low and the turbine is not penalized or damaged by the excessive presence of liquid in its final stages. The hot-side outlet streams of the two heat exchangers in this section are sent to the two high-pressure feedwater preheaters, as they still have some thermal power to be exploited.

The pressure value at the inlet of the LPT (inlet of component 19) was set as a design parameter (Table 3.2). The software determined the HPT outlet pressure (outlet of component 2) by adding the pressure drops across the re-superheating section to the LPT inlet pressure. In a similar way, the LPT outlet pressure was determined by the software given the design parameters set for the condenser (component 32).

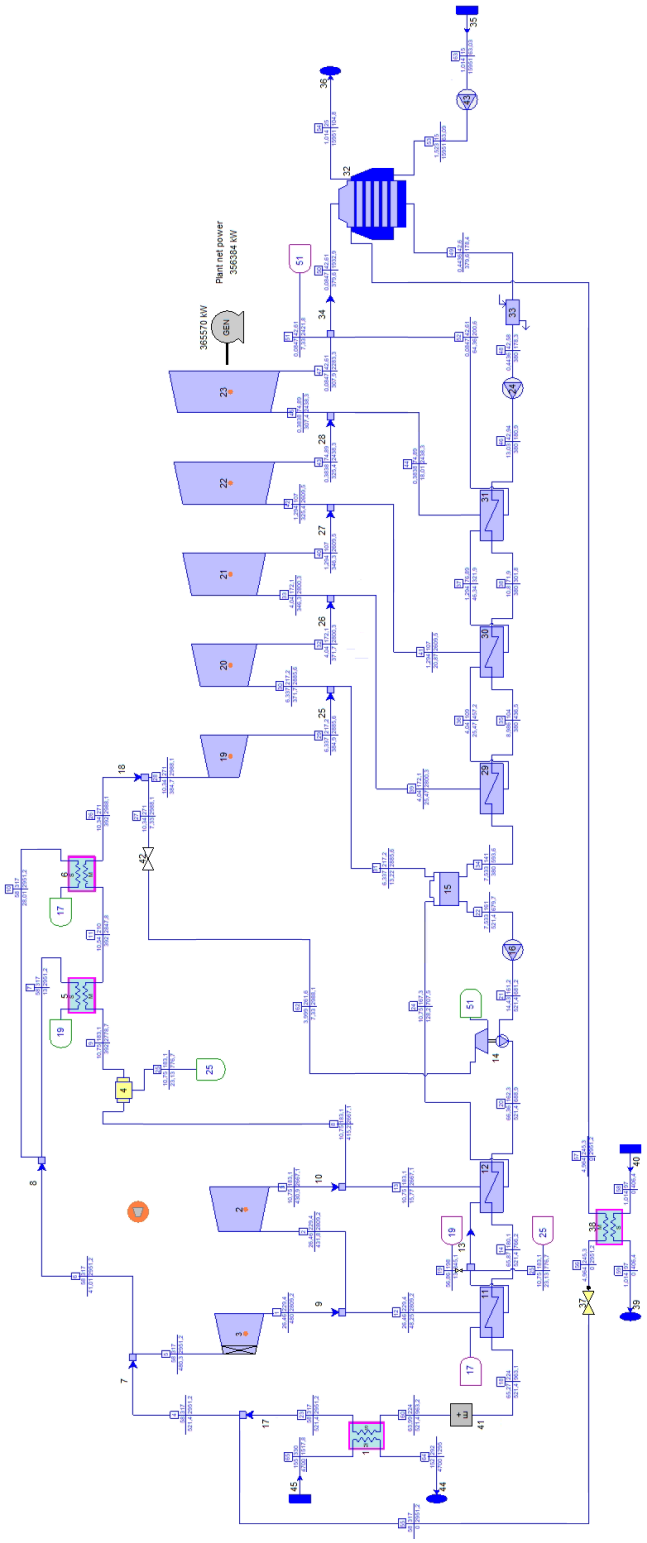

Figure 3.2 - NPP power block layout

An extraction pump (component 24) placed downstream the condenser pushes the water through the preheating line, which consists of three low-pressure feedwater heaters (components 29, 30, and 31), a deaerator (component 15), and two high-pressure feedwater heaters (components 11 and 12), all fed by steam bleedings from the turbine. The feedwater outlet temperature for each preheater was set equal to values found in literature [60]. As already mentioned, between the deaerator and the two high-pressure preheaters, the feedwater goes through an electric pump and a turbopump which increase the pressure enough to win the pressure drops in the components downstream and meet the specification for the SG cold-side inlet. The steam expanded by the turbopump (stream 51) is sent back to the condenser.

All the values of pressure drop across the components in the power block are assumed as the default ones on THERMOFLEX® and no further investigation was carried out.

Once the power block layout is determined and all the design parameters are set to the desired values, THERMOFLEX® proceeds to perform the thermodynamic and engineering designs. In these two steps, the components of the power block are sized in compliance to the specified inputs.

3.4 Off-design operation

After the engineering design was concluded and all the components size was fixed, the next step was to simulate the behaviour of the power block as the mass flow rate bled towards the hydrogen system was gradually increased up to the point where power production is no longer possible.

The aim was to find the power produced by the NPP at different values of bled steam, check the correct operation of the plant, and interpolate the points so to achieve a mathematical equation describing how the produced power varies with the bled steam. It is important to remember that the mass flow rate of steam produced by the SG is constant for any operative condition, meaning that the sum of the mass flow rates bled towards the hydrogen system and circulating in the power block is always equal to 521.4 kg/s.

At the design conditions the steam bleeding towards the hydrogen system is null and the steam produced by the SG is entirely sent to the power block, whose components are all working at design conditions. In this operative condition, the software computes a net power output at the generator of 356.5 MW_e.

The off-design simulation was carried out increasing the bled steam mass flow rate by steps of 50 kg/s up to a value of 250 kg/s. It is important to remember that while

the steam circulating in the turbine and the MSRs decreased with every step, the water mass flow rate in the preheating line is constant for any operative condition, as the bled steam is reintroduced in the condenser. As expected, when the mass flow rate circulating in the turbine is reduced, the turbine responds by decreasing the internal and outlet pressures and temperatures. The occurrence of this phenomenon, together with an increasing disproportion between the two streams, results in a reduced cold-side inlet temperature to the SG. Since the reactor is kept at design conditions, the amount of heat exchanged at the steam generator is fixed, together with the cold side mass flow rate. This implies that, if no action is taken, the cold-side outlet temperature would also decrease more and more as the off-design condition is brought to its limit, possibly affecting even the reactor coolant thermodynamic conditions. As mentioned in section 3.3, given the core extreme sensitivity to variations of thermodynamic conditions in the SG, an electric heater was introduced between the last feedwater heater and the SG as a precautionary feature. The heater is intended to bring the feedwater temperature to the design value for any off-design condition. Since the electric power required by the heater is decurted from that made available by the plant, this might not be the optimal solution, and further investigations on the possible alternatives could lead to improvements of the technology.

The values of net electric power output and electric heater thermal duty were extracted for each of the considered values of bled mass flow rate. An efficiency of 95% was assumed for the electric heater, allowing to calculate its electric power consumption in the considered operative points. For convenience, the values of bled mass flow rate have been expressed as a percentage of the SG total outlet steam mass flow rate (521.4 kg/s) and will be referred to as "ε" in the following. The power curves shown in Figure 3.3 have been obtained using the built-in curve fitting tool on MATLAB on the six points extracted for each desired curve. For the sake of simplicity, from this point on, the net electric power of the NPP obtained in THERMOFLEX® will be referred to as "electric generator power". The cubic polynomial obtained from the data fitting process returned an electric generator power of 356.5 MW_e when NPP works at design conditions.

To find the electric power available at the grid terminals, the electric generator power needed to be decurted of the house load and of the heater electric power. For convenience, it was assumed a constant house load of 20 MW_e, so to have a net electric power at design conditions of 336.5 MW_e, only 1.5 MW_e higher than the value indicated in Table 3.1. Since the house load was assumed to be constant over the whole operative range, the gross power curve is achieved by shifting downwards by 20 MW_e the electric generator power curve. As a final step, the heater electric power

consumption was subtracted from the gross power, and the curve representing the power available from the NPP was achieved.

Once this last curve was found, it was possible to calculate the value of ε at which the available power from the NPP drops to zero. Figure 3.3 shows the curves obtained from the modelling process: the light blue curve is the gross power, the curve in red is the heater electric power consumption and the green curve represents the power available from the NPP. According to this model, available power drops to zero when 39.7% of the steam is bled upstream the power block. This value may vary with different plant layouts or control logics, which could be a worth subject for further investigation.

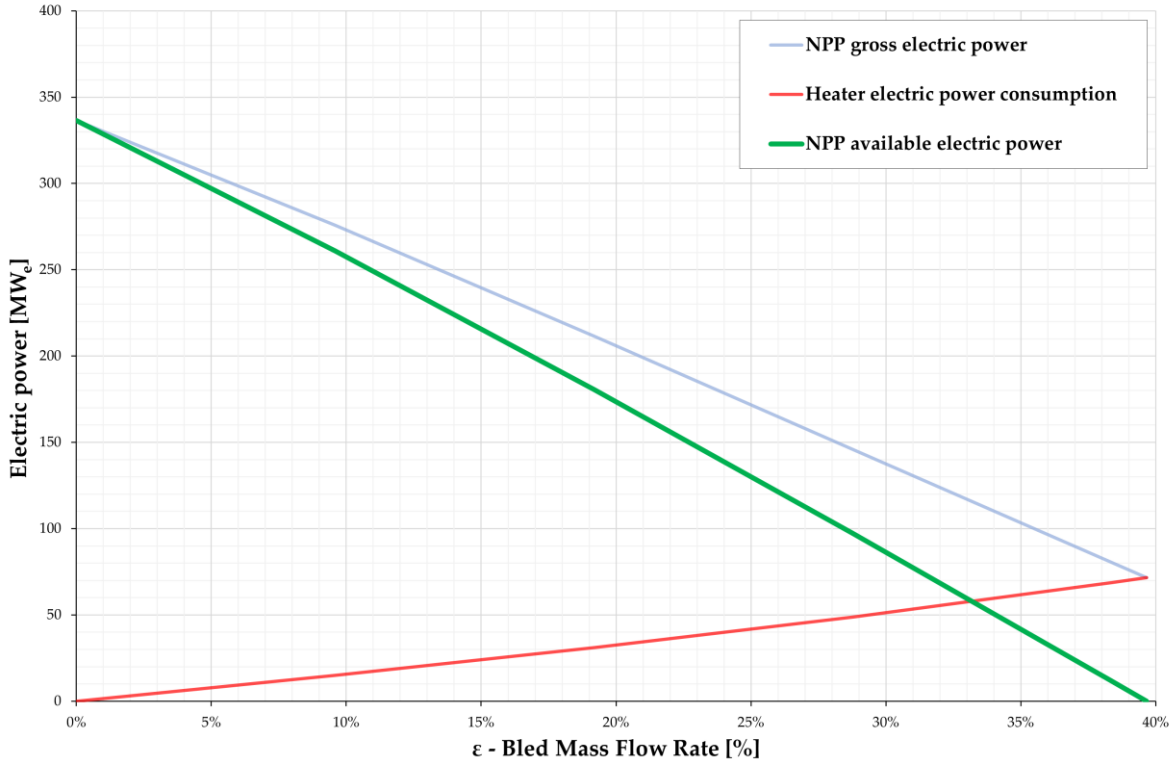

Figure 3.3 - NPP available electric power curve

The third-grade polynomial describing the NPP available power has been used as a base for the SOEC plant model, which will be discussed in chapter 4. The curve will provide the values of power available to the hydrogen plant and, consequently, the net power delivered to the grid (that is the difference between the available power and the hydrogen system electric consumption).

Figure 3.4 shows the trends of the power block first-law efficiencies (related to gross and available net power) as a function of ε over the thermal power entering the power block.

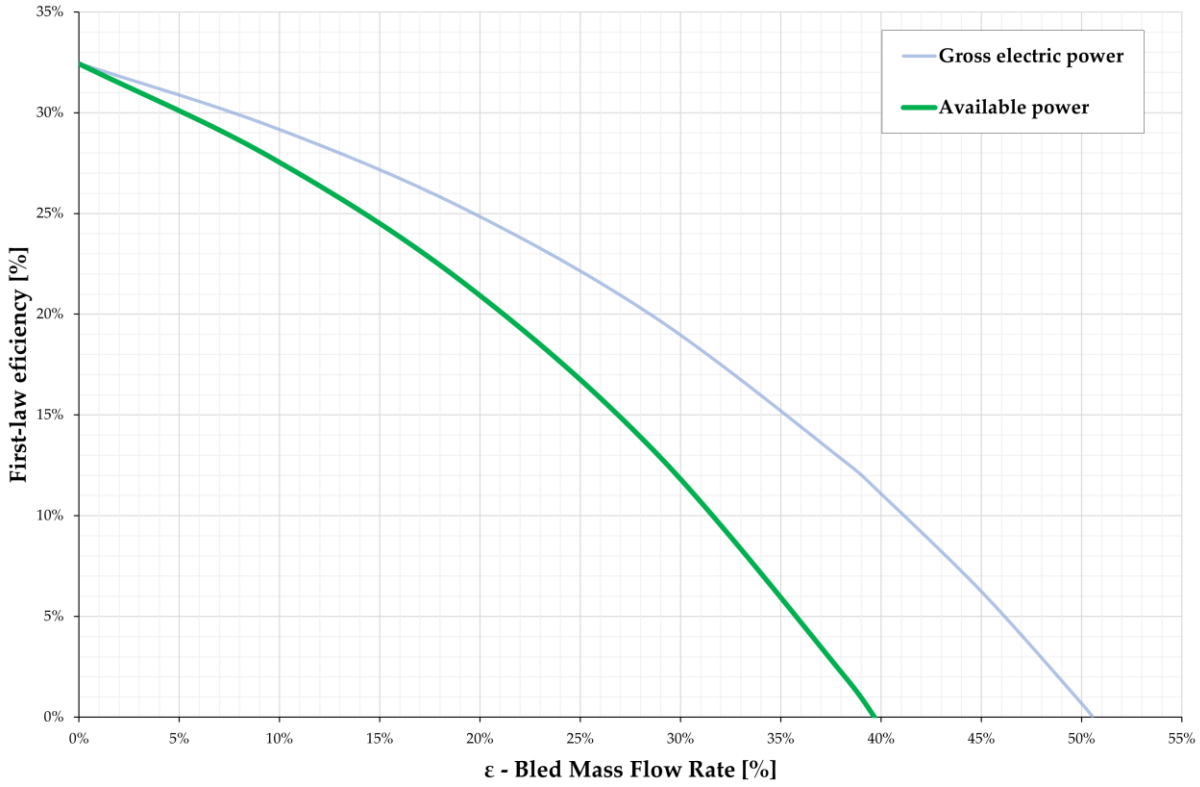

Figure 3.4 - Power block first-law efficiency as a function of ε

The thermal power entering the hydrogen system (Q_{SOE}, [MW_{th}]) can be calculated as:

$$\dot{Q}_{SOE} = \varepsilon \cdot \dot{m}_{SG-CS} \cdot (h_{SG-CS,out} - h_{COND-HS,out}) \quad (3.1)$$

Where the product of ε and the total steam mass flow rate at the SG cold side (m_{SG-CS}, [kg/s]) is the bled steam mass flow rate, while the specific enthalpy difference between the SG cold outlet and condenser outlet within the brackets expresses the available specific thermal energy of the bled steam ([MJ/kg]), as the hot outlet of the condenser is the point with the lowest specific enthalpy in the whole NPP. The difference between the thermal powers at SG cold side (constant) and QSOE (function of ε) returns the thermal power entering the power block as ε varies.

shows how rapidly the first-law efficiency related to available power drops as the value of ε is increased. Once again, the major role played by the electric heater is visible as the difference in the values of ε at which the green and the light-blue lines reach 0% efficiency, suggesting that improvement is likely possible.

Finally, the values of mass flow rate, temperature, pressure, and specific enthalpy in major points of the power block for four different operating conditions are provided. Figure 3.5 shows where the points are located on the power block layout. Table 3.3

refers to ε=0% (NPP works at design condition) and Table 3.6 refers to ε=25.337% (the design point for one of the configurations of hydrogen plant shown in chapter 4). Table 3.4 and Table 3.5 are for ε=9% and ε=16% respectively

The variation of temperature between the outlet of the last feedwater heater and electric heater inlet (point 9) for the different cases shows how the preheating line is less and less able to bring feedwater to design temperature as the value of ε increases, that is when the NPP off-design condition is pushed. The change in the temperature between the values in point 9 and 10 is operated by the electric heater. It is possible to see how the inlet and outlet conditions at the cold side of the SG (points 10 and 11) are kept constant as ε changes despite the variation in the mass flow rate entering the power block.

Mass flow rates at ε=0% show similar trends to those reported in Table 3.1, suggesting that the model is coherent with those found in literature and provides a satisfactory representation of a NPP power block design.

The effect of the undersized condenser is visible in temperatures for point 1, as they increase together with ε. However, changes are relatively small and the effect on the overall thermodynamic performances are negligible.

One last consideration can be made on point 16, as the temperature after the re-superheating section increases with ε. This effect is due to heat exchangers becoming oversized (mass flow rate is reduced) and hence their effectiveness increases, leading to higher temperatures at cold-side outlet. However, this is a minor effect and has no significant impact on the power block performances.

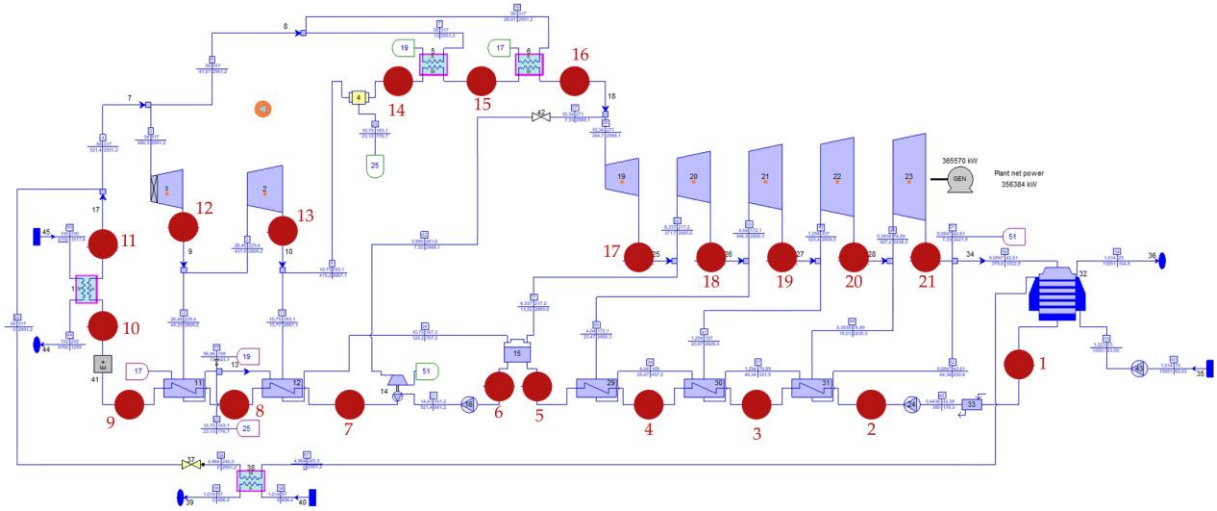

Figure 3.5 - Points on the NPP power block layout

Table 3.3 - Thermodynamic points for ε=0%

Point	T [°C]	p [bar]	h [kJ/kg]	ṁ [kg/s]
1	42.6	0.444	178.4	379.6
2	42.94	13.030	180.9	380
3	71.9	10.800	301.8	380
4	104	8.986	436.5	380
5	141	7.533	593.6	380
6	161	7.533	679.7	521.4
7	162.3	66.360	688.9	521.4
8	180.1	65.870	766.2	521.4
9	224	65.270	963.1	521.4
10	224	64.000	963.2	521.4
11	317	58.000	2951.2	521.4
12	229.4	26.460	2809.2	480
13	183.1	10.750	2667.1	430.9
14	183.1	10.750	2778.7	392
15	210	10.540	2847.8	392
16	271	10.340	2988.1	392
17	217.2	6.337	2885.6	384.9
18	172.1	4.040	2800.3	371.7
19	107	1.294	2609.5	346.3
20	74.89	0.384	2438.3	325.4
21	42.61	0.085	2283.3	307.9

Table 3.4 - Thermodynamic points for ε=9%

Point	T [°C]	p [bar]	h [kJ/kg]	ṁ [kg/s]
1	44.64	0.453	186.9	386.9
2	44.98	12.550	189.3	387.3
3	69.53	10.240	291.8	387.3
4	100.2	8.357	420.6	387.3
5	136.5	6.848	574.5	387.3
6	156.5	6.848	660.3	521.4
7	157.8	66.350	669.9	521.4
8	175.3	65.870	745.6	521.4
9	218.5	65.270	937.8	521.4
10	224	64.000	963.2	521.3
11	317	58.000	2951.2	521.4
12	223.9	23.820	2808	435.6
13	178.3	9.650	2665.6	388.3
14	178.3	9.650	2774.6	352.7
15	209.8	9.460	2853.2	352.7
16	271.9	9.727	2993.5	352.7
17	217.4	5.651	2889.3	345.5
18	171.8	3.582	2802.7	332
19	103.3	1.140	2610.8	306.8
20	72.26	0.343	2442	286.5
21	44.65	0.094	2310.2	271.4

Table 3.5 - Thermodynamic points for ε=16%

Point	T [°C]	p [bar]	h [kJ/kg]	ṁ [kg/s]
1	46.31	0.461	193.9	392.7
2	46.65	12.190	196.3	393.1
3	67.68	9.815	284	393.1
4	97.1	7.868	407.4	393.1
5	132.8	6.313	558.3	393.1
6	152.7	6.313	643.8	521.4
7	154	66.350	653.2	521.4
8	171.3	65.870	728.1	521.4
9	213.8	65.270	916.6	521.4
10	224	64.000	963.2	521.4
11	317	58.000	2951.2	521.4
12	219.4	21.770	2806.9	401.2
13	174.3	8.788	2664	355.3
14	174.3	8.788	2771	322.2
15	209.8	8.613	2857.7	322.2
16	272.6	8.440	2997.6	322.2
17	217.5	5.116	2891.8	314.8
18	171.4	3.226	2804.1	301.2
19	100.2	1.022	2611.9	276.2
20	70.15	0.314	2445.7	256.6
21	46.32	0.103	2342.6	243.5

Table 3.6 - Thermodynamic points for ε=25.34%

Point	T [°C]	p [bar]	h [kJ/kg]	ṁ [kg/s]
1	48.6	0.474	203.4	400.6
2	48.94	11.710	205.8	400.9
3	65.26	9.251	273.8	400.9
4	92.56	7.220	388.2	400.9
5	127.2	5.601	534.6	400.9
6	147.1	5.601	619.7	521.4
7	148.4	66.350	629.1	521.4
8	165.5	65.870	702.7	521.4
9	207.1	65.270	886.2	521.4
10	224	64.000	963.2	521.4
11	317	58.000	2951.2	521.4
12	212.9	19.050	2804.9	355.5
13	168.5	7.636	2661.4	311.5
14	168.5	7.636	2765.4	2801.6
15	209.9	7.483	2863.9	281.6
16	273.5	7.330	3003	281.6
17	217.5	4.404	2895.1	274.1
18	170.6	2.754	2805.6	260.2
19	95.72	0.868	2613	235.7
20	67.33	0.277	2452.3	217.2
21	48.6	0.115	2400.3	207

4. Hydrogen production system

The other part of the integrated system consists in a hydrogen production plant that relies on thermal power and electricity from the SMNR system to perform high-temperature steam electrolysis through SOECs. Like in the case of the NPP power block, the hydrogen system has been designed, modelled and its functioning has been simulated for several points at partial load conditions over the whole operative range (between hydrogen system nominal conditions to hydrogen plant shut off).

The model was developed on Aspen Plus®, a process simulation software by AspenTech commonly used in chemical engineering and related industries for modelling, simulating, and optimizing various chemical processes. The software allows to create detailed process models, perform mass and energy balances, and evaluate the performance for chemical, polymers, life sciences and new sustainability processes [62]. This part of the present work is based on an existing model [63], which has been improved and developed.

Figure 4.1 shows the concept behind the hydrogen system and a schematization of the material flows involved. The system is thought to be modular, so the whole hydrogen production plant is composed of several modules (N_{MOD}), whose number is to be determined in the system sizing phase. Each of the modules is provided with SOECs stacks for hydrogen production and pieces of equipment which will be better described in section 4.2. The figure provides a visual representation of the modularity concept linked to the hydrogen system. Indeed, the boundary of the system containing the different modules, each containing several stacks can be easily visualized.

The sizing phase can be imagined as a bottom-up process: the SOEC operating conditions are defined first, then the module components are sized according to the layout specifications and the number of modules is found, ultimately determining the size of the whole system.

A total of three plant layouts has been proposed, and their performances have been evaluated both in exothermic and endothermic SOECs operating conditions, leading to a total of six configurations analysed.

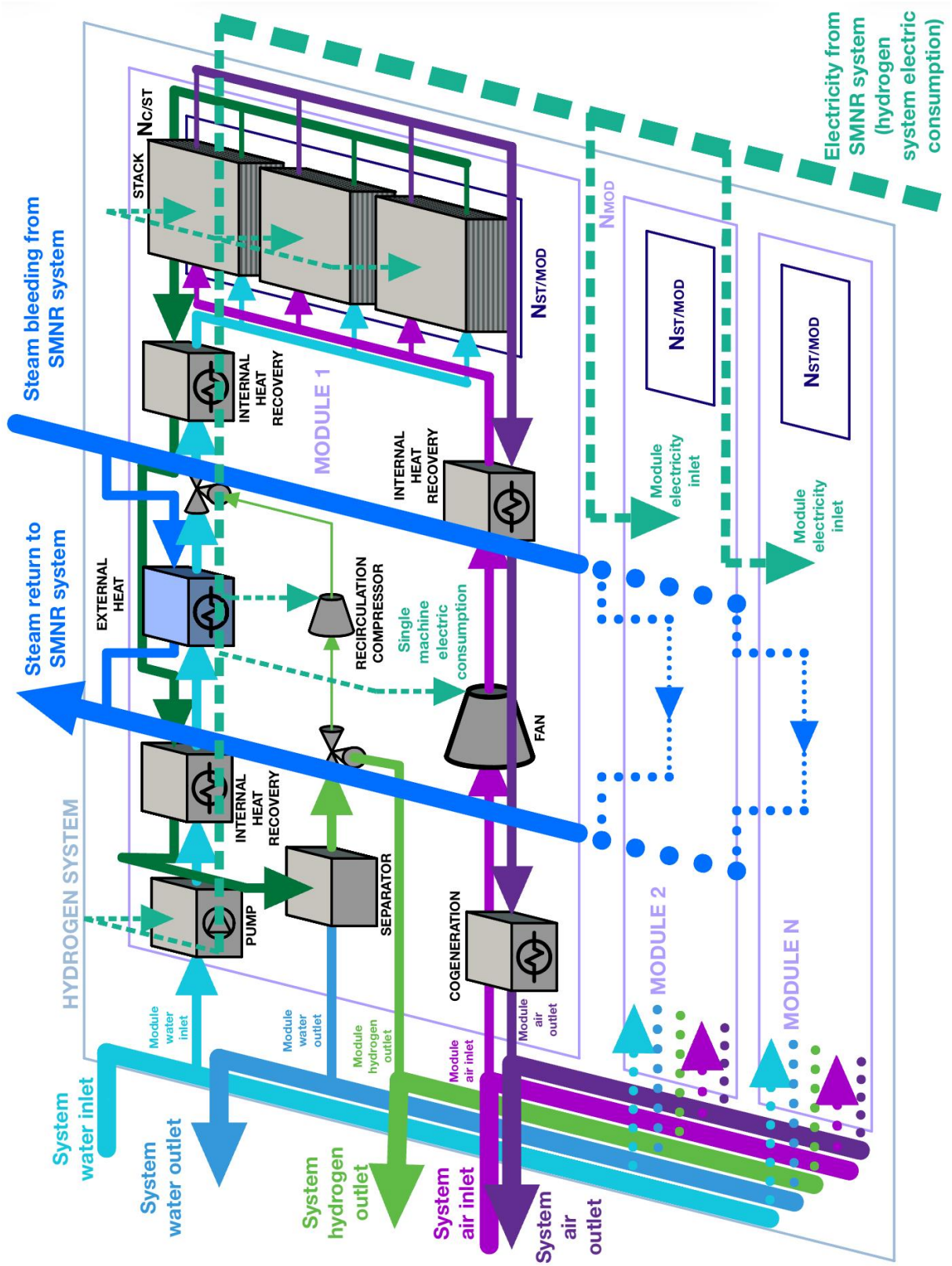

Figure 4.1 - Schematization of the hydrogen system

4.1 SOEC block design

The foundation of the whole design process is the definition of the SOECs design operating conditions and the sizing of the part of the system devoted to steam electrolysis.

The single cells are grouped in stacks composed of $N_{C/ST}$ cells. Each module consists of N_{ST} stacks, for a total of $N_{C/ST} \cdot N_{ST/MOD}$ cells per module. In the end, the whole hydrogen system will include $N_C = N_{C/ST} \cdot N_{ST/MOD} \cdot N_{MOD}$ cells in total. The number of cells per stack and the number of stacks per module are parameters of choice, while the number of modules is consequential to the system sizing phase and is not determined a priori. Coherently to what was explained in chapter 2, each module consisted in 50 stacks of 300 cells each, leading to a total of 15,000 cells per module.

Another parameter of choice is the molar composition of the SOECs cathode inlet flow. As explained in chapter 2, the "fuel" stream should include a variable share of hydrogen to maintain a reducing environment in the cells. A composition of 90% water and 10% hydrogen was adopted, achieving the hydrogen share by partial recirculation of the produced hydrogen.

Two more parameters to be chosen for the sizing process are the current density (j) and the utilization factor (UF). In accordance with typical operative values reported in chapter 2, current density was set to a design value of 800 mA/cm^2, while the utilization factor was set to 70%.

Details on the open circuit voltages and area-specific resistances will be provided in section 4.3 when dealing with the chosen polarization curves and the system operating conditions.

4.2 Hydrogen system layouts

In this section, three different layouts for the hydrogen system will be introduced. Each of the three layouts will differ from the others because of the routes of the streams within the system or the criteria according to which a component is sized. The three following subsections will provide a detailed description of the layouts.

4.2.1 Case A

Figure 4.2 shows the plant layout adopted for the reference model [63], renamed as case A. As for the other layouts shown in sections 4.2.2 and 4.2.3, the figure can be intended as a Matryoshka-like structure, with three different layers one inside another as visualized in Figure 4.1. The outer box delimited by the dashed light-blue

line can be intended as the boundary of the whole hydrogen system and all the modules are contained within. The intermediate box delimited by the dashed blue line identifies a single module, and N_{MOD} equivalent boxes can be imagined inside the outer one. Lastly, the inner box represents a single stack, and N_{ST}/N_{MOD} of these boxes can be imagined inside each single module.

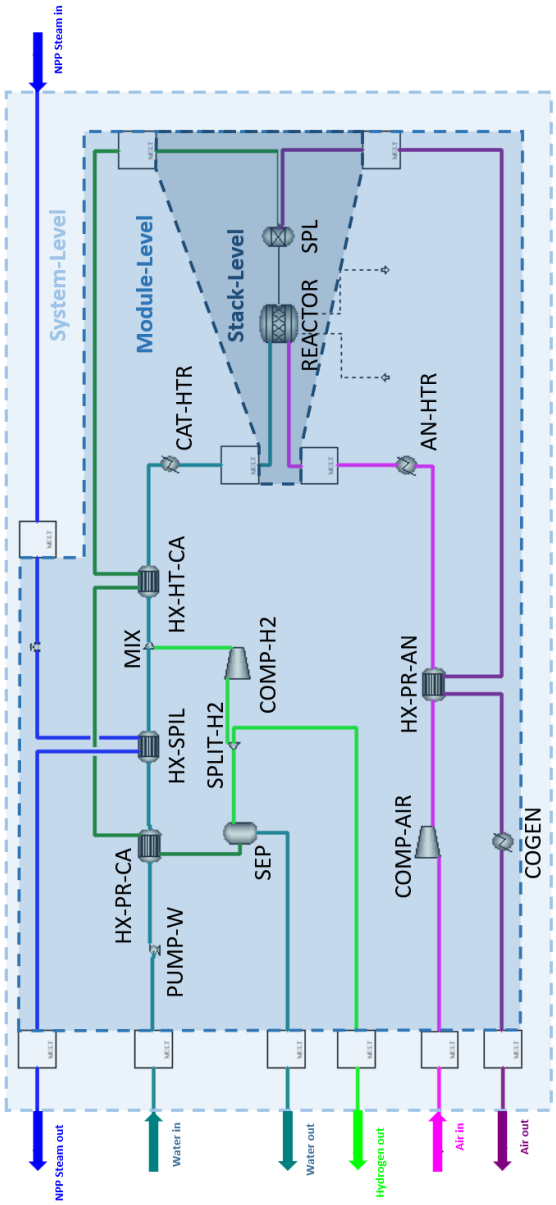

Figure 4.2 – Hydrogen system layout for case A

In this layout, cathode-side (fuel side) and anode-side (air side) inlet streams maintain two separate paths which never interact with each other.

Starting from cathode side, water enters the system at ambient conditions (at 20°C and 101,325 Pa) and is equally distributed among all the modules. In each module, the stream pressure is increased by a pump (PUMP-W) to win the pressure drops on the path, and then is sent through a heat exchanger (HX-PR-CA), where heat is recovered from the hot cathode outlet stream (dark green line). The cold-water stream is heated it up to 97°C, maintaining some degrees of subcooling to avoid evaporation in this section.

The subcooled water then flows through another heat exchanger (HX-SPIL), which is the only piece of equipment serving as an interface between the hydrogen system and the NPP. As explained in section 3.3, the hot-side fluid (blue line) is superheated steam bled downstream the SG and enters the system at 317°C and 58 bar. However, using steam at such high pressure would generate a large pressure difference between hot and cold side of HX-SPIL (cold-side is at around ambient pressure). Hence, before entering each heat exchanger, the hot-side steam is laminated to 5 bar and its temperature decreases to 260°C in the process. The hot stream is cooled down to saturated vapor conditions and leaves the hydrogen system. HX-SPIL works as an evaporator, and its cold outlet is superheated steam at 150°C: this value serves as a condition to make sure that evaporation of the cold stream is fully achieved. The cooling of the hot-side stream is limited to saturated vapor conditions to avoid a simultaneous double phase change at hot and cold side of HX-SPIL, which could represent a technological challenge.

The steam is then mixed with a hydrogen stream coming from the cathode outlet (green line) so to achieve the desired molar composition of the stream entering the stacks. This stream flows through the cold side of one last heat exchanger (HX-HT-CA) and is furtherly superheated. An electric heater (CAT-HTR) is placed after HX-HT-CA to provide the heat needed to bring the stream up to the operative temperature in case internal heat recovery and thermal from NPP should not suffice to achieve the desired stack inlet temperature.

This hot stream is equally split among the module stacks and flows through the cathode of the SOECs composing the stack. Since Aspen Plus® does not include any component to directly model this section, the single stack has been modelled as a cascade of a chemical reactor (REACTOR) and a separator (SPL), which simulate the process taking place inside the actual stack. Cathode and anode streams enter the reactor, where electrolysis is performed. Then, the outlet stream is sent to the separator, where cathode and anode streams are separated. It is important to highlight that modelling the stack this way, anode and cathode streams are mixed in the reactor. In real stacks, water and air streams are separated, and no streams crossover occurs.

The cathode outlet goes through the hot sides of HX-HT-CA and HX-PR-CA where it cools down (allowing for internal energy recovery), and then is sent to a separator (SEP). Here, the cathode exhaust is cooled down and hydrogen is separated from water, which exits the system at 40°C of temperature and slightly above ambient pressure. Hydrogen, instead, is sent to a splitter (SPLIT-H2) where a part of it is taken for recirculation, then sent through a compressor (COMP-H2) and a mixer (MIX). The remaining part (the vast majority) represents the module net hydrogen production, and the hydrogen produced from all the modules is collected at the system outlet (green line).

Moving to the cathode-side, the purple line represents the system inlet stream of air (oxygen 21%$_{mol}$, nitrogen 79%$_{mol}$) at ambient conditions. The air stream is equally split between the modules and sent through a fan (COMP-AIR) to win the pressure drops along its path and achieve a slight overpressure at system outlet. Then, air goes through the cold side of a heat exchanger (HX-PR-AN), where heat is recovered from the module's stacks anode outlet stream. Like for the cathode-side, an electric heater is added to path (AN-HTR). Air reaches the cells operative temperature and is split among the stacks and sent to the reactor/separator section, where it joins the cathode streams in the already-discussed process. As explained in chapter 2, the function of the air stream at the anode-side is to provide/remove heat to/from the cell in case of endothermic or exothermic operation, respectively. At the outlet of the stack, air has been enriched in oxygen (oxygen 27%$_{mol}$, nitrogen 73%$_{mol}$) by the oxygen ions resulting from the steam electrolysis process.

These oxygen-rich air streams from the stacks' outlets are mixed back to a single module-level stream, which is sent to the hot side of HX-PR-AN, where internal heat recovery is performed (dark purple line). Finally, it is sent to a cooler (COGEN) which simulates a further heat recovery process, where residual heat from the anode-side outlet stream can be exploited for collateral applications, such as sanitary hot water or low-pressure steam production. The actual heat recovery process has not been modelled as it is beyond the scope of this work. The only purpose of the cooler is to provide a general idea of the amount of heat that could still be recovered by cooling down the stream to 40°C, so to simulate a temperature difference of 15°C with a hypothetical water source at 25°C. After going through the cooler, the stream leaves the system at a pressure slightly higher than ambient.

4.2.2 Case B

This layout relies on the same components of configuration A, but the paths of anode and cathode outlet streams have been modified as shown in Figure 4.3.

In particular, the cathode-side outlet stream now only performs internal heat recovery in HX-HT-CA before being sent to the separator (SEP). The anode-side outlet stream, instead, performs internal heat recovery in AN-HTR and HX-PR-CA, where it performs water heating in the place of the cathode-side outlet stream (case A) before being sent to the heat recovery section in COGEN.

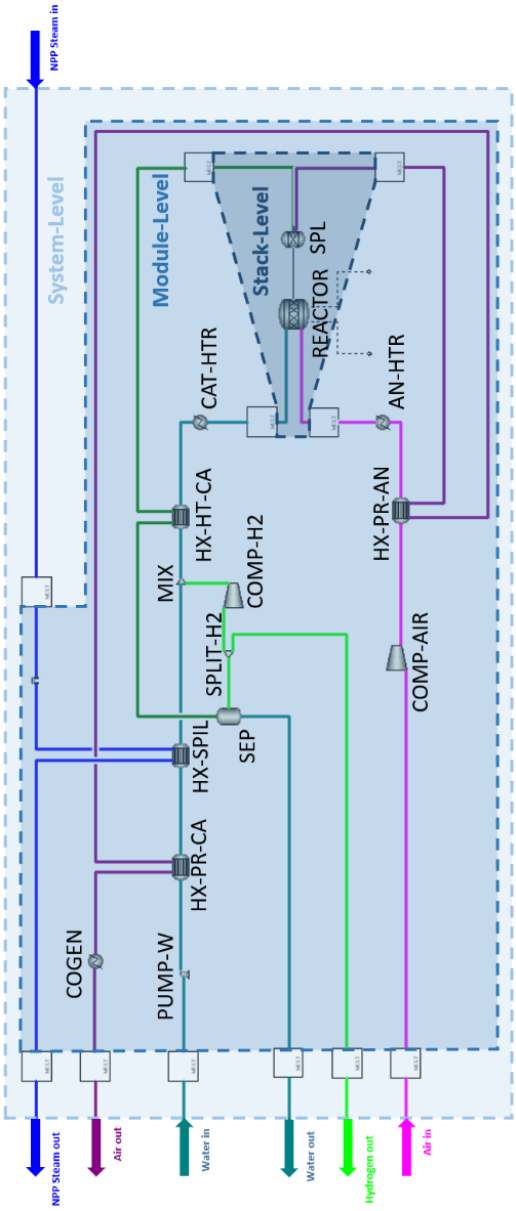

Figure 4.3 - Hydrogen system layout for case B

4.2.3 Case C

This last configuration is the same as configuration B, with the only difference represented by the position and dimensions of HX-SPIL. Here, contrarily to the other configurations, this heat exchanger is thought to be on a system-level, with only one large piece of equipment serving all the modules instead of them having their own. Figure 4.4 shows the layout in detail.

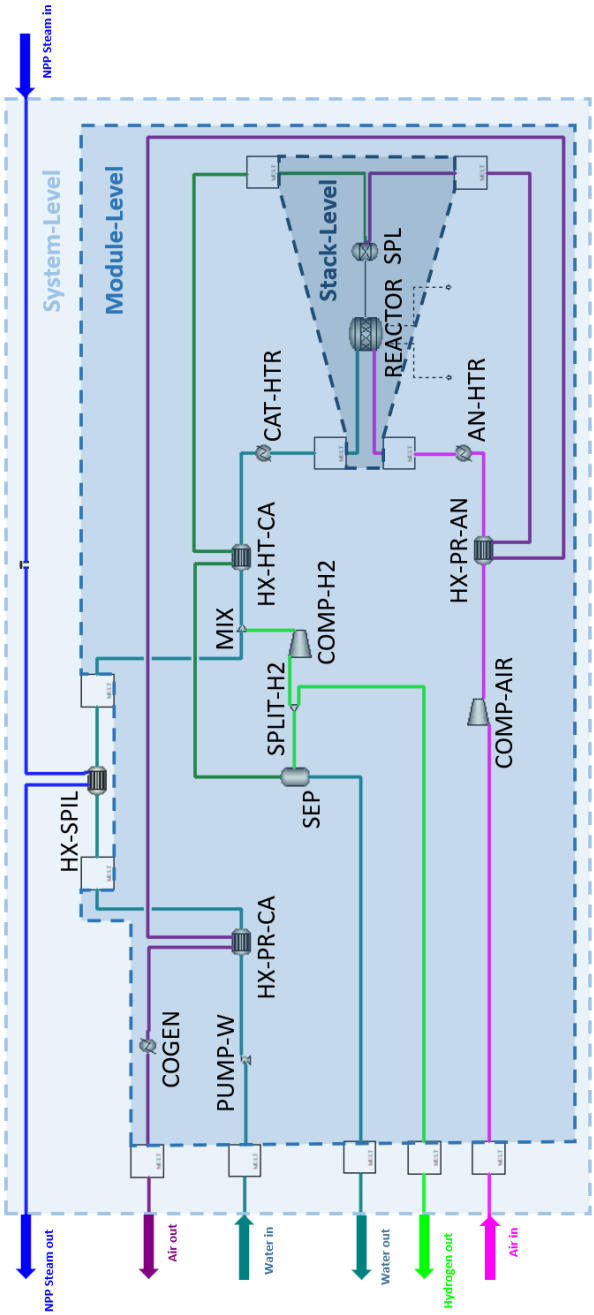

Figure 4.4 - Hydrogen system layout for case C

4.3 Exothermic and endothermic operation

As explained in chapter 2, SOECs can operate in exothermic or endothermic conditions with all the relative advantages and disadvantages. To fully evaluate the performances of the three hydrogen system layouts in section 4.2, each of them has been tested for these two operating conditions, bringing the total number of analysed configurations to 6.

Figure 2.6 in section 2.3.2 reported various polarization curves belonging to different types of cells. Among these, curves 1 and 4 (CSC with air at anode side) have been chosen to be included in the model and are shown in Figure 4.5. For simplicity, from this point on, the two curves will be referred to as case 1 (blue line) and case 2 (red line), respectively. The choice of these two curves is motivated by the fact that they belong to stacks of cathode-supported cells operating with air as sweep gas. More precisely, curve 1 refers to a stack of 6 cells, while curve 2 refers to a stack of 25 cells. These aspects are important as CSCs are the technology the market is focusing on due to their unique advantages and operating life as mentioned in section 2.3.1, while the fact that the curves belong to stacks rather than single cells helps to achieve a simulation closer to reality.

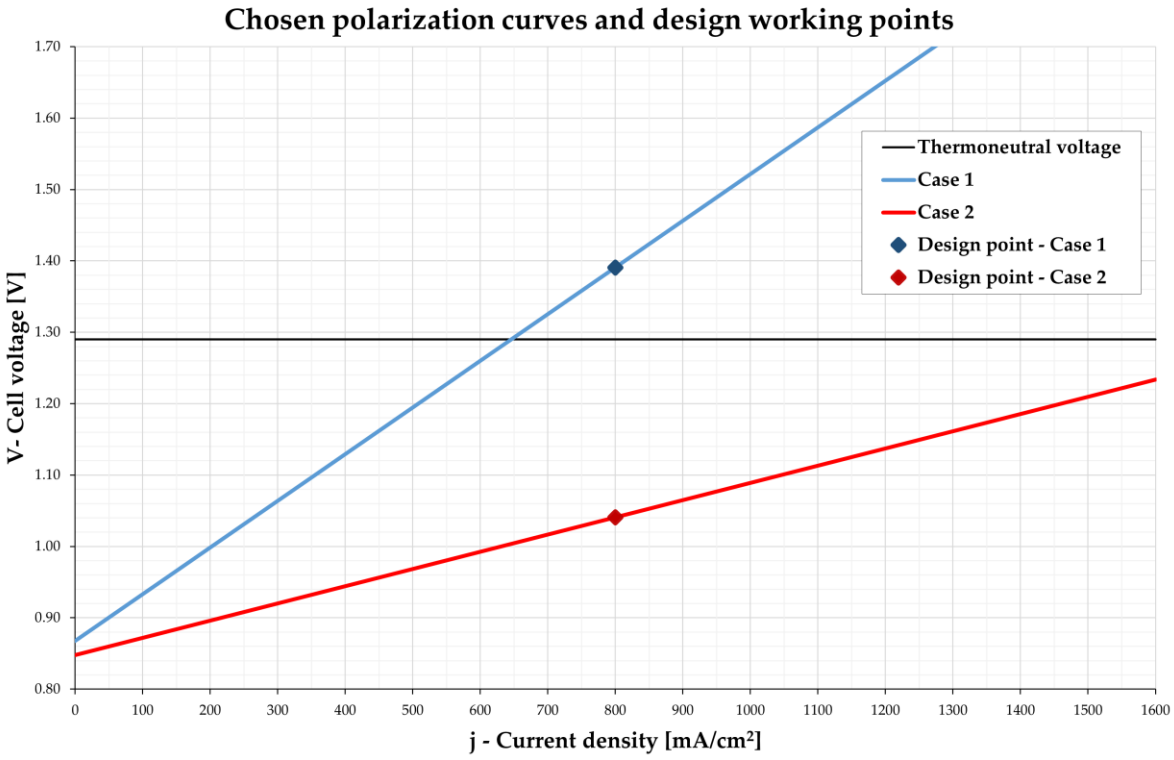

Figure 4.5 - Chosen polarization curves, Cases 1 and 2

The two dots marked on the curves represent the chosen design operating conditions. Current density has been set to a design value of 800 mA/cm^2 coherently with the current efforts to bring operative values up to 1000 mA/cm^2. For the chosen design value of current density, the operating point on curve 1 falls in the exothermic region, while the operative point on curve 2 is the endothermic region (the values of cell voltages are, respectively, $V_{C,1}$=1.39 V and $V_{C,2}$=1.04 V for the two cases, while thermoneutral voltage is V_{TN}=1.29 V). A transition from exothermic to endothermic operation could happen for case 1 if the values of cell voltage and current density should decrease enough (cell voltage below V_{TN}=1.29 V).

According to the adopted nomenclature, the six resulting configurations have been labelled as A1, B1, C1, A2, B2, C2. In these codes, the letter indicates the plant configuration adopted, while the number indicates whether the cells behaviour is described by either curve 1 or 2, as shown in **Errore. L'origine riferimento non è stata trovata.**.

Table 4.1 - Summary of the six configurations

	Case A	**Case B**	**Case C**
Curve 1 – Exothermic operation	A1	B1	C1
Curve 2 – Endothermic operation	A2	B2	C2

Table 4.2 shows some significant design parameters for cases 1 and 2. As it is highlighted by stack inlet and outlet temperatures, exothermic operation implies that for configurations A1, B1 and C1, stack outlet temperature is higher than the inlet. For configurations A2, B2 and C2, instead, stack outlet temperature is lower than the inlet temperature. This is one the reasons why electric heaters have been included in the hydrogen system layouts (more will be explained in section 4.4.2). As the stack outlet streams are colder than inlet during endothermic operation, they are unable to provide all the heat required by the cold-side stream to reach the operative temperature. Thus, stack inlet streams temperature needs to be topped by an external source.

The temperature difference between stack inlet and outlet streams has been set to 100°C, considering the operative temperature reported for the polarization curves as the outlet value. This means that for exothermic cases (1), since the curve is given for a 750°C temperature, the stack inlet temperature has been set to 650°C, while the outlet to 750°C. Whereas, for endothermic cases (2), since the curve is given for an 800°C temperature, stack inlet temperature has been set to 900°, while the outlet to 800°C.

The values of open circuit voltage (OCV), area-specific resistances (ASR) and cell active surface (S) were given as inputs for the plant sizing and modelling processes. The value of S is higher than that reported in the respective polarization curve references, but it is consistent with the values the market is aiming to [64].

Table 4.2 - Significant design parameters for cases 1 and 2

Design parameter	Case 1	Case 2
OCV [V]	0.86767	0.84765
ASR [Ω·cm²]	0.65383	0.24138
$T_{IN,\,STACK}$ [°C]	650	900
$T_{OUT,\,STACK}$ [°C]	750	800
S [cm²]	400	400

4.4 Refining of the base model

The model that served as a foundation for this section of the work [63] was refined with more detailed data. With respect to the base model, pressure drops across the pieces of equipment have been added, so to set precise values of pressure increase for pumps and compressors. Moreover, a few minor adjustments to the overall heat transfer coefficients (U-values) in the heat exchangers have been made.

4.4.1 Pressure drops

To set the same stack operative pressure for all the three layouts, pressure drops across the components had to be considered. The actual value of pressure drops depends on many different parameters, among which the geometry of the component, the nature of the fluids flowing through the component, their velocity, and their mass flow rate. However, since the values of pressure are just slightly above ambient pressure, and flows velocities are modest, pressure drops do not represent a significant source of losses for the system. For this reason, a simplified approach in defining pressure losses has been adopted.

The considered value of pressure drops across the heat exchangers are reported in Table 4.4, while Table 4.3 shows the values of pressure drops across the reactor (SOECs stack) and the electric heaters. For what concerns heat exchangers, the different nature of the fluids flowing at their hot and cold sides has been considered for each heat exchanger in every layout. Values found in literature for similar

applications have been considered for air and vapor flows [65]. In the case of liquid or boiling water flows, a drop of around 5% of the stream pressure has been considered. The values of pressure drop across the reactor and electric heaters have also been taken from literature [65].

In this simplified approach, these values of pressure drops are considered constant for every operative condition and do not vary with mass flow rate as it would happen in real life operation.

For each of the three layouts, the pressure drops for each inlet stream (water and air) have been found as the sum of the single drops across each piece of equipment on their respective path. A small overpressure was imposed at outlet as a further pressure drop added on top of the sum. However, the value of the overpressure varies between the layouts as it was determined so to have the same operative pressure of the stacks for each case (106,325 Pa). Once the resistances to win were found, each pump or compressor was set to provide that amount of pressure to the stream crossing it.

Table 4.3 - Pressure drop in reactor and electric heaters

Component	Pressure drops [kPa]
REACTOR	2
CAT-HTR	0.5
AN-HTR	0.5

Table 4.4 - Pressure drop and circulating fluids in heat exchangers

Heat exchanger	Configuration A				Configuration B				Configuration C			
	Hot-side fluid	Cold-side fluid	Hot-side pressure drop [kPa]	Cold-side pressure drop [kPa]	Hot-side fluid	Cold-side fluid	Hot-side pressure drop [kPa]	Cold-side pressure drop [kPa]	Hot-side fluid	Cold-side fluid	Hot-side pressure drop [kPa]	Cold-side pressure drop [kPa]
HX-PR-CA	Steam + H_2 (27/73%$_{mol}$)	Subcooled Water	1.25	5	Sweep Air	Subcooled Water	1.25	5	Sweep Air	Subcooled Water	1.25	5
HX-SPIL	Steam	Boiling Water	1.25	5	Steam	Boiling Water	1.25	5	Steam	Boiling Water	1.25	5
HX-HT-CA	Steam + H_2 (27/73%$_{mol}$)	Steam + H_2 (90/10%$_{mol}$)	1.25	1.25	Steam + H_2 (27/73%$_{mol}$)	Steam + H_2 (90/10%$_{mol}$)	1.25	1.25	Steam + H_2 (27/73%$_{mol}$)	Steam + H_2 (90/10%$_{mol}$)	1.25	1.25
HX-PR-AN	Sweep Air	Air	1.25	1.25	Sweep Air	Air	1.25	1.25	Sweep Air	Air	1.25	1.25

4.4.2 Heat exchangers sizing

All the heat exchangers have different heat transfer areas which depend on the fluids circulating at both sides, and to the constraints on outlet thermodynamic conditions (specific for each configuration).

Heat exchangers have been sized on Aspen Plus® according to the U-method. Indeed, the heat duty of a heat exchanger ($\dot{Q}$ [W]) can be expressed in two different ways:

$$\dot{Q} = \dot{m} \cdot C_p \cdot \Delta T \tag{4.1}$$

$$\dot{Q} = A \cdot U \cdot \Delta T_{lm} \tag{4.2}$$

In equation (4.1), $\dot{m}$ [kg/s] is the mass flow rate of the stream flowing either at the hot or cold side of a heat exchanger, C_p [J/kg °C] is the specific heat of the substance, and ΔT [°C] is the temperature variation of the flow between inlet and outlet. In equation (4.2), A [m²] is the heat transfer area, U [W/m² °C] is the overall heat transfer coefficient, and ΔT_{lm} [°C] is the log mean temperature of the two streams flowing in the heat exchanger.

By setting outlet stream design specifications (like temperature or vapor quality) and overall heat transfer coefficients for each heat exchanger, the software can size their heat transfer area according to the imposed conditions. During the system sizing phase, a new value of A is found for each iteration. Once the sizing process is completed, the value of A is fixed and the system is tested in off-design conditions, as better explained in chapter 5.

Table 4.5 shows the U values adopted in the sizing process, which are the average values of the ones found in literature [66]–[69]. Their value depends on both the fluids flowing at hot and cold side of heat exchangers. As it was shown in Table 4.4, phase change never happens for any stream in any heat exchanger and is to be avoided if not considered in the heater exchanger design phase. The only exception is represented by the cold side of HX-SPIL (where subcooled water is brought to evaporation temperature, evaporated, and superheated. On a sidenote, no data was found for a steam-steam heat exchanger, thus the U value was assumed at 50 W/m²K, close the one for gas-gas heat exchangers.

The constraints on the physical state of the outlet streams were imposed by setting outlet temperatures which allowed to recover as much thermal energy as possible from the hot streams without incurring in undesired condensation. For cathode outlet streams, this meant bringing them as close as possible to the saturated vapor

condition The conditions imposed for each heat exchanger are shown in Table 4.6 and Table 4.7.

Table 4.5 - Adopted U-values

Hot-side fluid	Cold-side fluid	U values range [W/m²K]	Design U values [W/m²K]
Steam	Subcooled water	300-3,500	1,900
Steam	Boiling water	900-6,000	3,500
Steam	Steam	-	50
Gas (p~p_{ATM})	Gas (p~p_{ATM})	5-50	25
Gas (p~p_{ATM})	Subcooled water	10-300	150

Table 4.6 - Thermodynamic constraints for Cases 1 (exothermic)

Heat Exchanger	A1	B1	C1
HX-PR-CA	$T_{OUT,C}$=97°C $\Delta T_{AP,\,min}$=25°C	$T_{OUT,C}$=97°C $\Delta T_{AP,\,min}$=25°C	$T_{OUT,C}$=97°C $\Delta T_{AP,\,min}$=25°C
HX-SPIL	$T_{OUT,C}$=150°C $X_{OUT,H}$=1	$T_{OUT,C}$=150°C $X_{OUT,H}$=1	$T_{OUT,C}$=150°C $X_{OUT,H}$=1
HX-HT-CA	$T_{OUT,C}$=560°C $\Delta T_{AP,\,min}$=25°C	$T_{OUT,C}$=650°C $\Delta T_{AP,\,min}$=25°C	$T_{OUT,C}$=650°C $\Delta T_{AP,\,min}$=25°C
HX-PR-AN	$T_{OUT,C}$=650°C $\Delta T_{AP,\,min}$=25°C	$T_{OUT,C}$=650°C $\Delta T_{AP,\,min}$=25°C	$T_{OUT,C}$=650°C $\Delta T_{AP,\,min}$=25°C
CAT-HTR	T_{OUT}=650°C	T_{OUT}=650°C	T_{OUT}=650°C
AN-HTR	T_{OUT}=650°C	T_{OUT}=650°C	T_{OUT}=650°C
COGEN	T_{OUT}=40°C	T_{OUT}=40°C	T_{OUT}=40°C

Table 4.7 - Thermodynamic constraints for Cases 2 (endothermic)

Heat Exchanger	A2	B2	C2
HX-PR-CA	$T_{OUT,C}$=97°C $\Delta T_{AP,\ min}$=25°C	$T_{OUT,C}$=97°C $\Delta T_{AP,\ min}$=25°C	$T_{OUT,C}$=97°C $\Delta T_{AP,\ min}$=25°C
HX-SPIL	$T_{OUT,C}$=150°C $X_{OUT,H}$=1	$T_{OUT,C}$=150°C $X_{OUT,H}$=1	$T_{OUT,C}$=150°C $X_{OUT,H}$=1
HX-HT-CA	$T_{OUT,H}$=270°C $\Delta T_{AP,\ min}$=25°C	$\Delta T_{OUT,H-IN,C}$=25°C $\Delta T_{AP,\ min}$=25°C	$\Delta T_{OUT,H-IN,C}$=25°C $\Delta T_{AP,\ min}$=25°C
HX-PR-AN	$T_{OUT,C}$=775°C $\Delta T_{AP,\ min}$=25°C	$T_{OUT,H}$=122°C $\Delta T_{AP,\ min}$=25°C	$T_{OUT,H}$=122°C $\Delta T_{AP,\ min}$=25°C
CAT-HTR	T_{OUT}=900°C	T_{OUT}=900°C	T_{OUT}=900°C
AN-HTR	T_{OUT}=900°C	T_{OUT}=900°C	T_{OUT}=900°C
COGEN	T_{OUT}=40°C	T_{OUT}=40°C	T_{OUT}=40°C

The constraints on hot outlet temperatures for HX-HT-CA in configurations A1 (Table 4.6) and A2 (Table 4.7) are imposed due the need of the hot stream to perform two heat exchanges (hot outlet is sent to HX-PR-CA) without incurring in condensation, and hence a limit on hot stream cooling is necessary. The exact value comes from an iterative process and allows for the maximum heat recovery (constraint on hot outlet temperature set as low as possible).

A similar consideration can be made for constraints on hot outlet temperatures at HX-PR-AN in configurations B2 and C2 (Table 4.7). Here the hot fluid is oxygen-rich air, thus condensation is not an issue. However, after leaving the heat exchanger, the hot stream still must perform heating at HX-PR-CA (Figure 4.3 and Figure 4.4). Hence, the constraint was set by imposing a hot outlet temperature in HX-PR-AN 25°C higher than the cold outlet temperature in HX-PR-CA, that is the minimum approach temperature difference between the two streams.

This constraint is not necessary for the same layouts in exothermic operation (B1 and C1, Table 4.6) as the anode outlet streams are hotter than inlet and their thermal energy is sufficient to perform both heating processes without any need for limitations.

4.5 System sizing procedure

The process adopted for the hydrogen system sizing was the same for all the six configurations (A1, B1, C1, A2, B2, C2). Figure 3.3 in section 3.4 showed the curve of the available power from the NPP as a function of the share of bled steam mass flow rate (ε). The sizing of the hydrogen system for each configuration was carried out by means of an iterative process aimed to find out a value of ε for which the power delivered to the grid was null. In other words, the configurations are sized on a design value of ε such that, when operated a design conditions, the hydrogen system will absorb all the electric power made available by the NPP.

As already mentioned, the sizing phase of the hydrogen system was carried out on Aspen Plus®. The integration with the NPP was simulated by implementing the third-grade polynomial function describing the power available from the NPP as a function of ε (the green line in Figure 3.3) in the Microsoft Excel solver used in Aspen Plus®. A first-try value of ε was chosen and a preliminary sizing of the system was achieved. For each step of the iterative process, the software would resize all the components in the hydrogen system both at system-level (number of modules N_{MOD}) and module-level (heat exchangers, pumps, and compressors). Eventually, the process converged to a design point at which the condition of no energy delivered to the grid is satisfied.

Once the design of each configuration was complete, the total number of modules of the system was found, together with the size of their components. As a reminder, for cases A and B every piece of equipment was sized at module-level. On the other hand, for cases C, the HX-SPIL was sized at system level, with only one single piece of equipment serving all the modules at the same time.

5. Preliminary analysis and integrated system operation

This chapter will show the results from the hydrogen system sizing phase and a preliminary analysis to assess the differences emerged in the process. Then, a description of the criteria and the strategies adopted to operate the hydrogen system in off-design conditions will be provided.

5.1 Preliminary analysis

Given the large number of considered configurations, a preliminary analysis was carried out to assess whether significant differences between the configurations were already present at design conditions. The aim is to assess eventual pros and cons that may already be showing at design conditions, potentially favouring some configurations, or excluding them from further analysis.

5.1.1 Key performance indicators

The analysis was based on some significant quantities resulted from the sizing process, and a few key performance indicators (KPIs) listed in the following.

- Stack electric efficiency ($\eta_{EL,ST}$): it is defined as the ratio of the hydrogen mass flow rate production of a stack times hydrogen LHV, over the electric power consumption of a stack. It indicates how efficient is the electrolysis process alone, without considering the thermal flows involved in the process. It is expressed as:

$$\eta_{EL,ST} = \frac{\dot{m}_{H_2,OUT-ST} \cdot LHV_{H_2}}{\dot{W}_{EL,ST}} \tag{5.1}$$

- Module electric efficiency ($\eta_{EL,MOD}$): it is defined as the ratio of the net hydrogen mass flow rate production of a module times hydrogen LHV, over the electric power consumption of a module (namely the power consumption of the pump, compressors, electric heaters, and stacks). The hydrogen mass flow rate considered is netted of the recirculation share, so it is the actual useful production of a module. It is expressed as:

$$\eta_{EL,MOD} = \frac{\dot{m}_{H_2,OUT-MOD,NET} \cdot LHV_{H_2}}{\dot{W}_{EL,MOD}} \tag{5.2}$$

- Module first-law efficiency ($\eta_{I,MOD}$): it is defined as the ratio of the net hydrogen mass flow rate production of a module times the hydrogen LHV, over the total energy consumption of a module. It accounts for both the electric and thermal power consumption of a module. In particular, the thermal power coincides with the thermal duty of HX-SPIL, that is the thermal power drawn from the NPP. The hydrogen mass flow rate considered is netted of the recirculation share, so it is the actual useful production of a module. It is expressed as:

$$\eta_{I,MOD} = \frac{\dot{m}_{H_2,OUT-MOD,NET} \cdot LHV_{H_2}}{\dot{W}_{MOD}} \tag{5.3}$$

- Module first-law efficiency with heat recovery ($\eta_{I,MOD\text{-}HR}$): it is the same as the module first-law efficiency, but it also accounts for heat recovery from hot anode outlet streams as a useful byproduct by adding it at the numerator. It is expressed as:

$$\eta_{I,MOD-HR} = \frac{\dot{m}_{H_2,OUT-MOD,NET} \cdot LHV_{H_2} + \dot{W}_{COGEN}}{\dot{W}_{MOD}} \tag{5.4}$$

- System first-law efficiency ($\eta_{I,SYS}$): it is the same as the module first-law efficiency, but it accounts for system-level quantities. It is expressed as:

$$\eta_{I,SYS} = \frac{\dot{m}_{H_2,OUT-SYS,NET} \cdot LHV_{H_2}}{\dot{W}_{SYS}} \tag{5.5}$$

5.1.2 Preliminary analysis results

Table 5.1 and Table 5.2 provide an overview of the listed parameters and other significant physical quantities for all the configurations. It is important to remember that this first analysis is only based on the steady-state performances at design condition of the six configurations. Indeed, chapter 5 will deal with the steady-state operation of the different configurations over the whole ε operational range, that is at partial load.

What immediately stands out is that all the six configurations are composed by the same number of modules (18), and hence operate with the same number of SOECs, allowing for a fair comparison without imbalances that may have been caused by differently sized systems. This is evident when noticing that the thermal duty of HX-SPIL is roughly the same for all configurations, as the value of ε at design point only changes of a few decimal percentage points among the configurations.

Hydrogen production is very similar for all the configurations, with small differences between the configurations in the range of 4-10 g_{H2}/s. This is because each configuration is sized at a slightly different ε, so the inlet water mass flow rate slightly changes between the configurations, while the UF is constant. However, inlet air mass flow rates are significantly different between exothermic (1) and endothermic (2) cases. This is because in endothermic operation, the operative point on the polarization curve is relatively further from thermoneutral condition with respect to exothermic case (Figure 4.5). This means that larger amounts of heat are involved in the electrolysis reaction for the same amount of processed water. Thus, since the relative temperature difference between stack inlet and outlet flows is the same, a higher mass flow rate is needed for case 2.

Table 5.1 – Significant quantities of system sizing (1)

Physical quantity		Exothermic configurations			Endothermic configurations		
		A1	B1	C1	A2	B2	C2
SOEC details	N_{MOD} [-]	18	18	18	18	18	18
	N_C [-]	270,000	270,000	270,000	270,000	270,000	270,000
	j_{REAL} [A/cm²]	0.791	0.796	0.796	0.7952	0.7870	0.7872
	V_{CELL} [V]	1.385	1.388	1.388	1.0396	1.0376	1.0376
	V_{STACK} [V]	415.407	416.344	416.345	311.8747	311.2841	311.2948
System-level	ε_{DESIGN} [%]	25.3%	25.5%	25.5%	25.5%	25.2%	25.2%
	m_{ε} [kg/s]	132.1	132.9	132.9	132.8	131.4	131.4
	$m_{H20\text{-}IN\text{-}SYS}$ [kg/s]	11.3	11.4	11.4	11.4	11.3	11.3
	$m_{AIR\text{-}IN\text{-}SYS}$ [kg/s]	48.8	51.4	53.0	155.5	156.1	155.8
	$m_{H2\text{-}OUT\text{-}SYS}$ [kg/s]	0.9	0.9	0.9	0.9	0.9	0.9
	$W_{SYS,el}$ [MW_e]	127.286	125.896	125.889	126.049	128.431	128.501
	$S_{HX\text{-}SPIL}$ [m²]	-	-	240.708	-	-	232.125
Module-level heat exchangers surfaces	$S_{HX\text{-}PR\text{-}CA}$ [m²]	13.730	13.114	13.196	15.140	33.560	33.561
	$S_{HX\text{-}SPIL}$ [m²]	13.414	13.541	13.3703*	13.497	13.206	12.896
	$S_{HX\text{-}HT\text{-}CA}$ [m²]	72.431	267.497	266.983	85.007	279.318	279.422
	$S_{HX\text{-}PR\text{-}AN}$ [m²]	525.081	554.846	565.354	6877.833	3586.013	3580.225
Module-level mass flow rates	$m_{H20\text{-}IN\text{-}MOD}$ [kg/s]	0.6	0.6	0.6	0.6	0.6	0.6
	$m_{AIR\text{-}IN\text{-}MOD}$ [kg/s]	2.7	2.9	2.9	8.6	8.7	8.7
	$m_{H2\text{-}OUT\text{-}NET,\ MOD}$ [kg/s]	0.05	0.05	0.05	0.05	0.05	0.05

* This area is obtained dividing the area of the system-level heat exchanger by the number of modules

Table 5.2 - Significant quantities of system sizing (2)

	PHYSICAL QUANTITY	CONFIGURATIONS					
		EXOTHERMIC			ENDOTHERMIC		
		A1	B1	C1	A2	B2	C2
Module-level powers	$W_{ST,el}$ [kW]	131.395	132.487	132.488	99.197	97.993	98.015
	$Q_{CAT-HTR}$ [kWth]	136.111	0.002	0.002	459.849	329.979	330.155
	Q_{AN-HTR} [kWth]	-0.001	-0.001	-0.001	1262.282	1585.727	1590.307
	$W_{PUMPW,el}$ [kWe]	0.047	0.049	0.049	0.047	0.048	0.048
	$W_{COMP-H2,e}$ [kW_e]	1.018	0.780	0.772	1.020	0.771	0.774
	$W_{COMP-AIR,e}$ [kW_e]	18.771	20.395	19.989	58.646	61.010	58.967
	$W_{BOP,MOD}$ [kW_e]	155.945	21.225	20.810	1781.844	1977.535	1980.250
	$W_{MODULE,e}$ [kW_e]	7071.450	6994.216	6993.837	7002.716	7135.072	7138.935
	$Q_{HX-SPIL}$ [kW_{th}]	1568.878	1578.719	1579.789	1577.636	1560.768	1561.284
	Q_{COGEN} [kW_{th}]	560.776	341.735	345.653	435.214	520.630	521.642
Efficiencies	$\eta_{EL,ST}$ [-]	90.5%	90.3%	90.3%	120.5%	120.8%	120.8%
	$\eta_{EL,MOD}$ [-]	84.1%	85.5%	85.5%	85.4%	82.9%	82.9%
	$\eta_{I,MOD}$ [-]	68.8%	69.8%	69.8%	69.7%	68.1%	68.0%
	$\eta_{I,MOD-CONGEN}$ [-]	75.3%	73.8%	73.8%	74.8%	74.0%	74.0%
	$\eta_{I,SYS}$ [-]	68.8%	69.8%	69.8%	69.7%	68.1%	68.0%

The pump and hydrogen compressor power consumption are roughly the same among the configurations, and overall negligible. Air compressors, on the other hand, show a higher power consumption for endothermic cases since the air mass flow rate is higher, as previously explained. However, the share of power consumption that they represent over the total is still negligible. This means that pumps and compressors should not be a significant factor in the system analysis given their marginal role.

Moving to the SOECs electric performances, the stack electric performances show significant differences between cases 1 and 2. In cases 1, the electric consumption of a single stack results higher due to the higher energy consumption of the electrolysis reaction, resulting in a lower stack electric efficiency. The opposite is true for cases 2, where the reaction is less demanding in terms of power and a higher stack electric efficiency can be achieved with the same amount of produced hydrogen.

The module electric and first-law performances are affected by the total electric and power consumption, keeping in mind that the useful effect (produced hydrogen mass flow rate) is roughly the same for all configurations. The only source of consumption that still must be investigated are the electric heaters. Starting from anode-side heaters (AN-HTR), it stands out that their power consumption is roughly null for all cases 1, as the anode outlet streams are enough to bring inlet to its operative temperature without the need for an external source. This is not true for cases 2, where outlet is colder than inlet, and the operative temperature cannot be reached by only means of HX-PR-AN. This causes a significant power consumption for anode-side electric heaters, also caused by the larger air mass flow rates circulating with respect to cases 1.

A few more distinctions are needed for cathode-side electric heaters (CAT-HTR). In general, cases A show a higher power consumption than cases B and C for the same SOEC operative condition (1 or 2). This is because in cases A, cathode outlet streams must perform two heating processes (HX-HT-CA and HX-PR-CA), so the amount of heat that can be provided at the first heat exchanger on their path (HX-HT-CA) is limited, as the outlet hot flow must have enough thermal power to perform heating at the second heat exchanger (HX-PR-CA) without condensation at hot outlet side. This will cause the impossibility to reach operative temperature at HX-HT-CA cold outlet, raising the need for an external source to top up the difference (CAT-HTR). For cases B and C, instead, cathode outlet performs heating only at HX-HT-CA, allowing for a higher heat transfer without incurring in undesired condensation and reducing the need for an external heating source to reach operative temperatures. For cases B1 and C1, the thermal duty of CAT-HTR is null as HX-HT-CA is enough to bring the cold stream at operative temperature (exothermic condition). For cases B2

and C2 the thermal power of CAT-HTR is reduced with respect to A2 but is still significant due to the endothermic operation (at HX-HT-CA, hot inlet temperature is lower than operating temperature and the heater is still required). These constraints are reflected by the temperature values set for the heat exchangers sizing phase. In the end, the higher power consumption for cases 2 with respect to 1 flattens out the advantage represented by a lower electrolysis power demand, causing the total power consumption of the modules to be roughly the same for all the six configurations.

Lastly, some differences between the heat exchangers surfaces can be noticed. The first significant difference, of course, is in HX-SPIL for cases C as they are sized on system level, which will cause these heat exchangers to have a significant surface. When dividing the total surface among the number of modules, however, surface values very close to cases A and B are found, showing how the modularity concept is still respected by this configuration. Further differences lie between the surfaces of HX-HT-CA between cases A and the others. In particular, the surface is smaller in cases A than in B and C (in which is roughly the same) since, as explained above, the thermal duty is limited by the nature of the system layout. Similarly, a significant difference arises for the surface of HX-PR-AN for configurations A2, which is almost double than that of configurations B2 and C2 because of the unconstrained cooling of the anode outlet streams. Moreover, the large amounts of circulating mass flow rates will cause the surfaces of HX-PR-AN for cases 2 to be significantly higher than the corresponding in cases 1.

In conclusion, the plant layout does not represent a significant factor at design steady-state operation since the advantages and drawbacks of each configuration balance out, leading to similar performances. This is clear looking at the efficiencies, which show minor differences between the configurations. The balancing effect is evident when comparing stack and module electric efficiencies: as expected, values of stack electric efficiencies around 90% and 120% are achieved for cases 1 and 2, respectively. However, no significant difference can be appreciated between module electric efficiencies, showing once again the major role played by electric heating.

As the layout for cases C does not provide any significant advantage in exchange for a reduced flexibility (only one HX-SPIL during partial operation), it was decided to exclude cases C from further analysis. The reason behind this is to maintain the modular flexibility provided by cases B given the lack of appreciable advantages in the use of configuration C in its place. Given all the considerations above, the partial load analysis will be performed only on configurations A1, B1, A2 and B2.

5.2 Integrated system off-design operation

The next step is to provide an analysis of the steady-state operation of the hydrogen system over the whole operational range, comparing the performances of the four remaining configurations (A1, B1, A2, B2). The aim is to provide an "operating map" of the integrated system as ε varies between 0% and the design value for each configuration, pointing out how both the thermal and electrical power from the NPP is used within the hydrogen system. This will help to identify the potential critical aspects, suggesting where further studies could focus to improve flexibility and efficiency of the integrated system.

The analysis was carried out on Aspen Plus®, while fixing the sizing of each configuration according to the data shown in Table 5.1 (SOEC details and module-level heat exchangers surfaces), allowing the simulation of the off-design operation of the integrated system.

The range for off-design (ε varying between 0% and design values) was discretized in steps of 1% each, with a maximum value of ε=25% for all the configurations. This allowed to test the four configurations with the exact same amount of steam from the NPP, providing for a fair comparison in each working point all along the operative range.

In this section of the work the number of modules is manually adjusted for every step of the simulation process so that that some internal operating conditions (which will be better explained in the following) are satisfied. In the system sizing phase, instead, the number of modules for each configuration was a variable to be determined. At design conditions, all the modules are operative, and their number is the design value.

The active modules in every operative condition were imposed to work at the same load, and both the power consumption of the system and the hydrogen production are equally split among the active modules. This means that as ε decreases from the design value, the amount of steam bled from the NPP towards the hydrogen system reduces more and more. This will cause the components of the system to work at partial load, until eventually one (or more) module will have to be shut down and the number of active modules will decrease accordingly. At ε=0% the hydrogen system is completely off (in reality, it would be in hot-standby mode), none of the modules is active and all the power available from the NPP is delivered to the grid.

A detailed description of the regulation strategy adopted for partial load simulation for each configuration will be provided in the following sections of this chapter. The results will be presented and discussed in chapter 6 using the same KPIs already introduced in section 5.1.1.

5.2.1 Configuration A1

In configuration A1, the stacks operate in exothermic conditions, and the fuel and air lines never interact with each other. Cathode outlet streams perform heating on the water line, while anode outlet heats inlet air.

The design working condition on the polarization curve for exothermic operation was shown in Figure 4.5. As known from SOEC theory, stack and module electric and first-law efficiencies in exothermic operation are higher when the operating point on the polarization curve is closer to the thermoneutral condition, which means that the system benefits from operating at lower values of current densities and cell voltage. To achieve this condition when the modules are performing at partial load, it is sufficient to keep as many active modules as possible, so to reduce the duty of the active stacks. For this reason, the strategy adopted for regulation in exothermic conditions (configurations A1 and B1) was to reduce ε from 25% to 1%, keeping as many active modules as possible for each step of the simulation.

Providing the hydrogen system with gradually decreasing steam mass flow rates from the NPP will reduce the available thermal power and increase the electricity generation (as less steam is bled, the steam circulating in the NPP power block increases and, consequently, the electric power production too). The reduction in thermal power available for evaporation in HX-SPIL (linearly proportional to ε) reflects into a decrease of the system/module inlet water mass flow rate as ε is reduced.

Mass flow rates cannot be decreased at will, as different problems could arise (bad circulation, increased pressure drops) if the circulating mass flow rate becomes too small. A lower limit of 10% the nominal mass flow rate has been adopted for every section of the plant layout in every layout (this also applies for configurations B1, A2, B2).

When this condition is met anywhere within the system, one (or more) module is forced to shut down and a new working condition with a smaller number of active modules is found. This will cause the circulating mass flow rates in the system to be split between a smaller number of modules, whose circulating mass flow rates will increase. However, this will also move the stacks operating point further from the thermoneutral condition.

As the circulating mass flow rates reduce, heat exchangers become oversized and their effectiveness increases. Recalling equations (4.1) and (4.2), an increase in the exchanged heat over smaller mass flow rates causes temperatures to change. This effects is moderate since the part-load level of each module varies limitedly; at any rate, further analysis will focus on the partial load behaviour of heat exchangers, for instance revising the assumption of constant U. Considering a constant inlet temperature for booth hot and cold side streams, for a cooling stream (hot side) outlet temperature will decrease, while the outlet temperature will increase for

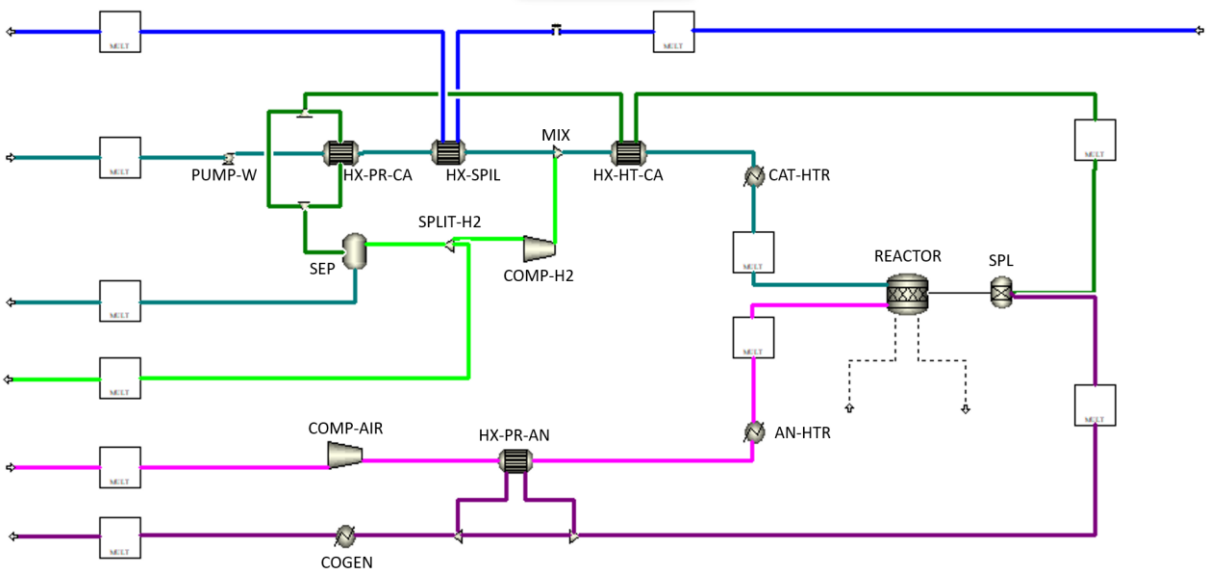

heating streams (hot side). This phenomenon could generate undesired conditions within the hydrogen system, which can be prevented with the adoption of some simple design features.

Figure 5.1 – Configuration A1: bypasses added for off-design operation

To keep the simulation process as simple as possible, hot-side bypasses have been adopted whenever the cold side stream of a heat exchanger would face an undesired condition if no measures were taken. This was achieved by means of splitting and mixing valves (Figure 5.1) which allowed to send through the hot side of the heat exchanger the exact mass flow rate to achieve the desired condition at cold outlet.

A bypass was introduced to the hot side of HX-PR-CA to avoid premature water evaporation at its cold side, keeping the cold side stream outlet temperature to 97°C, maintaining a few degrees of subcooling before entering HX-SPIL.

A decrease in the inlet water mass flow rate to the system/module also causes a reduction of inlet air mass flow rate. When considering a partial load in the exothermic electrolysis range, a reduced current density will correspond to a lower

thermal power generation, and therefore less air is needed for the heat extraction at anode side. Hence, a further bypass was adopted for hot side of HX-PR-AN (Figure 5.1) to prevent the cold side outlet temperature from exceeding the nominal stack inlet temperature (that is, maintaining the temperature difference between stack inlet and outlet as constant as possible).

5.2.2 Configuration B1

Considerations made in section 5.2.1 for exothermic operation and modules activation strategy are also valid for configuration B1. However, with this system layout, the anode outlet streams perform both inlet air heating in HX-PR-AN and inlet water preheating in HX-PR-CA. The cathode-side outlet streams, instead, are only used for cathode inlet superheating in HX-HT-CA.

As shown in Figure 5.2, three bypasses were necessary in this configuration. The first two are the same already discussed for configuration A1 in section 5.2.1, with the only difference being that in configuration B1, oxygen-rich air flows at the hot side of HX-PR-CA. However, this aspect has no practical influence in system regulation. The third and last bypass was added to the hot side of HX-HT-CA.

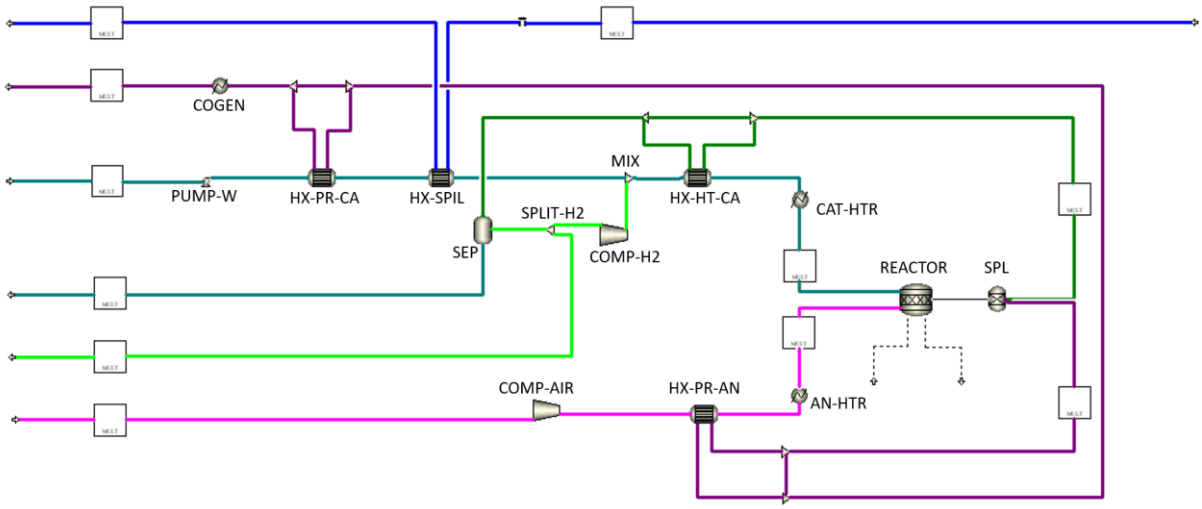

Figure 5.2 - Configuration B1: bypasses adopted for off-design operation

The reason because this bypass was necessary for configuration B1 but not for configuration A1 lies in the different sizing criteria for HX-HT-CA. Indeed, as it was shown in Table 4.6 and explained in section 4.4.2, in configuration A1 this heat exchanger was sized so to have a cold outlet temperature of 560°C, well below the stack operative temperature (650°C). This choice was necessary to avoid an excessive cooling of the cathode exhaust and prevent its condensation in the downstream heat exchanger. This design never allows the cold outlet temperature to exceed 650°C for

any off-design operative condition. In contrast, for configuration B1, HX-HT-CA has been sized so to have a cold outlet equal to the stack inlet temperature. Just like for HX-PR-AN, this would cause the cold outlet temperature to exceed the stack design inlet temperature when the heat exchanger becomes oversized, and no regulation is adopted.

5.2.3 Configuration A2

As in the case of configurations A1 and B1, the following considerations on endothermic operation are generic, and hence will apply both to configurations A2 and B2 despite their different plant layout. In the case of endothermic stack operation (outlet streams are colder than inlet and thermal energy must be provided to the cells), the number of active modules is determined according to a different logic.

The design working condition on the polarization curve for endothermic operation was shown in Figure 4.5. As known from SOEC theory, the stack electric efficiency in endothermic operation becomes higher when the operation point on the polarization curve is moved further from the thermoneutral condition, that is at lower values of current densities and cell voltage. However, in contrast with exothermic operation, module electric and first-law efficiencies behave differently from the stack electric efficiency. More specifically, module electric and first-law efficiencies for endothermic operation increase when the operative point is brought closer to the endothermic condition, that is to higher values of current density and cell voltage. This happens because the closer is the operating point to the thermoneutral conditions, the lesser is the absolute quantity of heat involved in the electrolysis process and, hence, air mass flow rate necessary to provide heat. As for endothermic configurations inlet streams need heat from the electric heaters to reach the design stack inlet temperature, reducing the amount of air will reduce the electric heaters power consumption and, consequently, increase module electric and first-law efficiencies. This last effect is the one which affects the hydrogen system performances the most, as the system has an overall benefit from operating to values of current densities higher than the design one. More on this will be discussed in chapter 6.

To pursue this condition, active modules need to be “overloaded” (i.e., they must operate at current densities higher than the design value), and this is achieved by activating as few modules as possible. For this reason, the strategy adopted to find the number of active modules that satisfies the operating constraints in endothermic conditions (configurations A2 and B2) while optimizing the first-law efficiency was to increase ε from 1% to 25%, keeping as few active modules as possible for each step of the simulation.

However, current density cannot be increased at will as cells lifetime is strongly affected by high values. As SOECs durability is a main parameter of concern, an upper limit is required so to determine when a further module (or more) needs to be activated to decrease the operative current density. The limit was set to 1000 mA/cm^2, which may be a slightly high value for state-of-the-art cells, but market is moving to achieve even higher operative current densities given the advantages it represents [70]. So, this value is perfectly coherent with an operative condition which should be commonly supported in the next years.

Configuration A2 operates in endothermic conditions and the fuel and air lines never interact with each other. Cathode outlet streams perform heating on the water line, while anode outlet heats inlet air.

In endothermic operation, internal heat recovery does not suffice to bring the inlet streams to stack operative temperature as stack outlet streams temperature is lower than the operative one, and electric heaters are needed to top up with the missing thermal energy. Moreover, the choice to operate with as few active modules as possible implies that the heat exchangers deal with mass flow rates higher than design and do not become oversized as in configurations A1 and B1. For these reasons, inlet streams overheating is not an issue, and no bypasses are needed for configuration A1 (Figure 5.3).

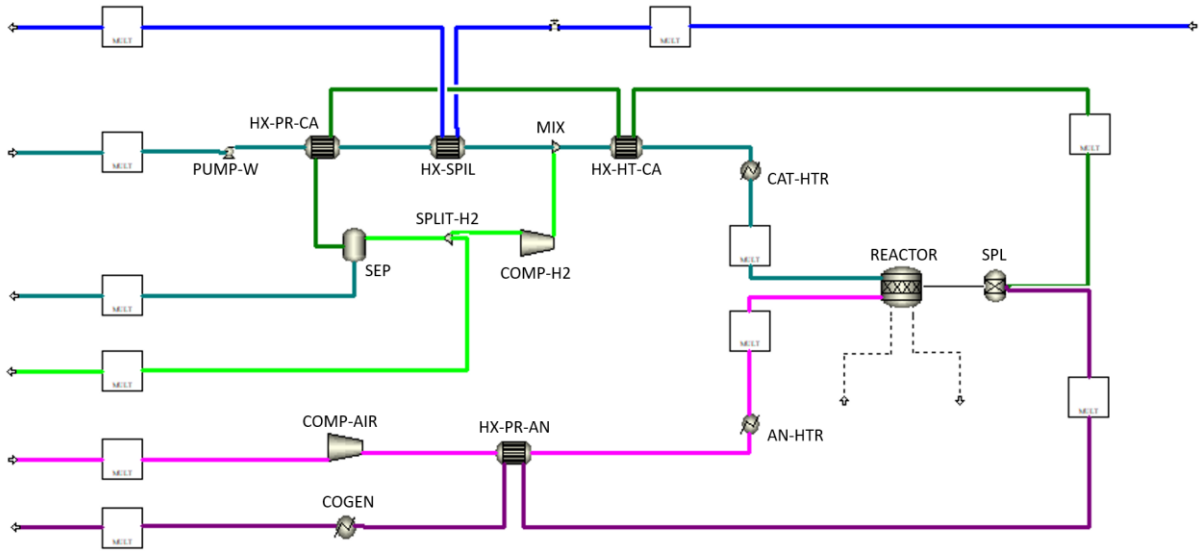

Figure 5.3 - Configuration A2: off-design operation layout

However, another issue emerges from endothermic operation. When the number of active module must be increased due to current density limitations, the operating conditions with the higher number of modules causes the current density to decrease below the design value. In this case, condensation at hot side of HX-PR-CA (stream

composed of water vapor and hydrogen) could occur because of the heat exchanger becoming oversized. This is an undesirable phenomenon which should be avoided if occurring with a significant frequency. However, since this only happens for very low values of operative current density which may be reached only for low values of ε, this is not a particular issue over the operative range. Whereas, it has been used as a further criterion to determine the number of active modules at any working condition. Coherently with the decision to keep the values of current densities below a certain threshold to extend cells lifetime, one more constraint was added in the process to determine the number of active modules.

For each value of ε in the operative range, two checks were performed. The first step was to find an operating point for a certain number of modules N_{MOD}=n, which pushed current densities above the design value (800 mA/cm^2) but still below the limit value. Then, a second check was performed with N_{MOD}=n+1, so to decrease the operative current density. If no condensation of hot streams occurred, N_{MOD}=n+1 was chosen as the final number of active modules for that value of ε. Operating with a higher number of active modules than the one allowed by the constraint on current density penalizes the module electric and first-law efficiencies, but positively impacts on cells durability. Economic considerations can be made on the topic, so to determine if a more conservative strategy as the one described is also economically advantageous or not.

5.2.4 Configuration B2

In this configuration, anode outlet streams are responsible for two heating processes. For this reason, a bypass on the hot side of HX-PR-AN was added (Figure 5.4). Differently from any case seen so far, the objective of this bypass was not to avoid overheating of the cold side stream (this condition cannot be achieved in endothermic operation), but to make sure that the hot outlet stream temperature was high enough to perform water preheating at HX-PR-CA. Preventing part of the stream to go through the hot side at HX-PR-AN causes a decrease in exchanged thermal power, leading to a lower cold outlet temperature and, consequentially, to an increase of thermal duty of AN-HTR. The control logic on the valve was to guarantee a temperature of 97°C at HX-PR-CA cold outlet.

Undesired condensation was not an issue for this configuration as the cathode outlet stream performs only one heating process (hot side of HX-HT-CA), and the hot outlet temperature is well above saturation.

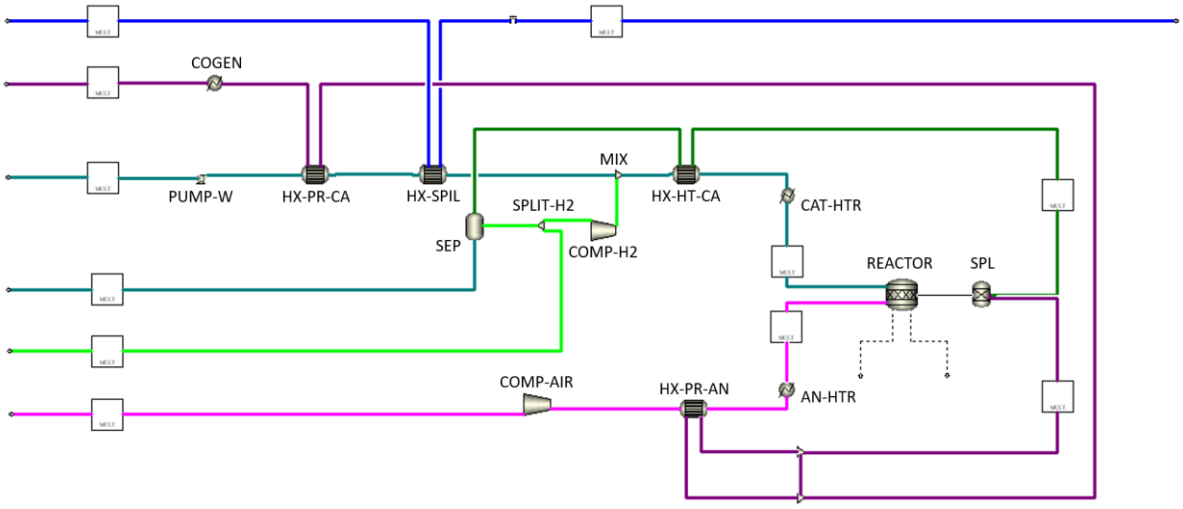

Figure 5.4 – Configuration B2: off-design operation layout

6. Results and discussion

The results from the off-design simulations will be presented and discussed in this chapter. First, the results for hydrogen production will be introduced and discussed. Then, the discussion will move to the key performance indicators (KPIs) introduced in section 5.1.1, which refer also to the integrated system. Other significant physical quantities will be considered to provide a comprehensive picture of the hydrogen system operation over the whole operative range and explain the trends of the KPIs. For the sake of clarity in the discussion, the results will be presented starting from stack level, then the results at module-level will be introduced and the overall performance of the system will be gradually discussed.

6.1 Hydrogen production

This section will deal with the total net hydrogen production from the system. In Figure 6.1 the trends for all the considered configurations (A1, B1, A2, B2) are shown.

The linear behaviour over the whole operative range is immediately visible, as expected from the imposed working conditions. Indeed, the amount of inlet water that will be used for electrolysis is linearly dependent on the amount of heat from the NPP, and hence from the quantity of bled steam (ε). Since the modules are imposed to work at constant utilization factor (UF), the share of water converted into hydrogen is constant over the whole operative range.

Another aspect to consider is that the trend lines of the four configurations almost perfectly overlap both for hydrogen production and water consumption. This is because despite different layouts for internal heat recovery and different SOECs operating conditions (exothermic or endothermic), the four configurations use the same logic for inlet water admission and the same UF.

The result is that hydrogen production alone cannot be a significant parameter to discriminate one configuration over the others, and a more exhaustive analysis of the system is needed before any conclusion can be made.

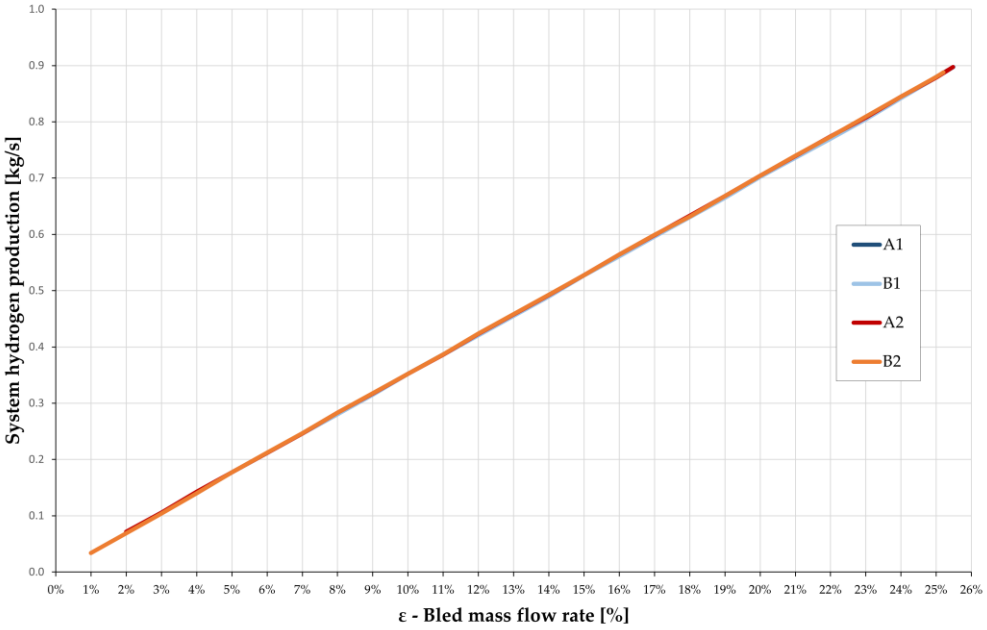

Figure 6.1 - System hydrogen production

6.2 Stack electric efficiency

The stack electric efficiency accounts for the net hydrogen production and the electric power consumption of a stack, meaning that only the electric power directly involved in the electrolysis process is considered, as expressed in Equation (5.1). Figure 6.2 shows the trends of the stack electric efficiency for all the configurations (A1, B1, A2, B2). The values of ε over the operative range can be read on the x-axis. The solid lines in the upper part of the chart represent the values of the stack electric efficiency over the whole operative range, whose values can be read from the left y-axis. The bars in the bottom part of the chart represent the number of active modules for a given value of ε for the four configurations, and their number can be read on the right y-axis.

For a better understanding, red and orange have been used for configurations operating in exothermic conditions (A1, B1), while blue and light blue have been used for configurations operating in endothermic conditions (A2, B2).

A first consideration can be made on the number of active modules, which is also valid for the figures showing the other KPIs in the following sections. The two regulation strategies adopted for exothermic and endothermic operation affect the number of active modules along the operative range, with exothermic configurations (A1 and B1) generally having a larger number of active modules with respect to endothermic (A2 and B2), coherently with the observations in sections 5.2.1 and 5.2.3.

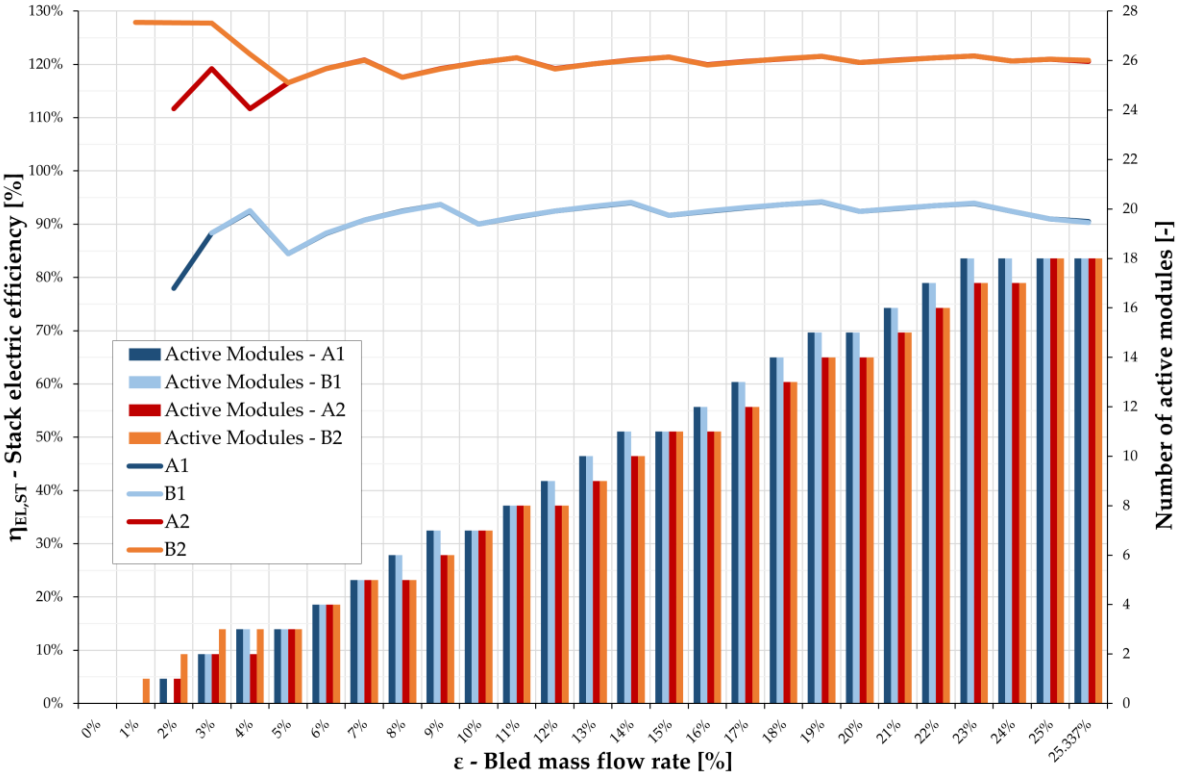

Figure 6.2 - Stack electric efficiency over the operational range

Moving from higher to lower values of ε, the pattern of the active modules becomes irregular when ε drops below 4-5%. As it will be explained, this factor will affect the behaviour of the KPIs in this region.

As expected from theory (see section 2.3), configurations with endothermic stack operation have a higher stack electric efficiency (up to 120%) with respect to exothermic ones (around 90%) as they can offset part of the electric power required by electrolysis with thermal power. Since hydrogen production is nearly the same for all the configurations (Figure 6.1), a lower stack electric power consumption translates in higher stack electric efficiencies.

By looking at the trends in Figure 6.2, it is clear how only configuration B2 reaches the limit of the operational range (ε=1%), while A1 and A2 stop at ε=2%, and B1 at ε=3%. However, operation in this range of small ε values is a limit conditions, and potentially is not essential for real-life operation. The reason why these three configurations face an early shut down is that it was impossible to find a valid operating point for any number of active modules within the boundaries set for current density (below 1 A/cm^2) without incurring in either too small flowing stream rates (A1 and B1) or undesired condensation of hot streams (A2). For the sake of

clarity in the discussion, more on this matter and on the instability of the trends in the region for low values of ε will be discussed in the next section.

6.3 Module electric efficiency

Now that the stacks behaviour has been described, the discussion can be moved to a higher level of complexity, and the module-level quantities will be now analysed. Since active modules are imposed to work in the same conditions, absolute quantities at system-level (e.g., mass flow rates) can be simply obtained by multiplying the module-level quantities by the number of active modules.

The module electric efficiency accounts for the net hydrogen production of a module and its total electric power consumption, as it is expressed in Equation (5.2). The total electric power consumption of the module is the sum of the power consumption from the stacks, the electric heaters, and the machines (pump, and compressors). However, as it will be shown in the following, the power consumption of the electric machines is negligible, and the attention can be focused on the stacks and the electric heaters only.

6.3.1 Anode-side electric heater power consumption

To explain the trends for the anode-side electric heaters power consumption, it is useful to start by look at the trends for the cells' operating voltage over the operational range shown in Figure 6.3. The first thing that can be pointed out is that due to the operating limits imposed to the modules, no transition to endothermic behaviour occurs for configurations A1 and B1 as operating voltage never reaches the thermoneutral voltage or drops below. Instead, this result was widely expected for configurations A2 and B2 as transition to exothermic behaviour would occur for values of current density well above the imposed limit (Figure 4.5).

It is clear how exothermic configurations (A1, B1) operate at values of cell voltage closer to thermoneutral with respect to exothermic ones (A2, B2). This reflects the respective design condition for the cases (Figure 4.5). The main consequence for this is that electrolysis for A1-B1 involves less heat on absolute value with respect to A2-B2 given the proximity to the thermoneutral condition.

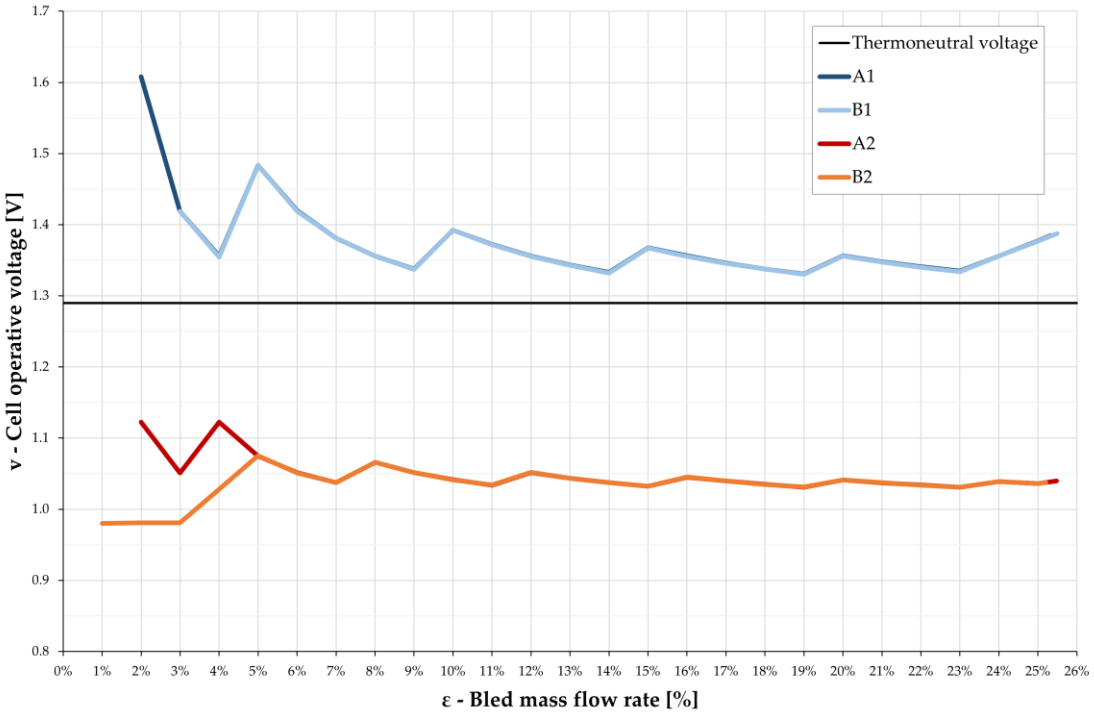

Figure 6.3 – Cells' voltage over the operative range

The result is that the endothermic configurations (A2, B2) need much larger air mass flow rates at anode side to perform temperature regulation of the stacks with respect to the exothermic configurations (A1, B1), as clearly visible in Figure 6.4. This effect is evident when looking at the surfaces of the heat exchangers for the different configurations in Table 5.1: while the surfaces of the heat exchangers at cathode side are similar for all the configurations, the area of HX-AN-PR is significantly larger for A2 and B2 due to the larger quantities of heat (and hence, air mass flow rate) involved in the sizing process.

Looking at the system air consumption for A1 and B1 in Figure 6.4 is evident that, despite being lower, the values fluctuate significantly with respect to those for A2 and B2. This can be addressed to the width of band of cell voltage values in which A1 and B1 operate. Indeed, looking back at Figure 6.3, it is evident how A2-B2 operate in a much narrower band, with minor fluctuations of cell voltage. Configurations A1-B1, instead, operate over a wider band of values, causing a relatively larger shift with respect to the thermoneutral condition with respect to A2-B2.

This phenomenon can be explained by the larger slope of the polarization curve for case 1 with respect to that for case 2 (Figure 4.5): for the same variation in current density, larger variations in cell voltage are achieved in cases1 with respect to cases 2.

This means that the quantity of air required by the module face larger fluctuations, reducing significantly as the operating voltage approaches the thermoneutral. On the other hand, as the trend of cell voltage for configurations A2-B2 is almost a horizontal line, the trend for the system air consumption will almost show a linear dependency on ε.

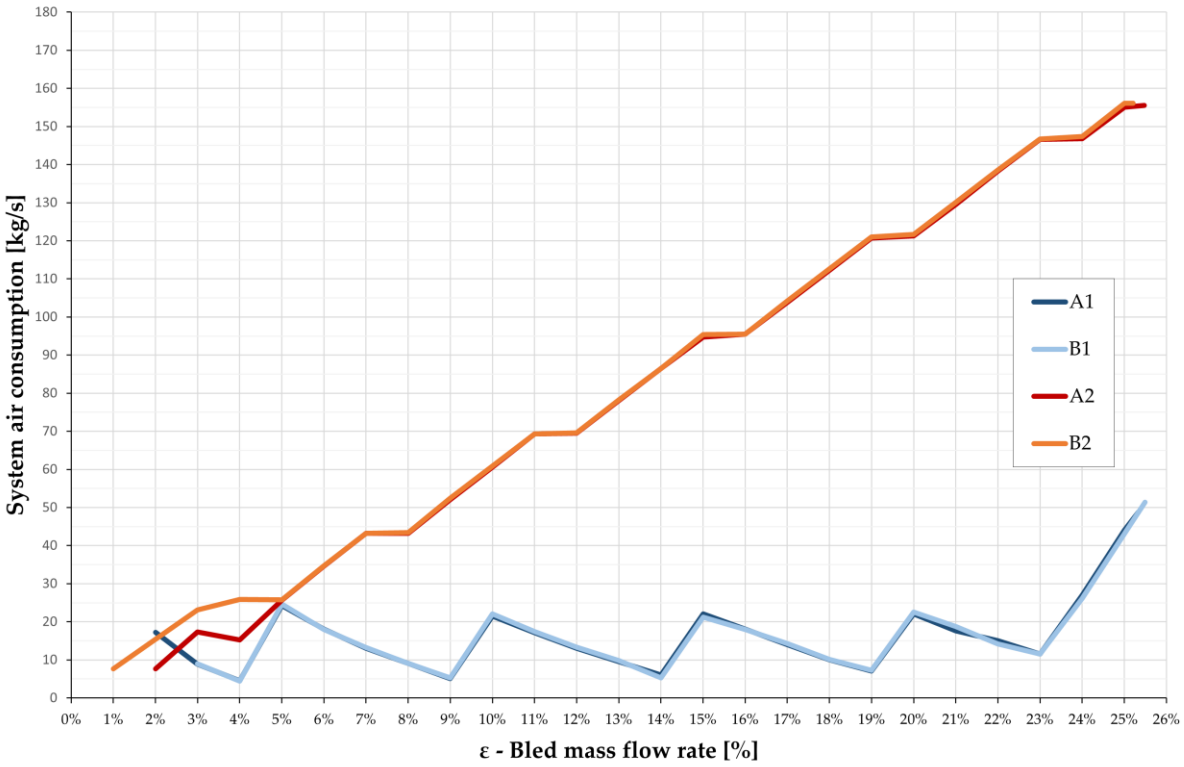

Figure 6.4 - System air consumption

If the endothermic operation (A2, B2) is considered, the result is that the electric power consumption related to the anode-side electric heater is much larger for these configurations with respect to the endothermic ones (A1, B1). Indeed, in configurations A2-B2, the stack outlet temperature is lower than the inlet and internal heat recovery does not suffice to bring inlet air to the stack inlet temperature, as already explained in chapter 4. This condition, combined to the larger air mass flow rates, explain the trends for the module anode-side electric heater power consumption in Figure 6.5.

The higher consumption for configuration B2 with respect to configuration A2 is related to the limitation in heat recovery in XH-PR-AN as the hot air stream must also perform water preheating in HX-PR-CA. Thus, a smaller heat recovery and a consequential increase in the power consumption of the electric heater.

As expected, the power consumption related to this component is null for exothermic configurations (A1, B1) as internal heat recovery at anode side is enough to bring the inlet air stream to design stack inlet temperature, resulting in a fairly regular trend over most of the operative range as for A2-B2.

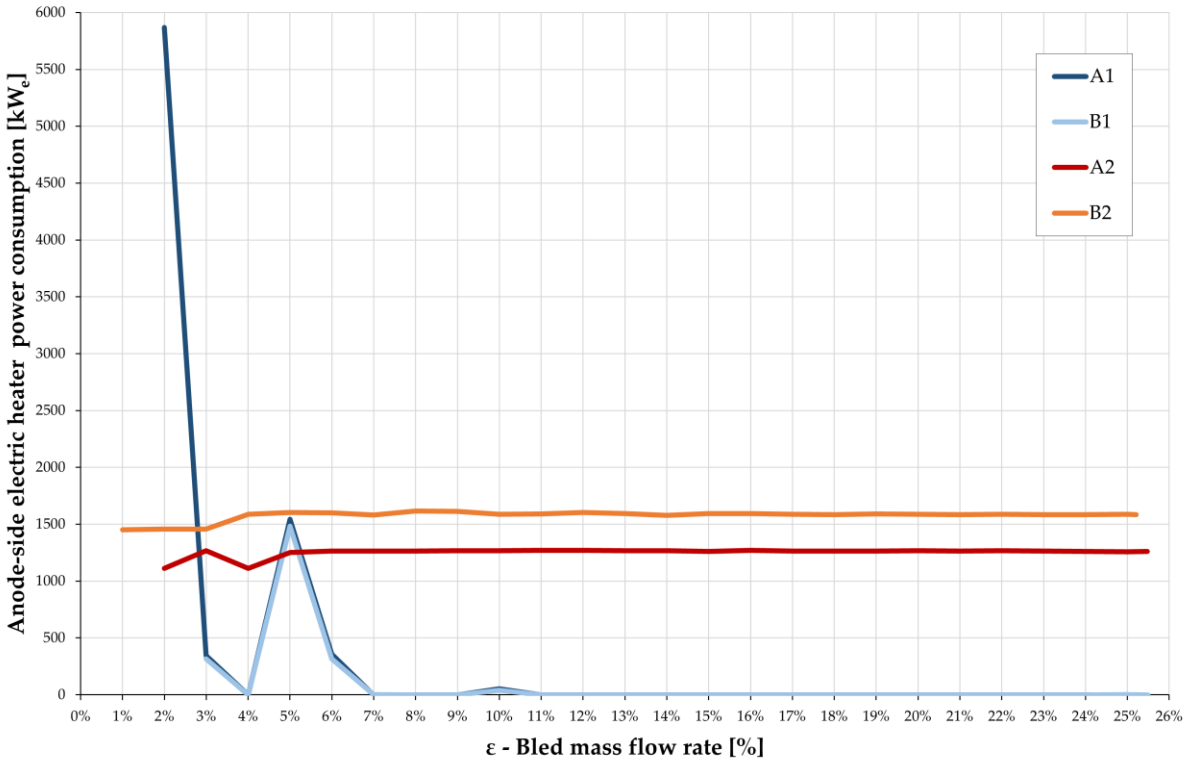

Figure 6.5 - Module anode-side electric heater power consumption

However, some fluctuations are visible in the region for low values of ε for all cases, especially for cases A1-B1. This phenomenon can be explained by looking at the trends for the cells' current density over the operational range in Figure 6.6 and the cells' operating voltage in Figure 6.3 and reminding what was previously explained on the voltage variations due to the slope of the polarization curves. The main reason for these fluctuations lies in the strategy used to determine the number of active modules, which are imposed to operate all at the same conditions. The constraints on current density, minimum flowing mass flow rates (A1, B1) and undesired condensation (A2) are easy to respect for large values of ε, as large quantities of inlet water are involved and the changes occurring when the number of active modules varies is dampened by their high number (minor changes in voltage and density for large ε).

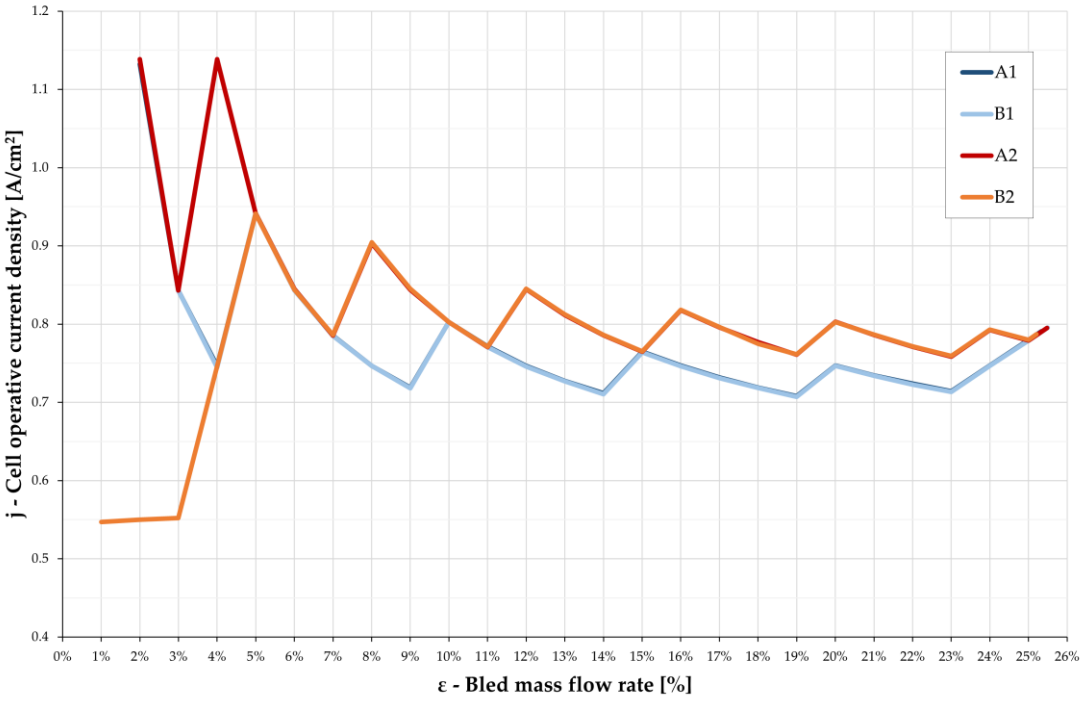

Figure 6.6 - Cells current density over the operative range

As ε reduces and the number of active modules becomes low, it may become necessary to break one constraint to keep one or more modules active.

Starting from configuration A2, two peaks are visible for current density (Figure 6.6) ε=2% and ε=4%, respectively. The reason it that operating with a higher number of modules to keep current density below the threshold value would have caused condensation of the hot stream to happen (section 5.2.3). As this effect is highly undesirable, it was decided to operate with a lower number of active modules, which caused current density to increase. As a 10% increase (j=1.1 A/cm²) was reputed acceptable, the working points was considered valid. This increase in j caused the voltage to move closer to the thermoneutral condition (Figure 6.3), resulting in reduction of stack electric efficiency (Figure 6.2), air consumption (Figure 6.4) and anode-side electric heater power consumption (Figure 6.5). As current density for ε=1% would have been too high, it was decided for an early shut off the hydrogen system.

Similar considerations can be made for configurations A1-B1. However, due to the inherent characteristics of the cell used in these configurations (higher slope of the polarization curve), variations in current density resulted in more significant variations of the other quantities with respect to A2.

What happened at ε=5% is that operation with a higher number of active modules would have caused current density to decrease, bringing the cells' voltage in proximity of the thermoneutral. This would have resulted in very small air mass flow rates at anode side, well below the 10% threshold. For this reason, it was decided to operate with a smaller number of active modules, so to increase current density and avoid the problem linked to air mass flow rate.

However, the small number of active modules caused a relatively large variation in current density, which resulted in an even larger increase in cells' voltage (Figure 6.3). This change brought the operating condition further from thermoneutral, causing a decrease in stack electric efficiency (Figure 6.2) and an increase in air consumption (Figure 6.4). This caused HX-PR-AN to become undersized, and internal heat recovery was no longer enough to bring inlet air to design stack inlet temperature, leading to a significant increase in the anode-side electric heater power consumption (Figure 6.5). Considerations for lower ε for configurations A1-B1 are the same as for configuration A2, and hence will not be repeated.

Since configuration B2 does not suffer from potential undesired streams condensation (section 5.2.4), regulation along the operational range is only dictated by the limit on current density, giving the chance to extend its actual operating range with respect to the other configurations.

6.3.2 Cathode-side electric heater power consumption

Moving to the power consumption related to the cathode-side electric heater (Figure 6.7), results are much easier to explain. First, power consumption of this component is lower than that of the anode-side electric heater (Figure 6.5), meaning that its impact on the overall module power consumption will be relatively lower.

The trend for all configurations on most of the operational range reflects what was already discussed when dealing with the system sizing in Chapter 4. Endothermic configurations (A2, B2) have a higher consumption with respect to the exothermic (A1, B1) due to the already-discussed impossibility for internal heat recovery to suffice for inlet streams heating up to inlet stack temperature. Moreover, consumption for A2 is higher than for B2 because of the outlet streams crossover which enhances internal heat recovery in HX-HT-CA for configuration B2, decreasing the need for external heat supply.

The same considerations apply to exothermic configurations (A1, B1). However, in this case, the overall consumption is lower (null for B1) due to the possibility of inlet streams to reach design stack temperature only by internal heat recovery.

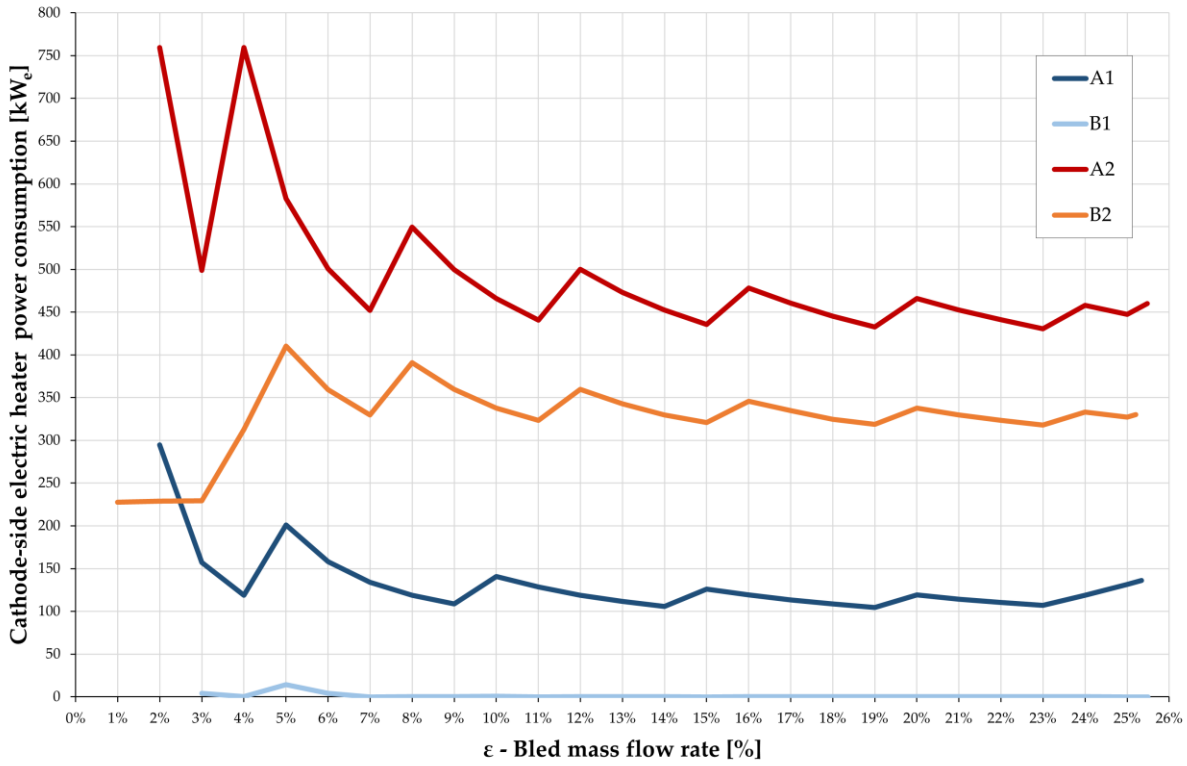

Figure 6.7 - Module cathode-side electric heater power consumption

Irregularities in the region for low ε can be explained similarly to how was done for the anode-side electric heater and are somewhat complementary. Due to the lower number of active modules adopted for operation of A2 at ε=4% and ε=2%, HX-HT-CA became undersized, leading to an increase in the electric heater power consumption. The same thing happened for A1 and B1 at ε=5%.

6.3.3 Module electric power consumption and efficiency

The module electric power consumption, shown in Figure 6.8 and accounts for the electric consumption from stacks, heater, and machines. What emerges is that the power consumption related to the electric heaters for configurations A2-B2 is enough to overturn the lower power consumption directly associated with the stacks and already discussed in section 6.2.

Exothermic configurations (A1, B1) benefit from lower module electric consumption despite a higher consumption from the stacks, as the power consumption liked to electric heaters is significantly lower.

The instabilities in the region for low values of ε are clearly addressable to the volatility and the huge variations in the electric heaters power consumption in the same region (Figure 6.5 and Figure 6.7)

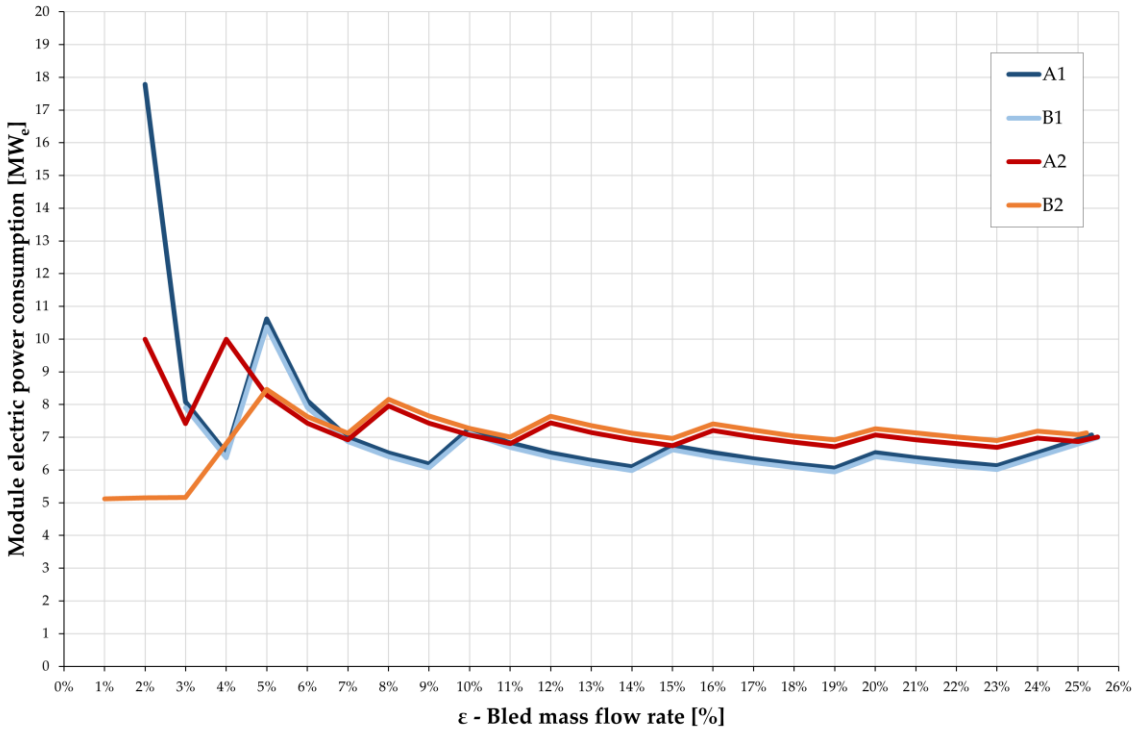

Figure 6.8 - Module electric power consumption

Since the hydrogen production remains the same for all the configurations (Figure 6.1), higher module electric power consumption implies a lower module electric efficiency and vice versa, as is shown in Figure 6.9.

Indeed, exothermic configurations (A1, B1) show better values for module electric efficiency over most of the operational range with respect to endothermic (A2, B2). The sawtooth-like profile of the trends for A1-B1 reflect the already-discussed larger variability of cell voltage and all the consequences it implies. Similarly, the regular trend for A2-B2 can be addressed to the narrower range for operative voltages (Figure 6.3).

Another difference with respect to the stack electric efficiency (Figure 6.2) is that the gap between the four configurations is significantly reduced, with values for all configurations spanning between 82% and 90% over most of the operative range.

The indentation in the trend for A1-B1 at ε=5% and the drop at ε=2% for B1 are explained by the relative peaks in the module electric power consumption caused by the adopted regulation strategy.

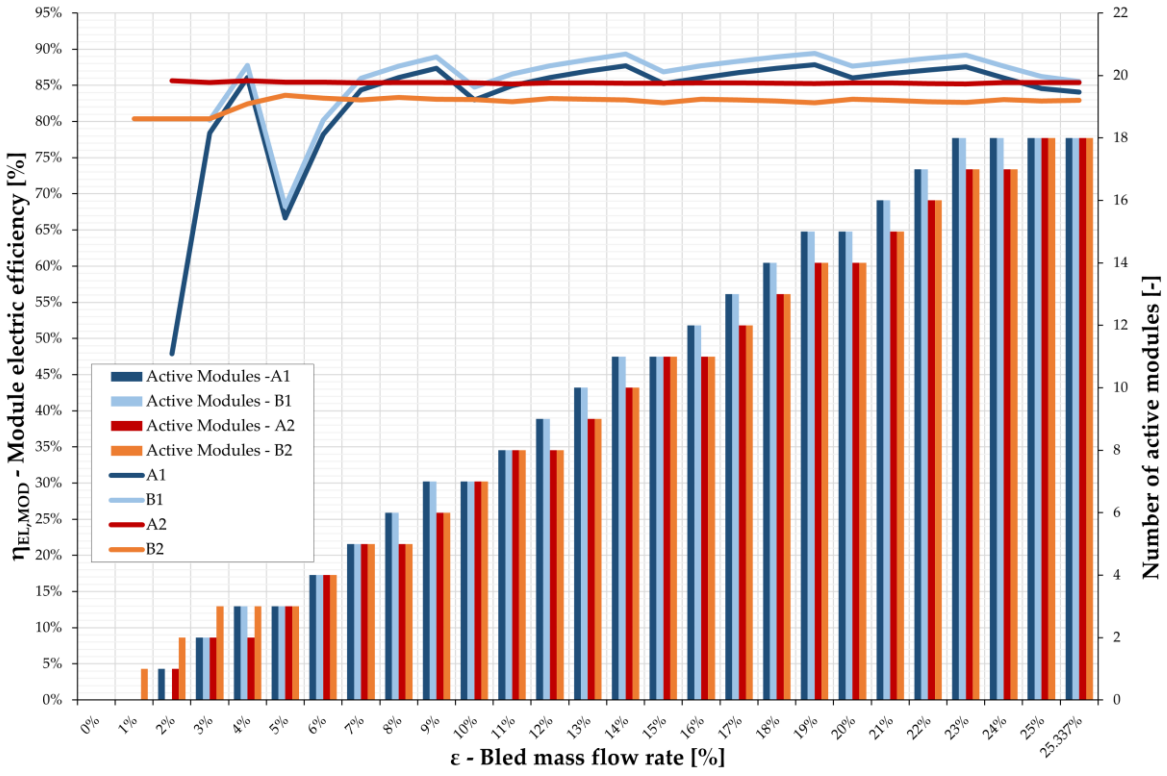

Figure 6.9 - Module electric efficiency over the operational range

6.4 Module first-law efficiency

The module first-law efficiency accounts for the net hydrogen production of a module and its total power consumption, as it is expressed in Equation (5.3). The total power consumption of the module is the sum of its electric power consumption and the thermal power entering the hydrogen system in HX-SPIL through the steam bled from the NPP. The solid lines in Figure 6.10 show the trends of the module first-law efficiency over the operational range for all the configurations (A1, B1, A2, B2).

It is immediately clear that the trends for module first-law efficiency strongly resemble those for module electric efficiency in Figure 6.9. The reason for this is that the amount of thermal power entering the hydrogen system is linearly dependent on ε, as the inlet and outlet conditions at the hot side of HX-SPIL are constant for any operative condition and thermal power only depends on the mass flow rate of steam bled from the NPP, as already explained in section 6.1. Obviously, including the thermal power in the calculation of the total power available to the hydrogen system

will cause the values for the modules first-law efficiency to be lower than their respective for electric efficiency.

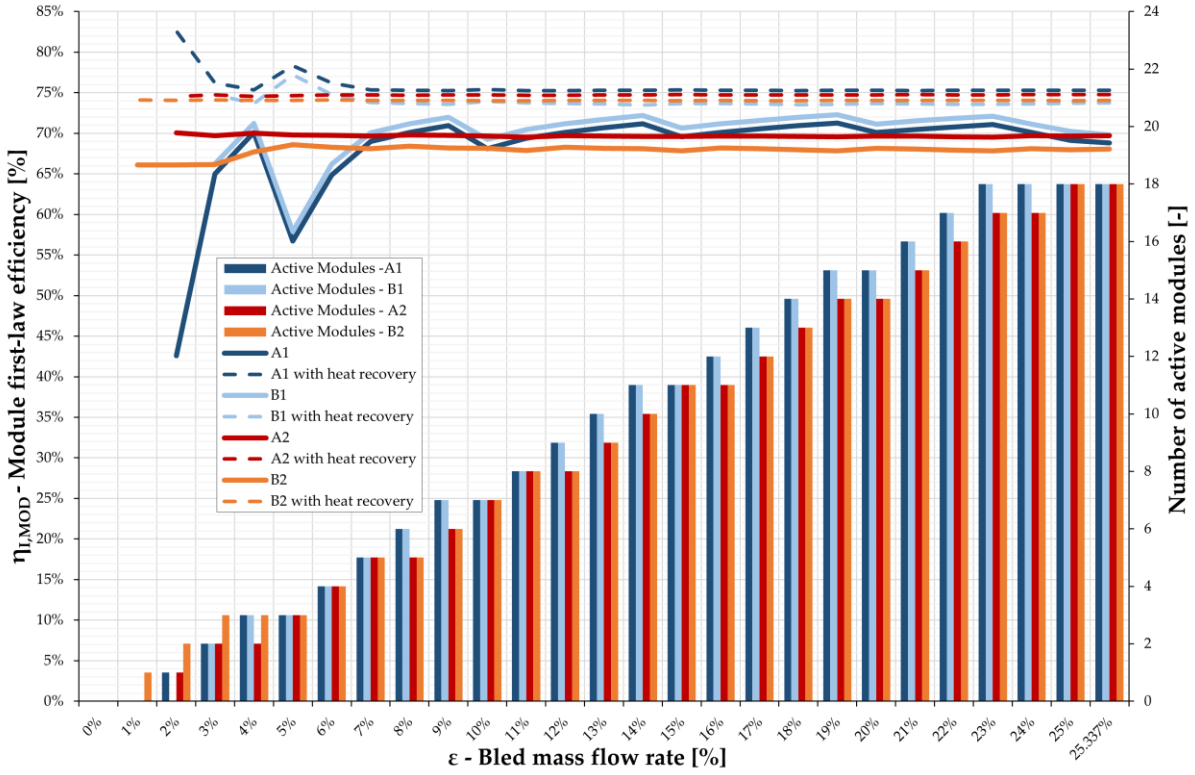

Figure 6.10 - Module first-law efficiency

For the sake of simplicity in the discussion, the trends for the module first-law efficiency with heat recovery have been included in the same figure (dashed lines). This efficiency accounts for the heat recovered from hot outlet streams as a useful product from the hydrogen system, as expressed by Equation (5.4). As explained, the heat recovered from the outlet streams could be used for low-pressure steam or sanitary hot water production. However, this is just a way not to waste heat that has been introduced into the hydrogen system but has not been used. So, theoretically talking, this quantity gives an idea of the thermal performances of the module.

The module first-law efficiency with heat recovery remains constant for most of the operative range for all the configurations, meaning that lower values of first-law efficiency correspond to higher quantities of recovered heat and vice versa. In the region for low values of ε, the trend for endothermic configurations (A2, B2) remains regular. For exothermic configurations (A1, B1) two peaks appear where the module first-law and electric efficiencies show the indentation and the plunge. This underlines once again that thermodynamic performances in that region are poor, with a significant quantity of heat introduced in the modules which is not converted

into hydrogen and hence available for recovery. More precisely, as air mass flow rate increases (Figure 6.4), HX-PR-AN becomes undersized and the hot outlet is a larger mass flow rate of air with a higher temperature (with respect to design), resulting in a larger heat rejection available for recovery.

As explained at the beginning of section 6.3, the absolute quantities of power and mass flow rates at system-level can be easily obtained by multiplying the values at module-level by the number of active modules in the considered operative point. This implies that relative quantities (efficiencies) at system-level have the exact same values of those at module-level, and the exact same considerations made at module-level apply. For this reason, no figure reporting the trend of the system first-law efficiency (Equation (5.5)) for the four configurations is provided, as it would perfectly match Figure 6.10.

6.5 Operating map of the integrated system

In this section, the results from the integration of the NPP and the hydrogen system will be shown, and an operating map of the integrated system will be provided for each of the four configurations. These maps allow to easily picture how the electric power available from the NPP is allocated over the whole operative range, highlighting the share delivered to the grid and how the electric power delivered to the hydrogen system is internally used.

Figure 6.11, Figure 6.12, Figure 6.13, and Figure 6.14 are the operating maps for configurations A1, B1, A2, and B2 , respectively. The green line at the bottom of every figure represents the hydrogen production, whose thermal power calculated on its LHV is reported in the figures so to be comparable with the other power values.

The sum of the areas is the total electric power available from the NPP. On the left-hand side of the figures is the condition at which no steam is bled towards the hydrogen system and the NPP power block operates at design conditions, meaning that all the electric power available is delivered to the grid (blue area). The right-hand side of the figures represents the design conditions for the respective hydrogen system configuration (no electric power delivered to the grid by the NPP). It is clear how the power delivered to the grid varies in almost the same way for all the configurations, only showing some appreciable variations between exothermic and endothermic configurations, coherently with the increase in module electric power consumption already discussed in section 6.3.

The area representing the electric power consumption from the stacks (in red) is thinner for endothermic configurations, reflecting lower values due to the better performances discussed in section 6.2. For exothermic configurations, the electric

consumption of the stacks represents almost the totality of the electric power consumption of the hydrogen system, as other quantities result virtually negligible (Figure 6.11 and Figure 6.12).

Cathode-side electric heaters power consumption is almost null for exothermic configurations, and is only barely visible for configuration A1, just above the red area in Figure 6.11. As already explained in section 6.3, cathode-side electric heater power consumption is higher for configuration A1 with respect to B1 due to the limitation in internal heat recovery caused by the hydrogen system layout. For endothermic configurations the green area becomes clearly visible as the electric heaters power consumption significantly increases (Figure 6.13 and Figure 6.14) and it results higher for configuration A2 for the same reason just explained above. Moving to the anode-side electric heaters power consumption, it results negligible for exothermic configurations, becoming relevant only in small ranges at low values of ε. These are the operating conditions described at the end of section 6.3, when HX-PR-CA (Figure 4.2) becomes undersized due to large inlet air mass flow rates (Figure 6.4) and anode-side electric heaters have to operate despite the endothermic conditions (Figure 6.5). For endothermic configurations, instead, the anode-side electric heaters power consumption is significantly larger, and the purple area is clearly visible. Coherently with Figure 6.5, the area is slightly thicker for configuration B2 (Figure 6.14) with respect to A2 (Figure 6.13).

It is evident that the power consumption from pumps and fans/compressors is practically negligible in the overall electric power consumption of the hydrogen system, as anticipated in section 6.3.

In the end, configuration A1 proves to offer better thermodynamic performances than endothermic configurations (A2, B2) with a lower system complexity with respect to configuration B1, resulting as the most promising among the four.

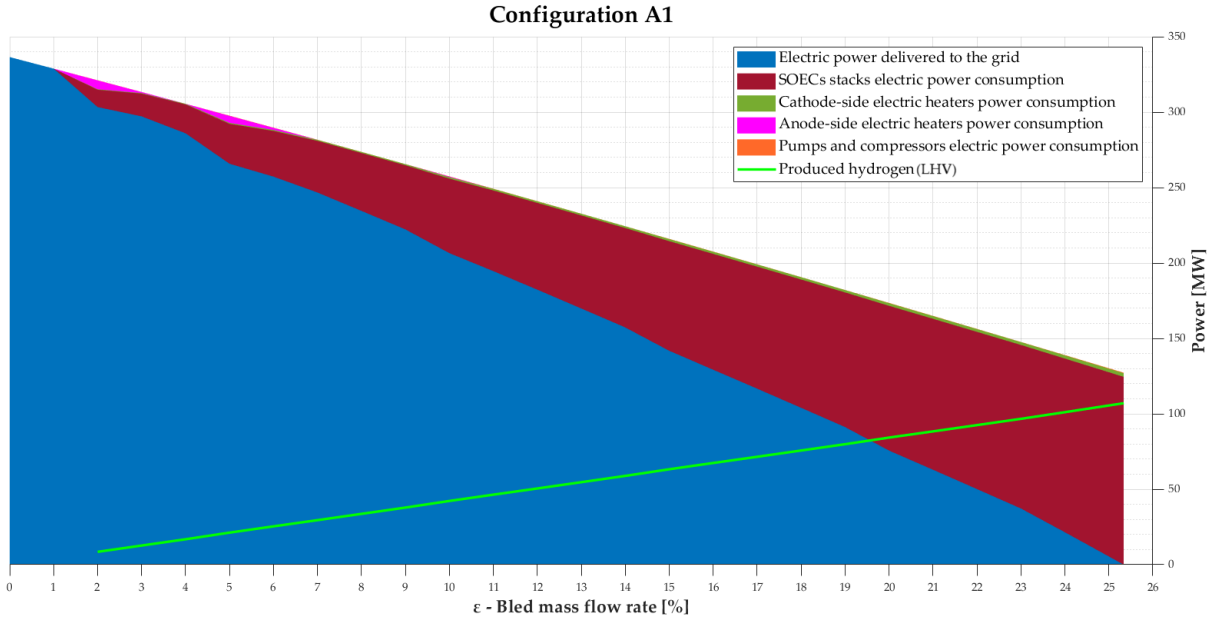

Figure 6.11 - Operating map for configuration A1

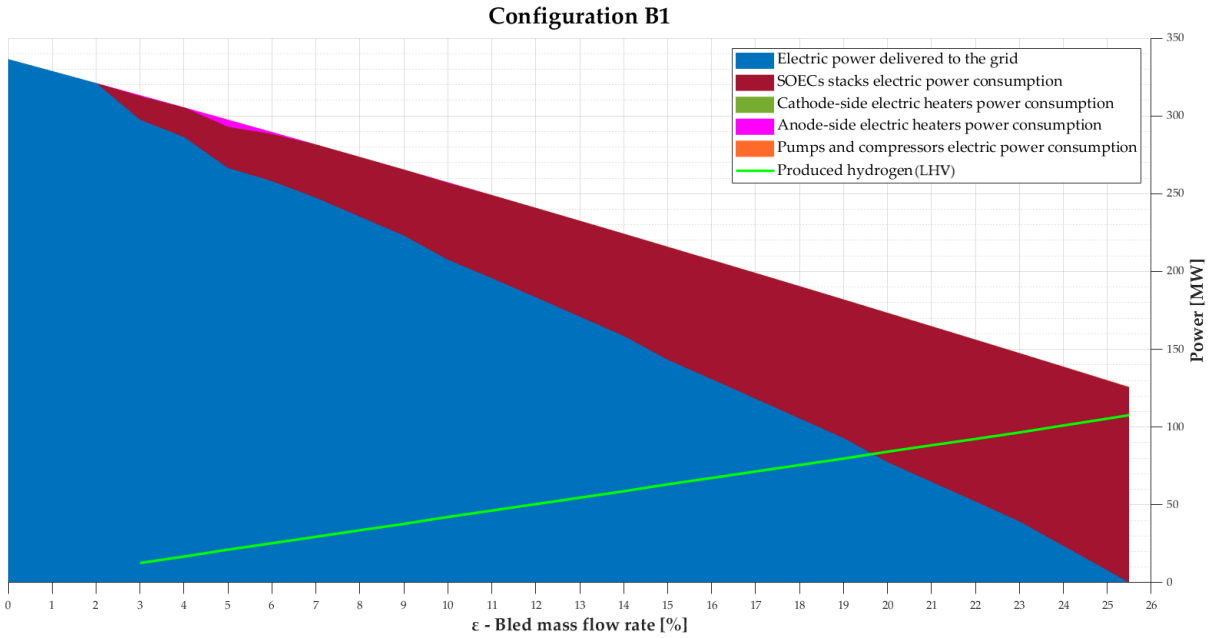

Figure 6.12 - Operating map for configuration B1

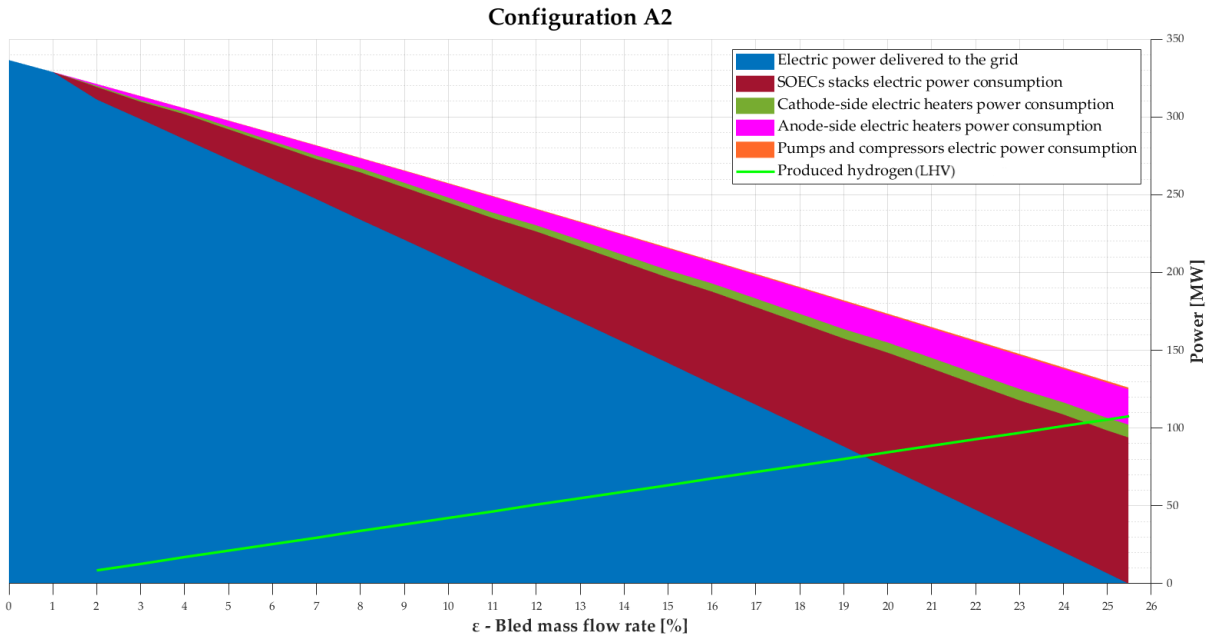

Figure 6.13 - Operating map for configuration A2

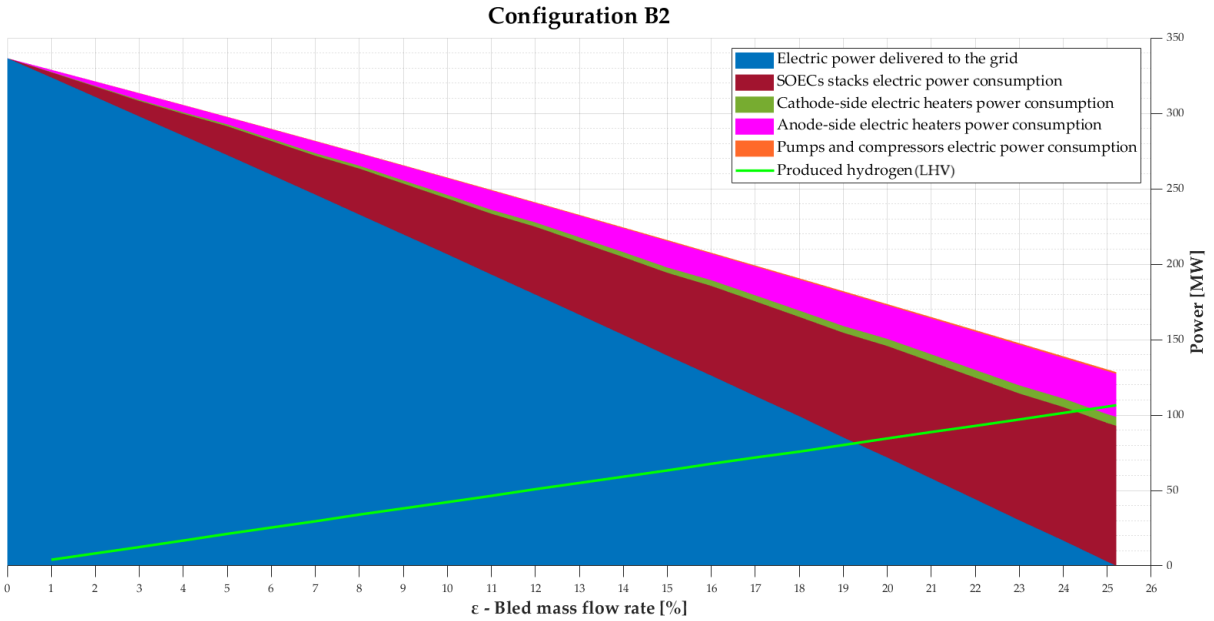

Figure 6.14 - Operating map for configuration B2

6.6 Energy balances of the integrated system

In this subsection, the Sankey diagrams relative to the integrated system will be introduced and discussed. These diagrams have been obtained considering the hot outlet of the condenser as the dead state for the NPP, meaning that thermal power can be extracted from the stream until its specific enthalpy is brought to the value in that point (point 1 in Figure 3.5).

Figure 6.15 shows the Sankey diagrams for the integrated system based on configuration A1 at ε=0%, that is when the NPP works at design conditions and the hydrogen system is off. Figure 6.16 is the Sankey diagram at ε=11%, an operating point at around half of the hydrogen system operating range. Lastly, Figure 6.17 is the Sankey diagram for the integrated system at ε=25.34%, that is when A1 work at design condition and no electric power is delivered to the grid from the NPP.

As expected, the quantity of electric power delivered to the grid decreases as ε moves from 0% to the design value for the hydrogen system. Coherently, larger quantities of thermal power are diverged towards the hydrogen system by means of the steam bleeding, causing the hydrogen production to increase accordingly.

However, it is evident that only a small share of thermal power from the bled steam is used by the hydrogen system, while the largest share is sent to the heat recovery section. This is because the hydrogen system water evaporation in HX-SPIL only employs the thermal power from bled steam desuperheating due to the specifications imposed in the design phase to avoid double phase change in the heat exchanger (section 4.2.1). Since the working fluid is water steam, the largest share of heat can be recovered from the condensation of the stream, as it is made clear by the dark blue lines. Indeed, the quantity of thermal power sent to the heat recovery section is calculated as the heat recovered by bringing the bled stream from saturated vapor conditions (HX-SPIL hot outlet) to saturated liquid condition, hence achieving full condensation of the stream.

Using this convention for heat recovery, the thermal power used in HX-SPIL is around 10% of the total thermal power from the bled steam, around 80% is sent to the heat recovery section, and a last 10% is accounted as a heat rejection loss (subcooling from saturated liquid to the specific enthalpy at condenser hot outlet).

As the two intended outputs from the integrated system are electricity and hydrogen, further productions linked to the heat recovery process are to be intended merely as a way not to waste heat which is still useful for other applications. This means that increasing the share of thermal power used over the total bled is fundamental to increase the overall system efficiency and enhance hydrogen production.

One last aspect that emerges from the analysis of the Sankey diagrams is that the power consumption from the electric heater in the NPP power block (section 3.4) significantly reduces the electric power availability of the NPP when is operated in off-design conditions. The power consumption related to this element increases with ε as shown in Figure 3.3.

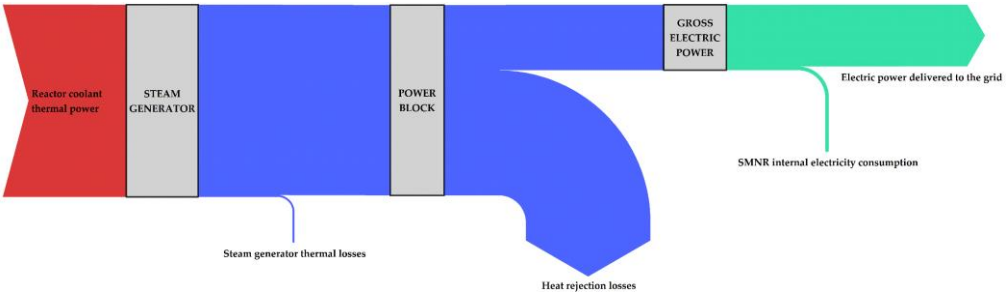

Figure 6.15 - Sankey diagram for the integrated system with configuration A1 at ε=0%

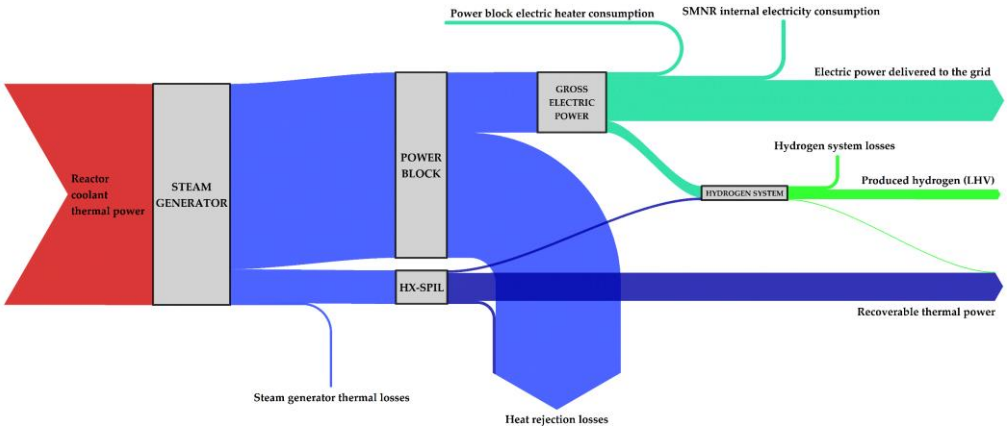

Figure 6.16 - Sankey diagram for the integrated system with configuration A1 at ε=11%

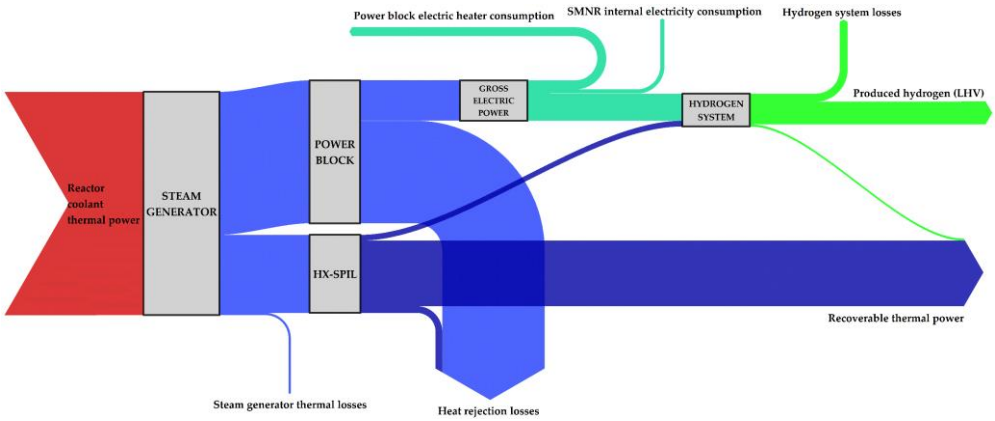

Figure 6.17 - Sankey diagram for the integrated system with configuration A1 at ε=25.34%

7. Conclusions

This works analysed the integration of a small modular reactor nuclear power plant with a hydrogen production unit based on solid oxide electrolysis. The IES was modelled and sized, and its steady-state operation was simulated over its whole operating range. Two separate models were implemented for the SMNR power block and for the SOE unit, using THERMOFLEX® and Aspen Plus®, respectively. The SMNR power block model allowed to obtain a curve that describes the electric power output as a function of the steam bled towards the SOE system while keeping the reactor and the main steam-generation heat exchanger at nominal conditions. The SOE system was sized so that, when operating at design conditions, no electric energy is delivered to the grid by the NPP. Six different configurations were proposed and assessed for the SOE system, with different anode-cathode cross flows and endo/exothermal stack conditions.

The modelled NPP power block has a net power output of 336.5 MW_e at nominal conditions and a first-law efficiency of 32.4%. Placing the steam bleeding upstream the high-pressure turbine, the off-design simulation of the power block showed that the NPP can provide electricity for values of bled steam mass flow rates up to 39.7% of the nominal quantity at the cold side of the steam generator. The availability of electric power in off-design operation is significantly reduced by the electric heater consumption, which absorbs 72 MWe at ε=39.7% (net zero electric power delivered to the grid) to guarantee unvaried inlet conditions to the steam generator.

The hydrogen system sizing provided the same number of modules for all the six proposed configurations, and a preliminary analysis allowed to eliminate the hydrogen system layout with the NPP-SOEC heat exchanger sized at system level due to its higher rigidity.

SOE operation is possible with either exothermic or endothermic stacks, with electric efficiencies around 90% and 120%, respectively, for the four configurations left. The values of first-law efficiencies are closer, with values around 67.5-70% for endothermic stacks and 70-72.5% for exothermic stacks. The maximum difference

between first-law efficiencies for the two cases is around 4.5 percentage points with the exothermic configurations featuring the highest values.

Off-design operation of the hydrogen system did not pose significant challenges for values of ε between 7% and design (around 25%). It became more complex for lower values of ε and required trade-offs due to the constraints imposed on the operating conditions (current density below 1 A/cm^2, minimum 10% of nominal mass flow rates flowing in each section and avoid condensation of hot streams during internal heat recovery). Configuration B2 showed the largest operational range, being able to operate down to ε=1%, while the other configurations required an early shut down at ε=2-3%. However, this region should be marginal for real-life operation. The first-law efficiency was almost constant on all the operative range for endothermic cases, while in endothermic cases it was strongly affected by the electric heaters power consumption for values of ε below 7%, with fluctuations in the order of 13-27 percentage points.

In the end, the configuration with exothermic stacks and without outlet streams crossovers (configuration A1) proved to offer better thermodynamic performances with a reduced layout complexity. The thermodynamic performances of the endothermic configurations (A2, B2) are strongly affected by the power consumption of the electric heaters, which are needed as the temperature of thermal power source (NPP) is less than half the nominal stack inlet temperature.

Looking at the critical aspects that emerged from the simulation process, the trends of the efficiencies in configuration A1 show appreciable variations within the operative range, especially in the region of low values of ε. This undesirable phenomenon strongly depends on the working conditions imposed to the active modules and their number. An asymmetric loading of the active modules would allow some of them to operate in more favourable conditions than with a balanced load distribution. This strategy could allow the average efficiencies to increase, smoothing the trend profile at the same time. Moreover, unbalanced active modules could possibly solve the instability issues at low values of ε, which are linked to the undersized heat exchangers and the consequential need for electric heaters on the inlet streams.

The decision to avoid a double phase change in the NPP-SOEC heat exchanger greatly increases the share of available thermal power from the bled steam downstream the component, as only 10% is used to perform water evaporation and 80% is sent to the heat recovery section. This factor strongly affects the overall IES performances. Part of this heat from could be recovered by using the NPP-SOEC heat exchanger hot outlet to perform the inlet water preheating. Separating the water preheating from the evaporation phase in two different heat exchangers would allow

to have only one phase change per heat exchanger. This could enable to overcome the technical difficulties and limitations in internal heat recovery for SOE steam superheating, removing the need of a cathode-side electric heater. However, the control logic for this kind of operation may be challenging in real-life operation.

The shift of the steam bleeding point from the NPP appears as an interesting factor to investigate. Indeed, the HPT works with a high-density fluid, meaning that it is particularly sensitive to the reduction of the steam mass flow rate. Moreover, the values of pressure and temperature at LPT inlet are still perfectly compatible for the integration of the SOE system, suggesting that the steam bleeding could be moved upstream the LPT. This would allow the HPT to work at nominal conditions, improving the thermodynamic performances. Different design features of the PB could also be investigated, in particular along the preheating line, in the attempt to reduce or eliminate the consumption of the electric heater.

A techno-economic analysis will be required to determine the most profitable size of the hydrogen plant (namely, the number of modules). Indeed, the proposed system was sized to have no electric power delivered to the grid at nominal conditions. An analysis of the typical load curve may suggest that such consistent power output reduction is rarely required and that a different sizing could contain costs and make the IES more profitable.

This work built a solid base for the analysis of this type of IES, comparing different system configurations and allowing to exclude those that do not provide advantages in terms of thermodynamic performances and complexity. The analysis of the energy balances allowed to pinpoint the critical aspects that need improvement to enhance the overall IES performances.

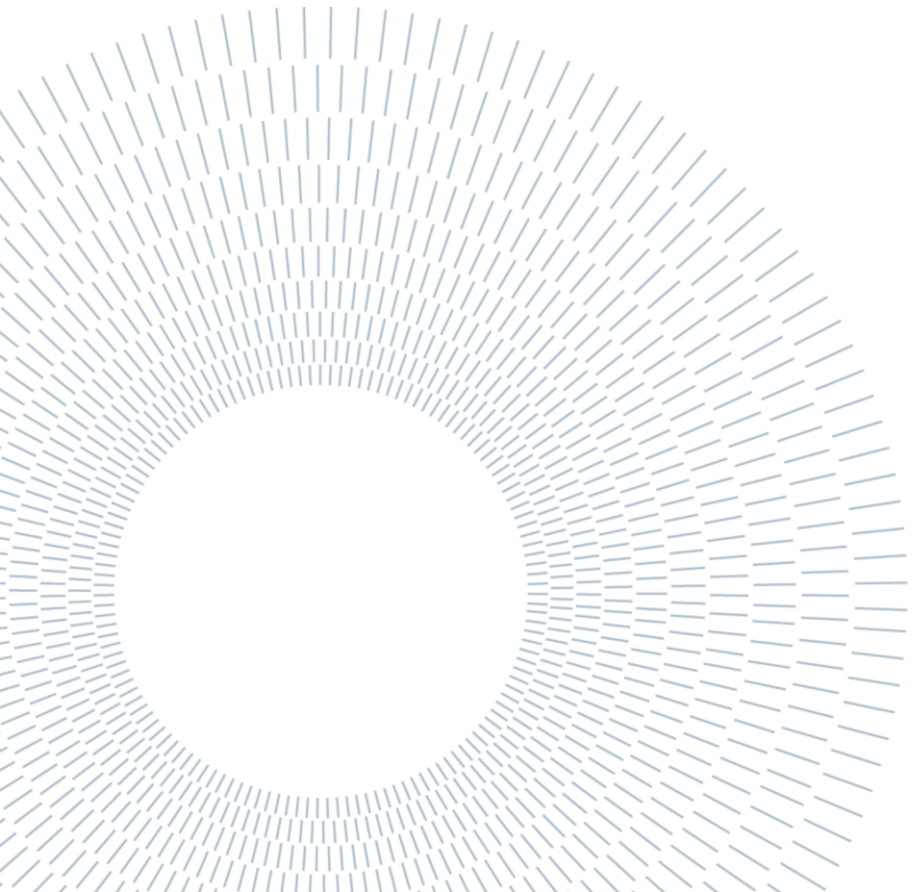

Bibliography

[1] United Nations (UN), "What Is Climate Change?" [Online]. Available: https://www.un.org/en/climatechange/what-is-climate-change

[2] National Aeronautics and Space Administration (NASA), "How Do We Know Climate Change Is Real?", [Online]. Available: https://climate.nasa.gov/evidence/

[3] National Aeronautics and Space Administration (NASA), "The Causes of Climate Change." [Online]. Available: https://climate.nasa.gov/causes/

[4] National Aeronautics and Space Administration (NASA), "The Effects of Climate Change." [Online]. Available: https://climate.nasa.gov/effects/

[5] M. M. Rahman, A. O. Oni, E. Gemechu, and A. Kumar, "Assessment of energy storage technologies: A review," *Energy Conversion and Management*, vol. 223. Elsevier Ltd, Nov. 01, 2020. doi: 10.1016/j.enconman.2020.113295.

[6] A. H. Azadnia, C. McDaid, A. M. Andwari, and S. E. Hosseini, "Green hydrogen supply chain risk analysis: A european hard-to-abate sectors perspective," *Renewable and Sustainable Energy Reviews*, vol. 182, Aug. 2023, doi: 10.1016/j.rser.2023.113371.

[7] International Energy Agency (IEA), "Understanding GEC Model Scenarios." [Online]. Available: https://www.iea.org/reports/global-energy-and-climate-model/understanding-gec-model-scenarios

[8] O. C. Anika, S. G. Nnabuife, A. Bello, E. R. Okoroafor, B. Kuang, and R. Villa, "Prospects of low and zero-carbon renewable fuels in 1.5-degree net zero emission actualisation by 2050: A critical review," *Carbon Capture Science and Technology*, vol. 5. Elsevier Ltd, Dec. 01, 2022. doi: 10.1016/j.ccst.2022.100072.

[9] A. Ajanovic, M. Sayer, and R. Haas, "The economics and the environmental benignity of different colours of hydrogen," *Int J Hydrogen Energy*, vol. 47, no. 57, pp. 24136–24154, Jul. 2022, doi: 10.1016/j.ijhydene.2022.02.094.

[10] Nuclear Energy Agency (NEA), "The Role of Nuclear Power in the Hydrogen Economy - Cost and Competitiveness," 2022.

[11] International Energy Agency (IEA), "Net Zero by 2050 - A Roadmap for the Global Energy Sector," 2021. [Online]. Available: www.iea.org/t&c/

[12] K. Guerra, P. Haro, R. E. Gutiérrez, and A. Gómez-Barea, "Facing the high share of variable renewable energy in the power system: Flexibility and stability requirements," *Appl Energy*, vol. 310, Mar. 2022, doi: 10.1016/j.apenergy.2022.118561.

[13] A. Biber, M. Tunçinan, C. Wieland, and H. Spliethoff, "Negative price spiral caused by renewables? Electricity price prediction on the German market for 2030," *Electricity Journal*, vol. 35, no. 8, Oct. 2022, doi: 10.1016/j.tej.2022.107188.

[14] M. D. Mathew, "Nuclear energy: A pathway towards mitigation of global warming," *Progress in Nuclear Energy*, vol. 143. Elsevier Ltd, Jan. 01, 2022. doi: 10.1016/j.pnucene.2021.104080.

[15] World Nuclear Association, "Plans For New Reactors Worldwide." [Online]. Available: https://world-nuclear.org/information-library/current-and-future-generation/plans-for-new-reactors-worldwide.aspx#:~:text=Today%20there%20are%20about%20440,are%20building%2C%20new%20power%20reactors.

[16] World Nuclear Association, "Nuclear Power Reactors." [Online]. Available: https://world-nuclear.org/information-library/nuclear-fuel-cycle/nuclear-power-reactors/nuclear-power-reactors.aspx

[17] M. Alwaeli and V. Mannheim, "Investigation into the Current State of Nuclear Energy and Nuclear Waste Management—A State-of-the-Art Review," *Energies (Basel)*, vol. 15, no. 12, Jun. 2022, doi: 10.3390/en15124275.

[18] B. Petrovic, M. Ricotti, S. Monti, N. Čavlina, and H. Ninokata, "Pioneering role of IRIS in the resurgence of small modular reactors," *Nucl Technol*, vol. 178, no. 2, pp. 126–152, 2012, doi: 10.13182/NT12-A13555.

[19] R. S. El-Emam and M. H. Subki, "Small modular reactors for nuclear-renewable synergies: Prospects and impediments," *Int J Energy Res*, vol. 45, no. 11, pp. 16995–17004, Sep. 2021, doi: 10.1002/er.6838.

[20] Edison Energia S.p.A., "Edison compie 140 anni e annuncia l'obiettivo di raddoppiare l'EBIDTA al 2030 accelerando le attività nella transizione energetica." [Online]. Available: https://www.edison.it/it/edison-compie-140-anni-e-annuncia-lobiettivo-di-raddoppiare-lebidta-al-2030-accelerando-le-attivita

[21] R. Rosner, S. Goldberg, and J. S. Hezir, "Small Modular Reactors-Key to Future Nuclear Power Generation in the U.S.," 2011.

[22] International Atomic Energy Agency (IAEA), "Advances in Small Modular Reactor Technology Developments - A Supplement to: IAEA Advanced Reactors Information System (ARIS)," 2022. [Online]. Available: http://aris.iaea.org

[23] International Atomic Energy Agency (IAEA), "Advances in Small Modular Reactor Technology Developments - A Supplement to: IAEA Advanced Reactors Information System (ARIS)," 2020. [Online]. Available: http://aris.iaea.org

[24] World Nuclear Association, "Small Nuclear Power Reactors." [Online]. Available: https://www.world-nuclear.org/information-library/nuclear-fuel-cycle/nuclear-power-reactors/small-nuclear-power-reactors.aspx

[25] S. Shiva Kumar and H. Lim, "An overview of water electrolysis technologies for green hydrogen production," *Energy Reports*, vol. 8. Elsevier Ltd, pp. 13793–13813, Nov. 01, 2022. doi: 10.1016/j.egyr.2022.10.127.

[26] S. Shiva Kumar and H. Lim, "An overview of water electrolysis technologies for green hydrogen production," *Energy Reports*, vol. 8. Elsevier Ltd, pp. 13793–13813, Nov. 01, 2022. doi: 10.1016/j.egyr.2022.10.127.

[27] J. Udagawa, P. Aguiar, and N. P. Brandon, "Hydrogen production through steam electrolysis: Model-based steady state performance of a cathode-supported intermediate temperature solid oxide electrolysis cell," *J Power Sources*, vol. 166, no. 1, pp. 127–136, Mar. 2007, doi: 10.1016/j.jpowsour.2006.12.081.

[28] T. Li *et al.*, "Robust Anode-Supported Cells with Fast Oxygen Release Channels for Efficient and Stable CO2 Electrolysis at Ultrahigh Current Densities," *Small*, vol. 17, no. 6, Feb. 2021, doi: 10.1002/smll.202007211.

[29] L. Barelli, G. Bidini, G. Cinti, and A. Ottaviano, "Study of SOFC-SOE transition on a RSOFC stack," *Int J Hydrogen Energy*, vol. 42, no. 41, pp. 26037–26047, Oct. 2017, doi: 10.1016/j.ijhydene.2017.08.159.

[30] N. Li *et al.*, "Reduced concentration polarization and enhanced steam throughput conversion with a solid oxide electrolysis cell supported on an electrode with optimized pore structure," *Int J Hydrogen Energy*, vol. 47, no. 51, pp. 21673–21680, Jun. 2022, doi: 10.1016/j.ijhydene.2022.05.013.

[31] B. Königshofer, M. Höber, G. Nusev, P. Boškoski, C. Hochenauer, and V. Subotić, "Accelerated degradation for solid oxide electrolysers: Analysis and prediction of performance for varying operating environments," *J Power Sources*, vol. 523, Mar. 2022, doi: 10.1016/j.jpowsour.2022.230982.

[32] M. Reytier *et al.*, "Stack performances in high temperature steam electrolysis and co-electrolysis," in *International Journal of Hydrogen Energy*, Elsevier Ltd, Sep. 2015, pp. 11370–11377. doi: 10.1016/j.ijhydene.2015.04.085.

[33] Y. Zhang, M. Han, and Z. Sun, "High performance and stability of nanocomposite oxygen electrode for solid oxide cells," *Int J Hydrogen Energy*, vol. 45, no. 8, pp. 5554–5564, Feb. 2020, doi: 10.1016/j.ijhydene.2019.05.027.

[34] M. Riedel, M. P. Heddrich, and K. A. Friedrich, "Analysis of pressurized operation of 10 layer solid oxide electrolysis stacks," *Int J Hydrogen Energy*, vol. 44, no. 10, pp. 4570–4581, Feb. 2019, doi: 10.1016/j.ijhydene.2018.12.168.

[35] T. Le Liu *et al.*, "Evaluation of polarization and hydrogen production efficiency of solid oxide electrolysis stack with La0.6Sr0.4Co0.2Fe0.8O3−δ-Ce0.9Gd0.1O1.95 oxygen electrode," *Int J Hydrogen Energy*, vol. 41, no. 36, pp. 15970–15978, Sep. 2016, doi: 10.1016/j.ijhydene.2016.04.243.

[36] Q. Li, Y. Zheng, W. Guan, L. Jin, C. Xu, and W. G. Wang, "Achieving high-efficiency hydrogen production using planar solid-oxide electrolysis stacks," *Int J Hydrogen Energy*, vol. 39, no. 21, pp. 10833–10842, Jul. 2014, doi: 10.1016/j.ijhydene.2014.05.070.

[37] E. Da Rosa Silva, G. Sassone, M. Prioux, M. Hubert, B. Morel, and J. Laurencin, "A multiscale model validated on local current measurements for understanding the solid oxide cells performances," *J Power Sources*, vol. 556, Feb. 2023, doi: 10.1016/j.jpowsour.2022.232499.

[38] F. Van Berkel, M. Shinde, M. Langerman, and C. Ferchaud, "Status of Solid Oxide Cell development at TNO," 2022.

[39] Hydrogen and Fuel Cell Technologies Office - U.S. Department of Energy, "High Temperature Electrolysis Manufacturing Workshop - Summary Report," 2022.

[40] T. Cui *et al.*, "Efficiency analysis and operating condition optimization of solid oxide electrolysis system coupled with different external heat sources," *Energy Convers Manag*, vol. 279, Mar. 2023, doi: 10.1016/j.enconman.2023.116727.

[41] J. M. Lee *et al.*, "Environ-economic analysis of high-temperature steam electrolysis for decentralized hydrogen production," *Energy Convers Manag*, vol. 266, Aug. 2022, doi: 10.1016/j.enconman.2022.115856.

[42] International Energy Agency (IEA), "Hydrogen Production and Infrastructure Projects Database." [Online]. Available: https://www.iea.org/data-and-statistics/data-product/hydrogen-production-and-infrastructure-projects-database#hydrogen-production-projects

[43] World Nuclear News (WNN), "OKG signs hydrogen supply contract." [Online]. Available: https://www.world-nuclear-news.org/Articles/OKG-signs-hydrogen-supply-contract

[44] The Barents Observer, "Kola NPP builds test facility for hydrogen." [Online]. Available: https://thebarentsobserver.com/en/industry-and-energy/2021/07/kola-npp-builds-test-facility-hydrogen

[45] TASS, "Kola NPP produces hydrogen in cutting-edge process — Rosatom." [Online]. Available: https://tass.com/economy/1556129

[46] Constellation Energy, "Constellation Starts Production at Nation's First One Megawatt Demonstration Scale Nuclear-Powered Clean Hydrogen Facility ." [Online]. Available: https://www.constellationenergy.com/newsroom/2023/Constellation-Starts-Production-at-Nations-First-One-Megawatt-Demonstration-Scale-Nuclear-Powered-Clean-Hydrogen-Facility.html

[47] Salzgitter AG, "Project 'GrInHy2.0.'" [Online]. Available: https://salcos.salzgitter-ag.com/en/grinhy-20.html

[48] Reflex, "Reversible solid oxide Electrolyzer and Fuel cell for optimized Local Energy mix." [Online]. Available: https://www.reflex-energy.eu/

[49] Offshore Energy, "MultiPLHY project: Sunfire installs world's largest SOEC electrolyser." [Online]. Available: https://www.offshore-energy.biz/multiplhy-project-sunfire-installs-worlds-largest-soec-electrolyser/

[50] Hydrogen Partnership Austria, "Elektrolyseure in Betrieb - HotFlex." [Online]. Available: https://www.hypa.at/#heading-3774-132

[51] FuelCell Energy, "Solid Oxide Electrolysis System Demonstration - 2023 Annual Merit Review and Peer Evaluation Meeting," Jun. 2023. [Online]. Available: https://www.hydrogen.energy.gov/docs/hydrogenprogramlibraries/pdfs/review23/ta039_ghezel-ayagh_2023_o-pdf.pdf

[52] Bloom Energy, "Xcel Energy and Bloom Energy to Produce Zero-Carbon Hydrogen at Nuclear Facility." [Online]. Available: https://www.bloomenergy.com/news/xcel-energy-and-bloom-energy-to-produce-zero-carbon-hydrogen-at-nuclear-facility/

[53] N. Chalkiadakis, E. Stamatakis, M. Varvayanni, A. Stubos, G. Tzamalis, and T. Tsoutsos, "A New Path towards Sustainable Energy Transition: Techno-Economic Feasibility of a Complete Hybrid Small Modular Reactor/Hydrogen

(SMR/H2) Energy System," *Energies (Basel)*, vol. 16, no. 17, Sep. 2023, doi: 10.3390/en16176257.

[54] A. Ho, K. Mohammadi, M. Memmott, J. Hedengren, and K. M. Powell, "Dynamic simulation of a novel nuclear hybrid energy system with large-scale hydrogen storage in an underground salt cavern," *Int J Hydrogen Energy*, vol. 46, no. 61, pp. 31143–31157, Sep. 2021, doi: 10.1016/j.ijhydene.2021.07.027.

[55] J. S. Kim, R. D. Boardman, and S. M. Bragg-Sitton, "Dynamic performance analysis of a high-temperature steam electrolysis plant integrated within nuclear-renewable hybrid energy systems," *Appl Energy*, vol. 228, pp. 2090–2110, Oct. 2018, doi: 10.1016/j.apenergy.2018.07.060.

[56] S. Pandey *et al.*, "Modeling of Solid Oxide -Electrolyzer and -Fuel Cell for Nuclear-Renewable Integrated Energy Systems," in *IEEE Power and Energy Society General Meeting*, IEEE Computer Society, 2023. doi: 10.1109/PESGM52003.2023.10253272.

[57] J. M. Lee *et al.*, "Environ-economic analysis of high-temperature steam electrolysis for decentralized hydrogen production," *Energy Convers Manag*, vol. 266, Aug. 2022, doi: 10.1016/j.enconman.2022.115856.

[58] "Thermoflow website." Accessed: Sep. 12, 2023. [Online]. Available: https://www.thermoflow.com/products_generalpurpose.html#

[59] M. D. Carelli, B. Petrović, N. Čavlina, and D. Grgić, "IRIS (International Reactor Innovative and Secure)-Design Overview and Deployment Prospects," Bled, Slovenia, Sep. 2005.

[60] M. Williamson and L. Townsend, "Sizes of Secondary Plant Components for Modularized IRIS Balance of Plant Design," 2003.

[61] S. R. Greene, G. F. Flanagan, and A. P. Borole, "Integration of Biorefineries and Nuclear Cogeneration Power Plants - A Preliminary Analysis," Oak Ridge (TN), USA, Mar. 2009. [Online]. Available: http://www.osti.gov/contact.html

[62] "Aspen Plus." [Online]. Available: https://www.aspentech.com/en/products/engineering/aspen-plus

[63] S. Marco, "Assessment of SOEC integration with a nuclear power plant to increase electric flexibility," Master's Theis, Politecnico di Milano, 2022.

[64] F. Berkel, C. J. Ferchaud, O. Partenie, M. Linders, and Y. van Delft, "Solid Oxide Cell Technology Development at TNO," *ECS Meeting Abstracts*, vol. MA2021-03, no. 1, pp. 227–227, Jul. 2021, doi: 10.1149/MA2021-031227mtgabs.

[65] J. Sanz-Bermejo, J. Muñoz-Antón, J. Gonzalez-Aguilar, and M. Romero, "Part load operation of a solid oxide electrolysis system for integration with renewable energy sources," *Int J Hydrogen Energy*, vol. 40, no. 26, pp. 8291–8303, Jul. 2015, doi: 10.1016/j.ijhydene.2015.04.059.

[66] M. A. Boda, S. S. Deshetti, and M. A. Gavade, "Design and Development of Parallel-Counter Flow Heat Exchanger," 2017. [Online]. Available: www.ijirae.com

[67] W. Roetzel and B. Spang, "Typical Values of Overall Heat Transfer Coefficinets," in *VDI Heat Atlas*, 2010.

[68] A. C. Dimian and C. S. Bildea, "Appendix B," in *Chemical Process Deisgn - Computer-Aided Case Studies*, 2008.

[69] "The Engineering ToolBox - Heat Exchangers - Overall Heat Transfer Coefficients." Accessed: Nov. 07, 2023. [Online]. Available: https://www.engineeringtoolbox.com/heat-transfer-coefficients-exchangers-d_450.html

[70] J. Cao *et al.*, "A Novel Solid Oxide Electrolysis Cell with Micro-/Nano Channel Anode for Electrolysis at Ultra-High Current Density over 5 A cm−2," *Adv Energy Mater*, vol. 12, no. 28, Jul. 2022, doi: 10.1002/aenm.202200899.

List of Figures

List of Tables

List of Symbols

Variable	Description	SI unit
A	Heat transfer area	m^2
a	Stoichiometric coefficient	-
ASR	Area-specific resistance	Ω·cm2
C_P	Specific heat	J/kg °C
ΔG	Gibbs' free energy	J
ΔT_{lm}	Logarithmic mean temperature difference	°C
ε	Share of bled steam mass flow rate	-
η	Efficiency	-
E_{CELL}	Cell potential	V
j	Current density	A/cm^2
$LCOH$	Levelized cost of hydrogen	$\$/kg_{(H2)}$
$LCOHD$	Levelized cost of hydrogen and delivery	$\$/kg_{(H2)}$
m	Mass flow rate	kg/s

n	Number of moles	mol
OCV	Open circuit voltage	V
p	Pressure	bar
Q	Thermal power	W
Q_R	Reaction quotient	-
Q_{loss}	Polarization heat flux	W/m^2
Q_{react}	Reaction heat flux	W/m^2
S	Cell active area	cm^2
T	Temperature	°C
U	Overall heat transfer coefficient	W/m^2 °C
UF	Utilization factor	$mol_{(H2)}/mol_{(H2O)}$
V	Voltage	V
W	Power	W

Acknowledgements

Ringrazio sentitamente il Prof. Colbertaldo e l'Ing. Ficili per il loro sostegno e la loro disponibilità, che mi hanno aiutato nel compiere quest'ultimo passo della mia carriera universitaria.

Un ringraziamento speciale va alla mia famiglia. In particolar modo, ringrazio i miei genitori e mio fratello Giulio, che non hanno mai mancato di farmi sentire tutto il loro supporto, la loro fiducia ed il loro affetto in questi anni.

Altrettanto sentitamente ringrazio Anna, che è stata al mio fianco sin dal primo momento di questo percorso, dimostrandosi un enorme sostegno e che mi ha sempre incoraggiato con le sue parole ed il suo amore.

Ci tengo a ringraziare anche tutti i miei amici: quelli di una vita e quelli che lo sono diventati nell'affrontare questo viaggio. A voi il mio ringraziamento per aver saputo rendere più semplice la strada, regalandomi affetto e spensieratezza con il tempo trascorso insieme.